



Norwegian University of  
Science and Technology

# Experimental Evaluation of Broadband Wave Propagation in Plates

**Andreas Sørbrøden Talberg**

Master of Science in Physics and Mathematics

Submission date: June 2016

Supervisor: Jon Andreas Støvneng, IFY

Co-supervisor: Tonni F. Johansen, SINTEF

Norwegian University of Science and Technology  
Department of Physics



# Preface

This Master's thesis is the result of 20 weeks work, which was conducted during the spring semester of 2016. The thesis has been written for the Department of Physics at the Norwegian University of Science and Technology (NTNU) in cooperation with SINTEF, and finalizes my study in Physics and Mathematics - Applied Physics. In addition to working on this thesis I have participated at the Scandinavian Symposium on Physical Acoustics (SSPA) as well as submitted a paper for the conference proceedings during the semester.

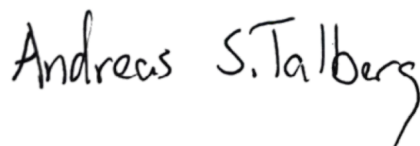
## Acknowledgments

I will like to start by thanking my supervisor at SINTEF, Tonni Franke Johansen, for great guidance and help with my thesis, in the preparations for my talk at the SSPA, and when submitting the paper for the conference proceedings.

I will also like to show my gratitude to SINTEF Petroleum Research, Statoil and NTNU for lending me the equipment used in the experimental work. A thanks is also given to the people at SINTEF Formation Physics for helping me with my experimental setup, where especially Hans Lund has given me great help in the customization of the setup.

At last I would like to thank my fellow M.Sc. candidates at Applied Physics - NTNU for good discussions and help throughout the semester.

Trondheim, June 21, 2016

A handwritten signature in black ink that reads "Andreas S. Talberg". The signature is written in a cursive style with a long, sweeping tail on the letter 'g'.

Andreas Sørbrøden Talberg



# Abstract

As the number of aging oil field in the North Sea is increasing, the number of plug and abandonment (P&A) jobs which has to be conducted on the wells going out of production, e.g. to prevent hydrocarbons from leaking out of the reservoirs, are increasing with it. In the planning of a P&A job, the bonding and hydraulic isolation properties of the sealing material in a cased well must be logged. In this thesis some of the ultrasonic evaluation tools currently used to ensure that a well cementing job has been properly executed will be presented together with two of the widely used techniques in ultrasonic logging, in particular the pulse-echo technique and the pitch-catch technique. Even though the ultrasonic pitch-catch technique is widely used in well logging and is commercially available, little research has been done on the use of this technique in an environment with multiple casings.

A finite-element simulation model were constructed for a double-casing environment, and a set of ultrasonic measurements were performed to give an experimental verification to the simulation model. The simulations were conducted using COMSOL Multiphysics and the ultrasonic experiments in this thesis were conducted on the Statoil-funded Behind Casing Logging Set-Up (BeCaLoS) developed by SINTEF Petroleum Research, designed to replicate the steel casing setup in an oil well.

It was found from the simulations that a train of leaky Lamb wave packets is excited on both casings in the double-casing environment. Through the ultrasonic experiments the excitation of the Lamb wave packet trains on the plate was experimentally verified. Three sets of pitch-catch measurements were conducted by moving the receiver in a grid parallel to the plate to measure the Lamb wave spreading in the plate, each with a different setup for the lower plate. The tilting of the lower plate in the experimental setup, replicating the situation of casing eccentricity, could be detected through these sets of pitch-catch measurements.



# Sammendrag

Antall eldre oljefelt i Nordsjøen øker, og med det øker behovet for plugging av brønner som nærmer seg enden på sin produktive levetid. Plugging av brønnene blir gjennomført blandt annet for å sikre at hydrokarboner ikke lekker fra reservoarene med olje eller gass til omgivelsene. Når man skal planlegge pluggingen av en brønn med et rør plassert i brønnen, er det viktig å ha god data om bindingen og den hydrauliske isolasjonsevnen til materialet plassert utenfor røret. I denne avhandlingen vil noen akkustiske verktøy brukt til å kontrollere at en sementerings jobb i en oljebrønn har blitt utført korrekt bli presentert, sammen med to metoder disse verktøyene bruker, nemlig puls-ekko metoden og "pitch-catch" metoden. Selvom verktøy som bruker "pitch-catch" metoden er kommersielt tilgjengelig, har det blitt gjort lite forskning på bruk av denne metoden til sementevaluering i en brønn med flere rør utenpå hverandre.

En simulerings modell for et scenario med to rør plassert utenfor hverandre ble laget ved bruk av et endelig element metode program, og for å gi en eksperimentell verifikasjon til den simulerte modellen ble tre sett med eksperimentelle målinger gjennomført. COMSOL Multiphysics ble brukt til å gjennomføre simuleringene, mens målingene ble gjennomført på den Statoil-finansierte "Behind Casing Logging Set-Up" (BeCaLoS) utviklet av SINTEF Petroleum for å etterligne forholdene i en oljebrønn.

Fra simuleringene ble det observert at et tog med Lamb bølgepakker ble eksitert i stålplatene, noe som også ble eksperimentelt verifisert. Tre sett med "pitch-catch"-målinger ble gjennomført ved å plassere mottakeren i et rutenett av målepunkter for å observere Lamb bølge-spredningen i platen for de ulike oppsettene. Monteringen av den nederste platen med en vinkel i forhold til den øvre platen i det eksperimentelle oppsettet, gjort for å replikere to rør som er usentrerte i forhold til hverandre, kunne også bli observert via disse "pitch-catch"-målingene.





# Table of Contents

Preface . . . . .	i
Abstract . . . . .	iii
Sammendrag . . . . .	v
List of Tables . . . . .	ix
List of Figures . . . . .	xiii
Abbreviations . . . . .	xv
<b>1 Introduction</b>	<b>1</b>
<b>2 Well Cementing and Cement Evaluation</b>	<b>3</b>
2.1 Purpose of well cementing . . . . .	3
2.2 Challenges . . . . .	5
<b>3 Ultrasonic Logging</b>	<b>7</b>
3.1 History . . . . .	7
3.2 The pulse-echo method . . . . .	9
3.3 The pitch-catch method . . . . .	12
3.3.1 The Lamb wave . . . . .	12
3.3.2 The pitch-catch technique . . . . .	17
3.3.3 The leaky Lamb wave . . . . .	18
<b>4 Ultrasonic Lab Experiment</b>	<b>21</b>
4.1 Experimental setup . . . . .	22
4.1.1 The Behind Casing Logging Set-Up . . . . .	22
4.1.2 Transducer and hydrophone holder array . . . . .	23

4.2	Experimental equipment . . . . .	24
4.3	Execution . . . . .	26
4.3.1	Configuration of the setup . . . . .	26
4.3.2	Broadband wave propagation in steel plates . . . . .	27
4.4	Simulation setup . . . . .	27
<b>5</b>	<b>Results</b>	<b>31</b>
5.1	Configuration of the setup . . . . .	31
	Broadband wave propagation in steel plates . . . . .	31
5.2	Experimental results . . . . .	32
5.2.1	Second plate: 3 mm thick . . . . .	32
5.2.2	Second plate: 4 mm thick . . . . .	39
5.2.3	Second plate: 3 mm thick - tilted . . . . .	45
5.3	COMSOL simulations . . . . .	52
5.3.1	Second plate: 3 mm thick - Flat aperture function . . . . .	52
5.3.2	Second plate: 3 mm thick - Sine aperture function . . . . .	53
5.3.3	Second plate: 4 mm thick - Sine aperture function . . . . .	57
<b>6</b>	<b>Discussion</b>	<b>61</b>
<b>7</b>	<b>Conclusions and Future Work</b>	<b>65</b>
	<b>Bibliography</b>	<b>67</b>
<b>A</b>	<b>Tables</b>	<b>71</b>
<b>B</b>	<b>SSPA 2016 Article</b>	<b>73</b>

# List of Tables

A.1	The configuration of the experimental setup with a 3 mm thick plate mounted inside the BeCaLoS. . . . .	71
A.2	The configuration of the experimental setup with a 4 mm thick plate mounted inside the BeCaLoS. . . . .	72
A.3	The configuration of the experimental setup with a 3 mm thick plate mounted with a tilt inside the BeCaLoS. . . . .	72



# List of Figures

2.1	The casing strings . . . . .	4
2.2	Cement slurry displacement problems . . . . .	5
3.1	Ultrasonic Tools developed by Schlumberger . . . . .	8
3.2	The Pulse-Echo Technique . . . . .	11
3.3	A sketch of the free plate in which the Lamb waves propagate . . . . .	12
3.4	The particle displacement in the symmetrical and anti-symmetrical Lamb wave modes . . . . .	15
3.5	Lamb Wave Dispersion Curves . . . . .	16
3.6	The Pitch-Catch Principle . . . . .	17
3.7	Schematic of multiple leaky Lamb wave packets on two plates . . . . .	20
4.1	The BeCaLoS - Photo . . . . .	21
4.2	BeCaLoS sketch - air in annulus . . . . .	22
4.3	BeCaLoS sketch - two plates - water in annulus . . . . .	23
4.4	The transducer/hydrophone holder array . . . . .	24
4.5	Photo of the oscilloscope and the pulser/receiver . . . . .	25
4.6	Photo of the transducer and hydrophone . . . . .	25
4.7	Sketch of the water-propagating waves . . . . .	26
4.8	COMSOL Simulation Setup . . . . .	28
5.1	Abs. value of the detected pulse - Logarithmic - 3 mm plate . . . . .	33
5.2	Waterfall plot of the detected pulses - Normalized - 3 mm plate . . . . .	34

5.3	Maximum amplitude of the wave packets as function of $x$ -position - Logarithmic - 3 mm plate . . . . .	34
5.4	Amplitude of 1st wave packet - Logarithmic - 3 mm plate . . . . .	36
5.5	Beam profile of 1st wave packet - Logarithmic - 3 mm plate . . . . .	36
5.6	Amplitude of 2nd wave packet - Logarithmic - 3 mm plate . . . . .	37
5.7	Beam profile of 2nd wave packet - Logarithmic - 3 mm plate . . . . .	37
5.8	Amplitude of 3rd wave packet - Logarithmic - 3 mm plate . . . . .	38
5.9	Beam profile of 3rd wave packet - Logarithmic - 3 mm plate . . . . .	38
5.10	Abs. value of the detected pulse - Logarithmic - 4 mm plate . . . . .	40
5.11	Waterfall plot of the detected pulses - Normalized - 4 mm plate . . . . .	40
5.12	Maximum amplitude of the wave packets as function of $x$ -position - Logarithmic - 4 mm plate . . . . .	41
5.13	Amplitude of 1st wave packet - Logarithmic - 4 mm plate . . . . .	43
5.14	Beam profile of 1st wave packet - Logarithmic - 4 mm plate . . . . .	43
5.15	Amplitude of 2nd wave packet - Logarithmic - 4 mm plate . . . . .	44
5.16	Beam profile of 2nd wave packet - Logarithmic - 4 mm plate . . . . .	44
5.17	Abs. value of the detected pulse - Logarithmic - 3 mm tilted plate . . . . .	46
5.18	Waterfall plot of the detected pulses - Normalized - 3 mm tilted plate . . . . .	47
5.19	Maximum amplitude of the wave packets as function of $x$ -position - Logarithmic - 3 mm tilted plate . . . . .	47
5.20	Amplitude of 1st wave packet - Logarithmic - 3 mm tilted plate . . . . .	49
5.21	Beam profile of 1st wave packet - Logarithmic - 3 mm tilted plate . . . . .	49
5.22	Amplitude of 2nd wave packet - Logarithmic - 3 mm tilted plate . . . . .	50
5.23	Beam profile of 2nd wave packet - Logarithmic - 3 mm tilted plate . . . . .	50
5.24	Amplitude of 3rd wave packet - Logarithmic - 3 mm tilted plate . . . . .	51
5.25	Beam profile of 3rd wave packet - Logarithmic - 3 mm tilted plate . . . . .	51
5.26	Waterfall plot of the simulated pulses - Normalized - 3 mm plate - Flat aperture function . . . . .	52
5.27	Snapshots from COMSOL - 3 mm plate - Sine aperture function . . . . .	54
5.28	Abs. value of the simulated pulse - Logarithmic - 3 mm plate . . . . .	55

5.29	Waterfall plot of the simulated pulses - Normalized - 3 mm plate . . . . .	56
5.30	Maximum amplitude of the wave packets as function of distance to the transducer - Logarithmic - COMSOL - 3 mm plate . . . . .	56
5.31	Snapshots from COMSOL - 4 mm plate - Sine aperture function . . . . .	58
5.32	Abs. value of the simulated pulse - Logarithmic - 4 mm plate . . . . .	59
5.33	Waterfall plot of the simulated pulses - Normalized - 4 mm plate . . . . .	59
5.34	Maximum amplitude of the wave packets as function of distance to the transducer - Logarithmic - COMSOL - 4 mm plate . . . . .	60
6.1	Maximum amplitude of the first wave packet for the three measurements and the simulations . . . . .	62





# Abbreviations

**BeCaLoS** The Behind Casing Logging Set-up

**CAST-V** Circumferential Acoustic Scanning Tool-Visualization

**CBL** Cement Bond Logging

**CET** Cement Evaluation Tool

**FEM** Finite Element Method

**LLW** Leaky Lamb Waves

**NCS** Norwegian Continental Shelf

**NTNU** Norwegian University of Science and Technology

**P&A** Plug and Abandonment

**P-C** Pitch-Catch

**P-E** Pulse-Echo

**PET** Pulse Echo Tool

**SNR** Signal-to-Noise Ratio

**SSPA** Scandinavian Symposium on Physical Acoustics

**USI** UltraSonic Imager



# 1

## Introduction

Since the drilling of the first exploration well on the Norwegian Continental Shelf (NCS) during the summer of 1966 and the discovery of oil at Balder in 1967, the work on the NCS has played a big part in the Norwegian economy. These two events help mark the beginning of Norway's petroleum era together with what is thought to be one of the biggest contributions to Norway's success story, namely Phillips' discovery of Ekofisk, one of the largest offshore fields ever discovered, in 1969. Since the discovery of Ekofisk a series of major discoveries have been made on the NCS, including the drilling of more than 4200 development wells and more than 1500 exploration wells [21, 22].

Drilling for oil and gas contains risks, e.g. due to the extreme pressures that can occur in the hydrocarbon bearing reservoirs. Hence, after the drilling of an oil or gas well has been completed, a cementing job has to be conducted to prevent uncontrolled hydrocarbon migration from the reservoirs to the surroundings, to ensure that the production efficiency can be maximized, and to ensure that the safety requirements are satisfied. The cement job involves the placing of a cement sheath in the annulus between the borehole wall and the casing. To control that a cementing job has been conducted properly, a cement job evaluation has to be conducted. Among methods used for cement evaluation is the use of acoustic techniques and a more extensive introduction to well cementing, cement evaluation as well as a brief history of various acoustic techniques used in cement job evaluation will be presented in the following chapters. The pitch-catch (P-C) technique used during the ultrasonic experiments conducted in this thesis will be presented in Chapter 3 together with the Lamb wave.

When planning the costly plug and abandonment (P&A) job, where the well is cemented for permanent abandonment, it is important to have good information about the cement sheath already placed in the annulus. The costs of the P&A may reach up to 25% of the total drilling cost [15], hence it is important to plan the job properly to avoid additional costs. Many of the methods used today to conduct a cement job evaluation only concerns single-casing geometries, inspecting the properties of the material outside the first casing. To use these methods in geometries with e.g. double-casing geometries, the inner casing must be removed to gain access to the outer pipe which is a costly and time-consuming process [32]. Using a method which makes it possible to inspect the cement through multiple layers would therefore be preferable. Statoil along with other oil companies has previously expressed the need of these tools, e.g. via their Innovate program [28]. This aspiration about wanting to analyze the cement through multiple casing layers is what inspired the work on this thesis and a set of measurements and simulations were planned to evaluate the possibility of using broadband wave propagation in plates to inspect a cementing job quality. An experimental verification of the work done by Viggen, Johansen and Merciu (2016 [32]), showing that multiple Lamb wave packets are excited in a double-casing geometry, were planned. A set of measurement inspecting the plate wave behavior in a double-casing, off-centered geometry was also conducted in this thesis. The experimental lab work were conducted on a Statoil funded setup developed by SINTEF Petroleum Research in Trondheim to analyze broadband wave propagation in plates. The experimental setup and the methods used are described in Chapter 4, followed by the results of the measurements and the discussion of the results. The conclusions and recommendations for further work are given in the last chapter of this thesis.

During the fall of 2015 the author conducted a project at the Norwegian University of Science and Technology (NTNU) about a related subject [29]. Some of this unpublished work was used as a basis for the background material in Chapter 2 and 3.

# 2

## **Well Cementing and Cement Evaluation**

When the cementing job has been completed at a newly drilled oil or gas well, the cement sheath has to meet several requirements concerning both environmental and safety aspects as well as requirements regarding the efficiency of the production of oil or gas. The main objective of the primary cement sheath in an oil or gas well has always been to provide zonal isolation between the different zones, but the sheath has also other purposes, e.g. providing mechanical support in the well [5]. To evaluate the cement before starting the production at a well or as a part of planning the P&A job is important as an improperly functioning sheath can lead to additional economical expenses to the responsible company as well as huge environmental consequences. As the number of aging fields in the North Sea are increasing more wells have to be plugged and abandoned [18], and a demand for better, more cost efficient cement evaluation tools is present.

### **2.1 Purpose of well cementing**

The main objective of primary cementing has always been to create zonal isolation between the different zones, preventing hydrocarbons to leak from the reservoirs to the surrounding environment. Other important purposes of the primary cementing varies according to which part of the casing string it supports, see Figure 2.1. For the conductor casing the cement sheath's purpose is to prevent erosion of the formation by using cement to stop the fluid circulation outside the casing. The cementing of the surface casing is conducted to support the deeper casing strings as well as to seal and protect water formations. Intermediate string's cement sheath must

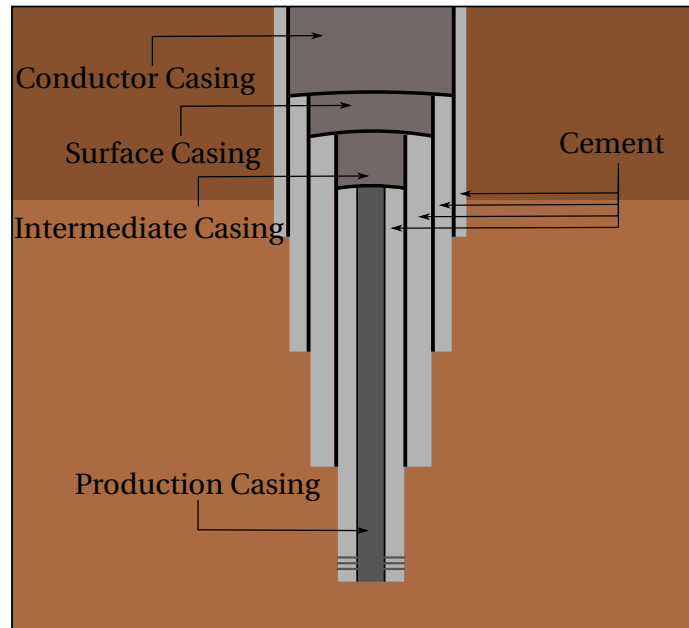


Figure 2.1: Illustration showing the different casing strings of an oil or gas well.

seal abnormally pressured formations, shut off lost-circulation zones, and isolate incompetent formations. The production string is cemented mainly to ensure zonal isolation and to prevent fluid migration in the annulus. When evaluating a cement job, the verification of a proper zonal isolation in the well is of greatest importance [2].

The operation of placing a successful cement sheath is difficult and requires proper planning. To conduct the operation in the right manner, it is important to have a working knowledge of the pressure mechanics regarding the placement of the cement slurry and good information about the well conditions. The two broad categories which the causes of poor cement jobs can be classified into are:

- flow problems of mechanical origin and
- degradation of the cement slurry during the curing stage.

The flow problems of mechanical origin include inefficient preflushing of the annulus, a poorly centralized pipe in the well, washed out holes, and an improper flow regime. These are problems that may occur following an incomplete mud removal, which again can lead to the cement slurry not being placed properly, leaving areas without cement, see Figure 2.2. Degradation of the cement slurry during the curing stage may lead to pollution of the cement sheath, where

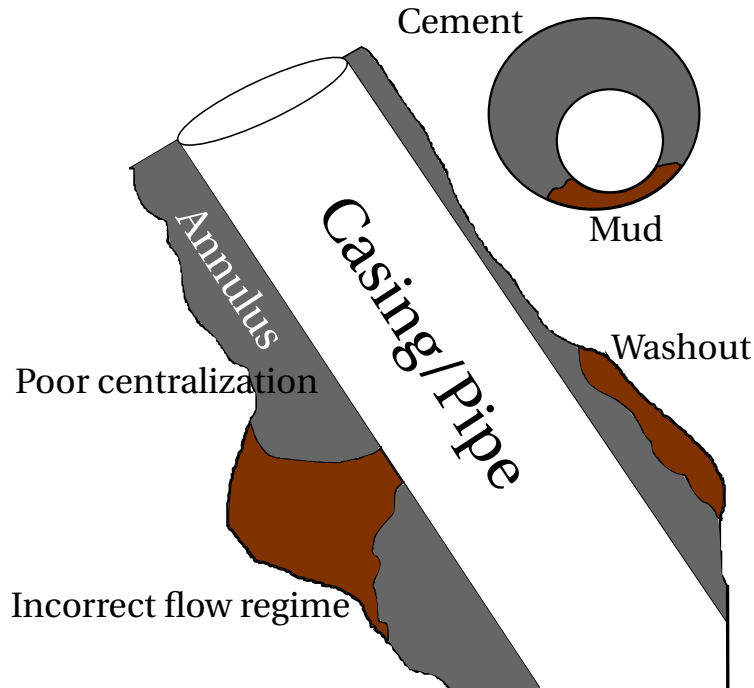


Figure 2.2: An illustration showing different cement slurry displacement problems. The illustration is adapted from Fig. 5.1 in Schlumberger's Well Cementing book [3].

differential pressure between the cement pore pressure and the formation pressure can cause cement failures, leading to the cement being polluted by formation fluids or by an inflow of gas [3]. The challenges and problems regarding the placing of a cement sheath are described further in Section 2.2.

## 2.2 Challenges

The conditions in the well during the curing stage of the cement slurry placed in the well are crucial. As shown in laboratory measurements, the permeability of the cement may increase from the order of 0.001 mD, which is the case of well cured cement, to permeabilities as high as 1 to 5 mD in poorly cured cement. If gas is allowed to migrate within the slurry before it has been cured completely, the pore structure will be partially destroyed and the gas will generate a network of tubular pores which can reach up to 0.1 mm in diameter. Comparing the poorly cured cement to properly cured cement, which has a pore size of less than  $2\mu\text{m}$ , the poorly cured cement will be able to provide a mechanical support to the casing, but the network of

pores lead to the cement having a high permeability, and hence not providing the required seal to the formation gas in the well. Uncontrolled flow of reservoir fluids behind the casing may lead to serious problems, e.g. blowouts, with environmental damages as a consequence [7]. Just in the US, it is estimated that more than \$50 millions are used annually on remedial work to fix issues related to cement failures [6]. The field of adding additives to the cement slurry to prevent the problems that occur during the curing stage is therefore an important field with continuous research being conducted. Both the problems of degradation of the cement during the curing stage and the problems of mechanical origin, leading to e.g. washouts, will influence the properties of the cement sheath and will effect the main function of primary cementing - the zonal isolation [3]. Even though the cementing slurry is properly placed during the cement job and the sheath initially satisfy the requirements regarding isolation, downhole condition changes can induce stresses that can destroy the integrity of the cement sheath, leading to loss of zonal isolation [26].

To inspect whether the objective of placing a proper cement sheath has been achieved, sonic and ultrasonic logging tools are used to both inspect the cement-to-casing bond and to detect the presence of channels within the cement sheath [4]. Some of these acoustic tools and the methods used will be described in Chapter 3.



# 3

## Ultrasonic Logging

To document that the requirements regarding the cementing of oil and gas wells have been fulfilled, the cement job has to be evaluated after completion. A way of evaluating the cement is through the use of acoustic methods, as they can provide information about the cement placed in the annulus between the borehole wall and the steel casing. This chapter will present two techniques used, the pulse-echo technique and the pitch-catch technique, as well as a brief summary of the history of ultrasonic applications used in the oil industry.

### 3.1 History

*The following brief summary of the ultrasonic logging history is based on Schlumberger's Well Cementing book, chapter 15, section 15-4.5.1 - History [2].*

The first use of ultrasonic applications in well logging was through the introduction of the Borehole Televiwer by Zemanek and Caldwell in the 1960s. The Borehole Televiwer tool (1969) used the ultrasonic pulse-echo (P-E) technique to image the borehole wall. The P-E technique will be presented in Section 3.2. The ultrasonic tools operates high frequencies, typically in the range from 200 kHz to 700 kHz, much higher than conventional cement bond logging (CBL) tools (about 20-30 kHz). While investigating methods to evaluate cement behind a pipe, Havira developed the ultrasonic Cement Evaluation Tool (CET) for Schlumberger (1979; 1982), Figure 3.1a. The CET has 8 transducers placed around the circumference with 45° intervals, using the P-E technique to map the acoustic impedance of the material around the pipe. In the following years Froelich *et al.* (1981) and Dumont *et al.* (1984) described the tool and used it to present field test results [8]. Finlayson *et al.*(1984) and Catala *et al.* (1984) described the results of the CET further, where Catala *et al.* proposed to merge the interpretations of the CET

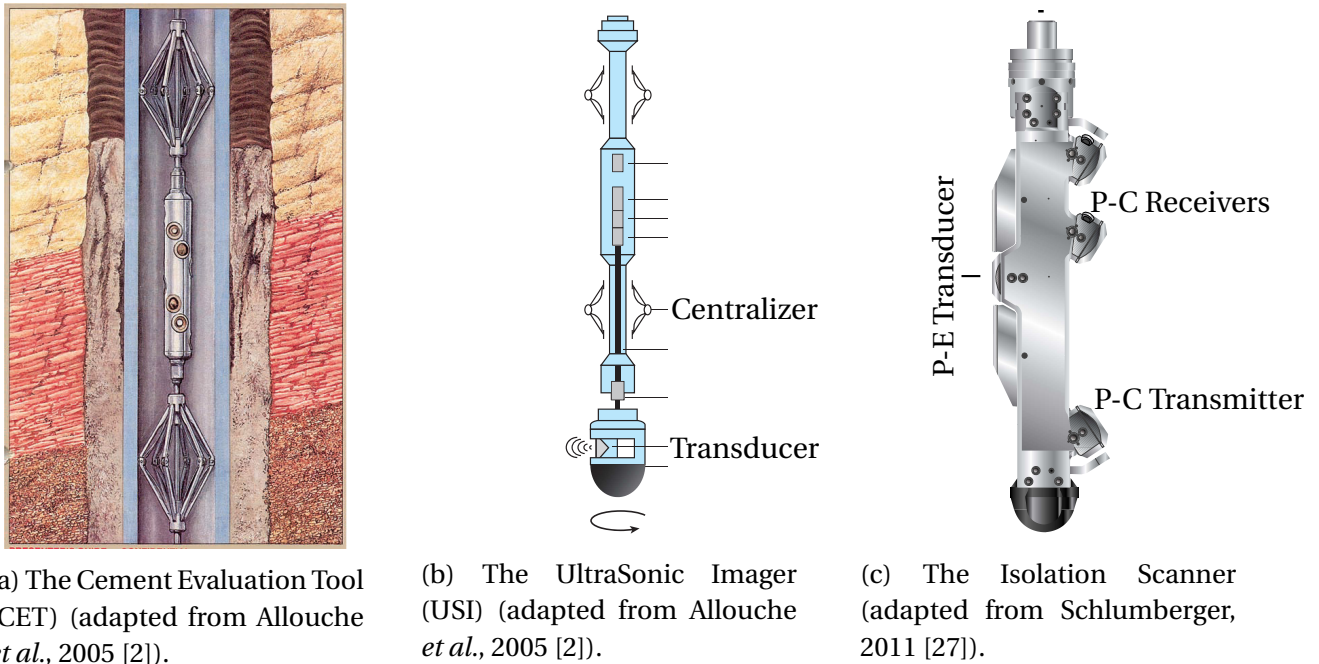


Figure 3.1: Illustrations showing three generations of ultrasonic tools for cement evaluation developed by Schlumberger.

and CBL tools to overcome the individual limitations of each of the two tools. Some years after the CET was introduced, the Pulse Echo Tool (PET) by Gearhart Industries was introduced by Shieves *et al.* (1986). In 1991, Hayman *et al.* of Schlumberger introduced the UltraSonic Imager (USI), a second-generation ultrasonic tool that used a single rotating transducer to give a full coverage of the whole circumference of the pipe with a greater accuracy, Figure 3.1b. Together with the similar Circumferential Acoustic Scanning Tool-Visualization (CAST-V) developed by Graham *et al.* for Halliburton, these tools made the early CET and PET devices to become obsolete. Since the early 1990s, statistical processing of the ultrasonic images has become more common, e.g. with Harness *et al.* (1992) and Graham *et al.* (1994) which made statistical analyses of PET data to improve the ability to evaluate low-density and complex cements. Butsch *et al.* (1995) proposed a statistical method for interpretation of the data from the USI tool, making the tool able to discriminate between cement with gas and fluid channels. The P-E technique limitations regarding the differentiation between light-weight cement and mud in the annulus, as well as the limitations regarding the detection of defects within the cement sheath or at the cement/borehole wall interface, prompted the need for a new ultrasonic cement evaluation tool [31]. This demand was met by Schlumberger through their new tool, the Isolation Scanner,

which was presented by van Kuijk *et al.* of Schlumberger in 2005 [20], Figure 3.1c. The Isolation Scanner includes one transducer for P-E measurements along with one ultrasonic transmitter and two receivers, using the Pitch-Catch technique (see Section 3.3) to do measurements on the media in the annulus [27].

## 3.2 The pulse-echo method

The P-E technique that is used in many of the devices mentioned in Section 3.1 is presented in the following section, with a small discussion on the strength and weaknesses of the P-E technique summarized at the end. An illustration of the P-E technique can be seen in Figure 3.2.

*The following derivations are based on Schlumberger's Well Cementing book, chapter 15, Section 15-4.5.5 - Measurements and Processing [2].*

The physics of the P-E method are derived using the assumption that the ultrasonic wave is planar and traveling perpendicular to a flat plate. The flat plate represents the casing used in oil and gas wells. In the P-E technique, one ultrasonic transducer is used both as transmitter and receiver. The transducer emits a relative short ultrasonic pulse with a limited bandwidth propagating perpendicular towards the casing and the wave being reflected back from the casing is then detected by the same transducer. As the transducer is immersed into the casing fluid while emitting a wave towards the plate or casing, the impedances of the materials given as

$$Z = \rho \cdot v \quad (3.1)$$

are of interest. Here,  $\rho$  is the density and  $v$  the compressional velocity of the respective material. The impedances of the two materials at the boundary are used to calculate the fraction of incident acoustic pressure that is transmitted into the second media,  $K_{\text{trans}}$ , and the fraction reflected back into the first media,  $K_{\text{ref}}$ . The reflection coefficient is given by the formula

$$K_{\text{ref}} = \frac{Z_2 - Z_1}{Z_2 + Z_1} \quad (3.2)$$

and the transmission coefficient by

$$K_{\text{trans}} = 1 + K_{\text{ref}} = \frac{2Z_2}{Z_2 + Z_1}. \quad (3.3)$$

Calculating the intensity of the acoustic wave in a media of impedance  $Z$  as

$$I = \frac{p^2}{Z}, \quad (3.4)$$

leads to energy conservation at the interface between the two media. The  $p$  given in equation (3.4) is the acoustic pressure of the wave. Since there is one transducer functioning as both the transmitting and receiving transducer, the arrival time of the first pulse which is detected will give information about the distance between the transducer and the casing. If the tool is properly centered, this will give information about the casing radius. The fraction of pressure that is reflected back at the boundary is given by equation (3.2) and the fraction of the pressure wave is transmitted into the casing by equation (3.3). The pressure wave that is transmitted into the casing will bounce back and forth inside the casing. At each reflection inside the casing, either at the interior/casing interface or at the casing/annulus interface, some of the energy are lost to the outside material, making the detection of a echo train after the first reflection possible. The time separation between the maximas in the train of pulses,  $\Delta t$ , is given as a function of the thickness of the casing,  $h_{\text{csg}}$ , and the compressional velocity in the casing,  $v_{\text{steel}}$ , and can be calculated as follows

$$\Delta t = \frac{2 \cdot h_{\text{csg}}}{v_{\text{steel}}}. \quad (3.5)$$

The resonance frequency of the casing,  $f_0$ , can then be calculated as

$$f_0 = \frac{1}{\Delta t} = \frac{v_{\text{steel}}}{2 \cdot h_{\text{csg}}}. \quad (3.6)$$

By matching the frequency of the transducer with the resonance frequency of the casing, the amplitude of the train of pulses is maximized and the P-E technique give the best results. The four measurements that can be done in a P-E measurements are the measurement of the main echo amplitude, the transit time of the main echo, the time delay in the resonance ringing, and the form of the resonance. The magnitude of the main echo measured can give usefull infor-

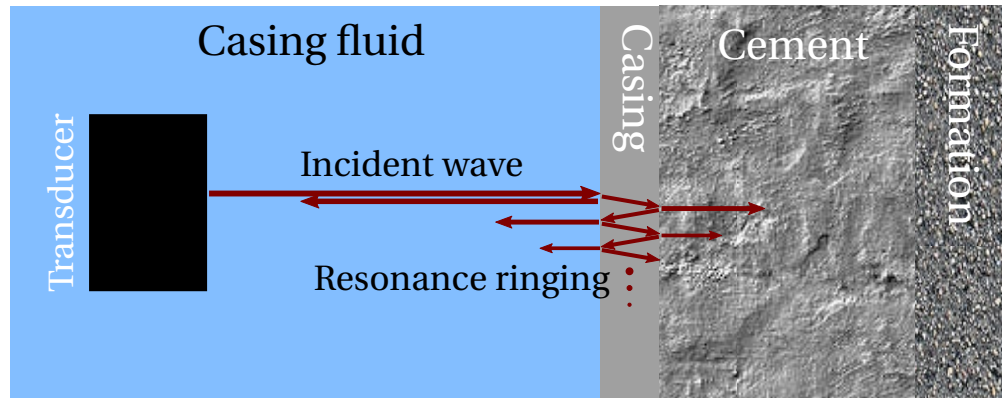


Figure 3.2: An illustration of the Pulse-Echo technique.

mation about the pipe rugosity, making it a tool for quality control of the pipe. By analyzing the resonance signal the thickness of the pipe and the impedance of the material behind the pipe can be calculated [10], while the transit time of the main echo can be used to find the internal radius of the pipe.

### Summary

The P-E technique can be used to calculate both the casing thickness and the impedance of the material in annulus, immediately behind the casing. Due to the high impedance difference between steel and the cement outside the pipe, only a small fraction of energy is transmitted into the material in the annulus. The small fraction of energy transmitted and the small differences between the impedance of some light-weight cements and the impedance of mud make the P-E technique not suitable for cases with light-weight cement. The P-E technique also has limitations concerning the radial resolution, where the measurements are sensitive to the region immediately behind the casing but do not provide information about defects within the cement sheath or at the cement-formation interface [31]. Hence, it is useful to consider the use of other inspection methods to evaluate the cement in the annulus, such as the Pitch-Catch method described in Section 3.3.

### 3.3 The pitch-catch method

The concept of the pitch-catch method involves the excitation of Lamb waves in the oil well casing. The Lamb wave which first was introduced by Horace Lamb in 1917 in his publication *On Waves in an Elastic Plate* [17] will therefor be introduced the following in section, followed by an explanation of the pitch-patch method in Subsection 3.3.2.

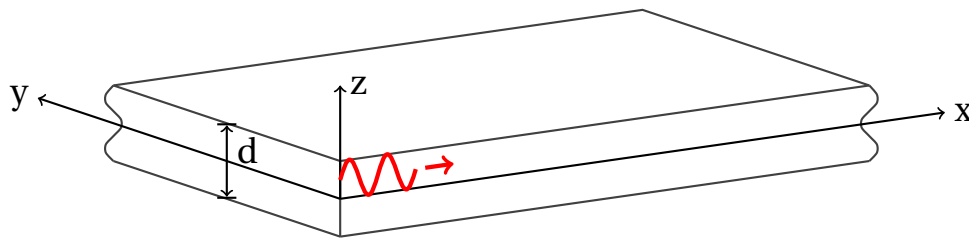


Figure 3.3: Sketch of a plate having infinite length in  $x$ - and  $y$ -direction and thickness  $d$  in  $z$ -direction. The propagation direction of the Lamb wave is in  $x$ -direction and is illustrated by the red line.

#### 3.3.1 The Lamb wave

In his book *Rayleigh and Lamb waves: physical theory and applications* (1967 [34]), Igor Viktorov did further work describing the Lamb waves. In chapter II.1 - The Concept of Lamb waves he wrote: "*Lamb waves refer to elastic perturbations propagating in a solid plate (or layer) with free boundaries, for which displacement occur both in the direction of wave propagation and perpendicular to the plane of the plate.*" In other words does the Lamb waves have no particle motion in the  $y$ -direction, lying in the plate - perpendicular to the particle direction, as illustrated in Figure 3.3. Potential movement in the  $y$ -direction are caused by the vertically polarized shear waves. In the derivation of Lamb wave theory, the assumption that the Lamb waves propagate in an infinitely unbounded plate lying in the  $xy$ -plane has been made. When the frequency of the pulse emitted from the ultrasonic transducer is sufficiently high (80 kHz or more), the area where the incident pulse interacts with the casing is sufficiently small so that the approximation holds for the curved casing [31].

The material from Hovem [13], Løvstad [19], and Viktorov [34] have been used in the deriving of the Lamb wave theory.

In the deriving of the Lamb wave theory, it is useful to use the convention of expressing the vector for the particle displacement in a solid,  $\mathbf{u}$ , as a function of the scalar potential,  $\phi$ , and the vector potential,  $\Psi$ , as

$$\mathbf{u} = \nabla\phi + \nabla \times \Psi, \quad (3.7)$$

where the scalar potential gives origin to the equations regarding longitudinal wave motion and the vector potential to the shear wave motion. The potentials satisfy their respective wave equations:

$$\begin{aligned} \frac{\partial^2 \phi}{\partial x^2} + \frac{\partial^2 \phi}{\partial z^2} + k_l^2 \phi &= 0, \\ \frac{\partial^2 \Psi}{\partial x^2} + \frac{\partial^2 \Psi}{\partial z^2} + k_t^2 \Psi &= 0, \end{aligned} \quad (3.8)$$

where the wave numbers for the longitudinal and the transverse modes are  $k_l = \omega \sqrt{\rho/(\lambda + 2\mu)} = \omega/c_l$  and  $k_t = \omega \sqrt{\rho/\mu} = \omega/c_s$ , respectively. The wave numbers are given by the angular frequency,  $\omega$ , the density of the medium,  $\rho$ , and the elastic Lamé constants,  $\lambda$  and  $\mu$  [35].  $c_l$  is the longitudinal (compressional) velocity and  $c_s$  is the shear wave velocity. The wave equations are independent, hence the compressional waves does not affect the shear waves, and *vice versa* (Hovem, page 480 [13]). Since the Lamb waves have no particle motion in the  $y$ -direction (Figure 3.3), only the particle displacements in  $x$ - and  $z$ -direction are considered, given as

$$\begin{aligned} u_x &= \frac{\partial \phi}{\partial x} - \frac{\partial \psi}{\partial z}, \\ u_z &= \frac{\partial \phi}{\partial z} + \frac{\partial \psi}{\partial x}. \end{aligned} \quad (3.9)$$

In a homogeneous, isotropic solid, the stress has six independent components due to the symmetry requirements for the shear strain. To investigate the particle motion in  $x$ - and  $z$ -direction,

the three stress components

$$\begin{aligned}\sigma_{xx} &= (\lambda + 2\mu) \left( \frac{\partial^2 \phi}{\partial x^2} + \frac{\partial^2 \phi}{\partial z^2} \right) - 2\mu \left( \frac{\partial^2 \phi}{\partial z^2} + \frac{\partial^2 \psi}{\partial x \partial z} \right), \\ \sigma_{zz} &= (\lambda + 2\mu) \left( \frac{\partial^2 \phi}{\partial x^2} + \frac{\partial^2 \phi}{\partial z^2} \right) - 2\mu \left( \frac{\partial^2 \phi}{\partial z^2} - \frac{\partial^2 \psi}{\partial x \partial z} \right), \quad \text{and} \\ \sigma_{xz} &= \mu \left( 2 \frac{\partial^2 \phi}{\partial x \partial z} + \frac{\partial^2 \psi}{\partial x^2} - \frac{\partial^2 \psi}{\partial z^2} \right)\end{aligned}\tag{3.10}$$

are of interest [13]. The Lamb waves particle displacement given as in equation (3.7) as a function of the potentials  $\phi$  and  $\Psi$ , can then be further evaluated. By using the potentials

$$\begin{aligned}\phi &= A_x f_x(z) e^{i(\omega t - kx)} \quad \text{and} \\ \psi &= A_z f_z(z) e^{i(\omega t - kx)}\end{aligned}\tag{3.11}$$

and applying the boundary conditions for the stresses ( $\sigma_{xz}, \sigma_{zz} = 0$  at  $z = \pm d/2$ ) when inserting the potentials from equation (3.11) into equation (3.10), gives a set of equations [34]. When solving the system of equations the symmetric and anti-symmetric wave number,  $k_n$  can be found by calculating the roots of

$$\frac{\tan\left(\frac{qd}{2}\right)}{\tan\left(\frac{pd}{2}\right)} = -\frac{4k_n^2 pq}{(q^2 - k_n^2)^2},\tag{3.12}$$

and

$$\frac{\tan\left(\frac{qd}{2}\right)}{\tan\left(\frac{pd}{2}\right)} = -\frac{(q^2 - k_n^2)^2}{4k_n^2 pq}\tag{3.13}$$

respectively. Here,  $p$  and  $q$  are defined as

$$\begin{aligned}p &= \sqrt{\left(\frac{\omega}{c_l}\right)^2 - k_n^2} \quad \text{and} \\ q &= \sqrt{\left(\frac{\omega}{c_s}\right)^2 - k_n^2}.\end{aligned}\tag{3.14}$$

The symmetrical and anti-symmetrical wave numbers describe the properties of the two infinite sets of Lamb wave modes, whose velocity depend on the relationship between the wavelength



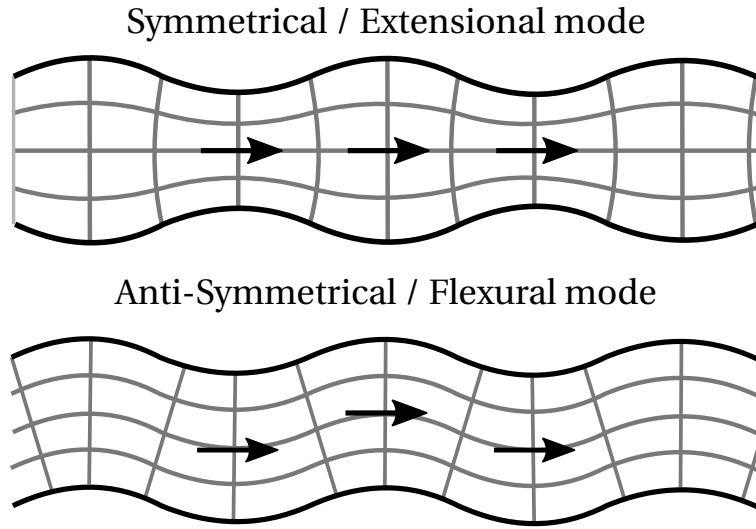


Figure 3.4: Illustration of the particle displacement in the symmetrical and anti-symmetrical Lamb wave modes.

and the plate thickness [19]. The two different types of Lamb waves, the symmetrical and the anti-symmetrical are illustrated in Figure 3.4. The dispersion curves for phase and group velocities can then be calculated numerically by solving equation (3.12) and (3.13) for different frequencies, finding all the corresponding wave numbers and inserting the wave numbers into the equation for the phase velocity

$$c_p = \frac{\omega}{k} \quad (3.15)$$

and the group velocity

$$c_g = \frac{\partial \omega}{\partial k}. \quad (3.16)$$

An example of dispersion curves for a 3 mm thick steel plate are shown in Figure 3.5, adapted from the work done by Løvstad, 2012 [19]. In Figure 3.5 the thicker black lines indicate the horizontally polarized shear waves which can be found when the scalar potential in equation (3.11) vanishes, that is  $u_x = u_z = 0$  (see Figure 3.3). The horizontally polarized shear waves will not be further discussed in this thesis. The nascent frequencies, seen as the cut-off frequencies in Figure 3.5 (a) and (b), correspond to the resonant frequency of the plate and can be calculated as

$$f = \frac{nc}{2d}, \quad (3.17)$$

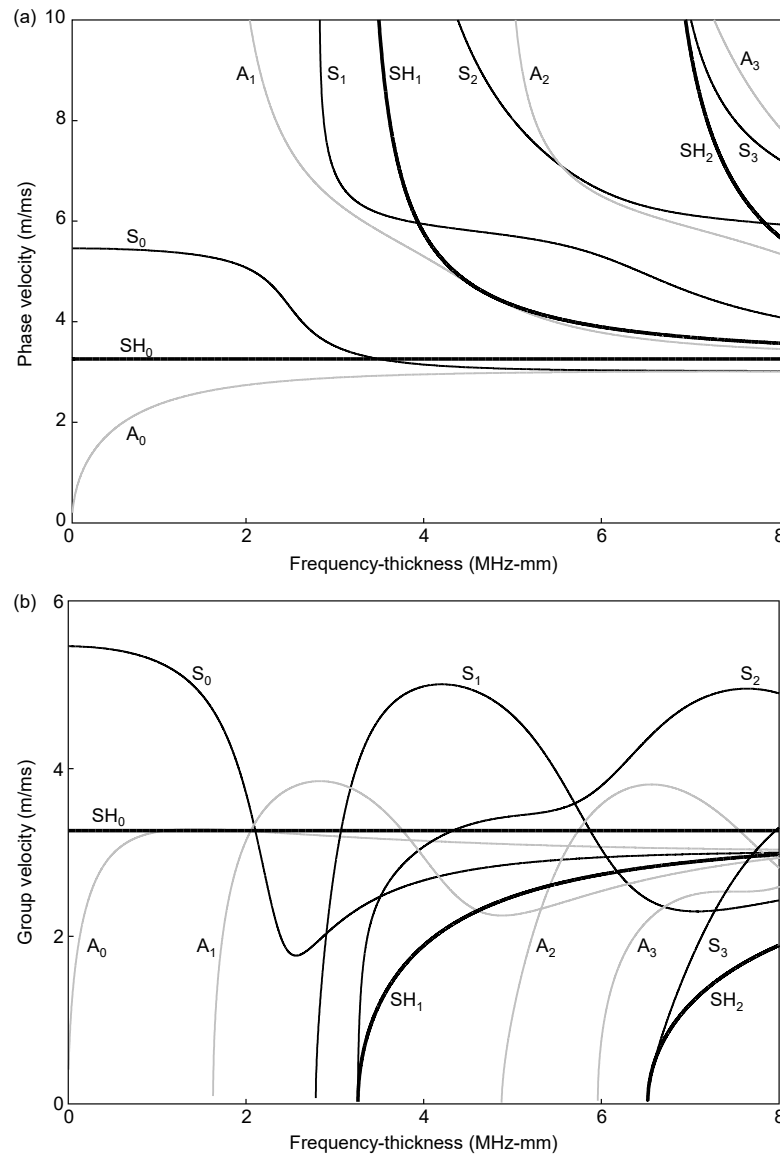


Figure 3.5: Dispersion curves for a 3 mm thick steel plate. Figure (a) shows the phase velocities and (b) the group velocities as a function of frequency thickness. Reproduced from Løvstad, 2012 [19]

where  $n$  is any positive integer. Only the 0th order mode are present for low frequencies with higher order modes being "born" at the corresponding nascent frequencies. The compressional velocity and the shear wave velocity can be inserted in equation (3.17) for  $c$ , giving a set of nascent frequencies for the symmetrical and anti-symmetrical Lamb wave modes respectively [19]. The dispersion curves for a steel plate in water are almost identical to the dispersion curves for the same plate in vacuum [36].

### 3.3.2 The pitch-catch technique

The P-C method involves the use of an ultrasonic transducer which emits a broadband ultrasonic pulse into the casing fluid. As the pulse hits the plate, various Lamb wave modes may be excited. The Lamb wave then propagate in the plate, radiating energy into the surrounding media. Due to the velocity of the plate wave being faster than the compressional velocity of typical casing fluids (1250 - 1650 m/s [31]) the Lamb wave acts as a supersonic sound source, creating a wavefront in the fluid as it propagates in the plate. This wavefront is then detected by a receiver (catcher) and the signal can be analyzed to get information about the downhole conditions in an oil or gas well. A principle sketch of the P-C technique is illustrated in Figure 3.6. The excita-

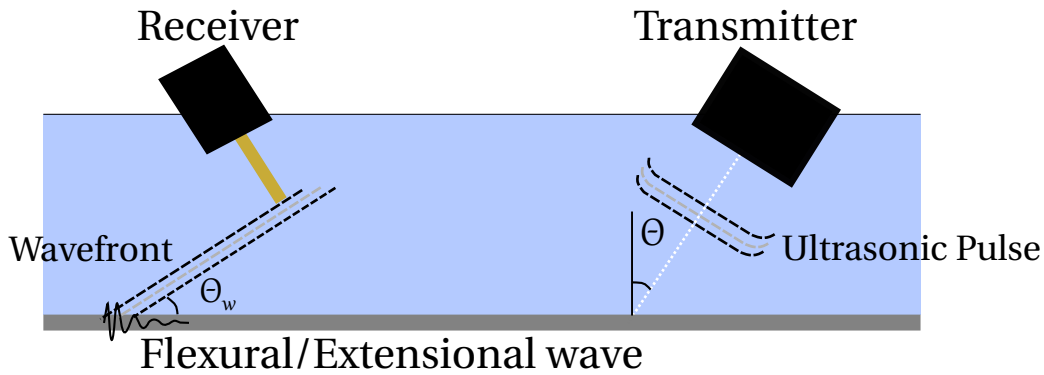


Figure 3.6: A principle sketch of the Pitch-Catch (P-C) method.

tion of the Lamb wave modes are dependent of the incident angle of the pulse, the sound speed in the casing fluid and the phase velocity of the Lamb wave mode in the plate. The optimal incident angle,  $\theta$ , for excitation of one particular Lamb wave mode is given by Snell's law:

$$\sin \theta = \frac{c_f}{c_p}, \quad (3.18)$$

where  $c_f$  is the sound speed in the fluid and  $c_p$  is the phase velocity of the Lamb wave mode [9]. With the typical casing fluids the optimal incident angles are found to be in the range from 28-38° for excitation of the flexural wave. Equation (3.18) assumes a plane incoming wave, which is not the case for the wave emitted by the ultrasonic transducer used in these experiments and equation (3.18) can only be used as an indication of approximately which incident angles which will excite the various Lamb wave modes in the experiment. The angle of which the wavefront

is radiated into the fluid is given by Snell's law (3.18), and hence the receiver should be aligned at this angle to maximize the received signal [31]. This angle is marked  $\theta_w$  in Figure 3.6.

### 3.3.3 The leaky Lamb wave

When a Lamb wave or a set of Lamb wave modes are excited in a plate, they radiate energy into the surrounding media as they propagate in the plate. Due to waves radiation (leakage) of energy into the surrounding media they are often referred to as Leaky Lamb waves (LLW). The symmetrical modes described in Subsection 3.3.1 (Figure 3.4) have particle displacement mainly in the direction of propagation, while the anti-symmetrical modes have particle displacement perpendicular to the propagation direction and the plate [31], giving the modes different properties regarding the attenuation due to energy leakage into surrounding media.

#### Attenuation

The attenuation of the Lamb waves can be caused by several mechanisms, with Wilcox *et al.* (2001) [36] listing the following five mechanisms:

1. signal spreading due to dispersion,
2. signal spreading due to beam divergence,
3. material damping,
4. scattering, and
5. leakage into surrounding media.

The spreading of the signal in the propagation direction, leading to a decaying amplitude of the Lamb wave, is due to dispersion in the plate. The attenuation which is due to spreading perpendicular to the propagation direction is the second attenuation mechanism. This spreading of the plate wave was thoroughly investigated by the author in the work done during the fall of 2015, and some of the results can be seen in the attached article in Appendix B [30]. The attenuation due to the material damping is caused by the energy conversion into heat. This effect can give larger contributions when the Lamb wave propagate in composite materials, but for a

steel plate as used in this thesis, this effect is minimal. The fourth mechanism is applied when using Lamb waves to detect defects as in Alleyne and Cawley's work *The interaction of Lamb waves with defects* (1992 [1]). As previously mentioned, the Lamb wave radiates acoustic energy into the media surrounding the plate and the attenuation caused by this fifth mechanism is dependent on the coupling between the Lamb wave mode in the plate and the surrounding media [36]. For a plate bounded to a solid media, e.g. cement, the situation is complex, with the attenuation being influenced by both the shear and compressional velocities of the connected media. For a fluid media outside the casing, the attenuation due to the outside material is approximately proportional to the acoustic impedance of the fluid [31]. The coupling between the anti-symmetrical waves and the surrounding media is efficient due to the particle displacement being mainly perpendicular to the plate, making the anti-symmetrical modes efficient sound sources [33]. The mechanism of energy leakage into the surrounding media can be massive for certain modes, which can lead to difficulties regarding the signal-to-noise ratio (SNR) in the measurements.

### **Multiple leaky Lamb wave packets**

In a setup with two plates aligned underneath each other, where the ultrasonic transducer excites a Lamb wave in the upper plate (as described in Subsection 4.1.1), the excitation of multiple leaky Lamb wave packets being excited by the energy radiating from the first Lamb wave packet is possible. As the leaky Lamb wave excited by the transducer propagates in the upper plate, it leaks energy into the annulus between the two plates, exciting a second Lamb wave packet in the lower plate. This second Lamb wave packet propagating in the lower plate then leaks energy into the annulus between the plates, leading to an excitation of a third Lamb wave packet propagating in the upper plate, and a train of Lamb wave packets is excited in both of the plates. This effect is described further by Viggen *et al.* [32] and Figure 3.7 is reproduced from this article. In Figure 3.7 the different contributions to the leaky Lamb wave packets amplitudes can be seen, where the Lamb wave packets contribute with energy to all the succeeding wave packets.  $B_1(t)$  is in this figure the leaky Lamb wave excited by the transducer,  $B_2(t)$  the first wave packet in the lower plate,  $B_3(t)$  the second wave packet in the upper plate etc.

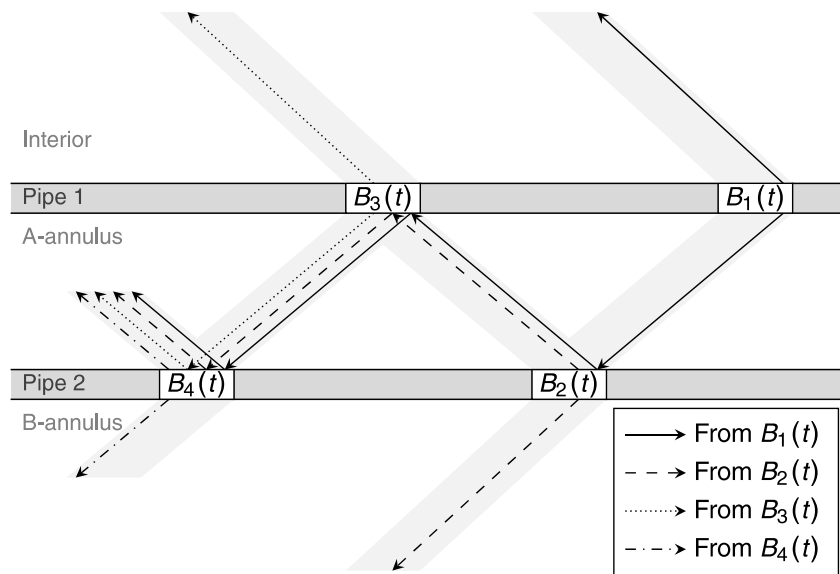


Figure 3.7: Schematic overview of the interaction between leaky Lamb wave packets on two parallel pipes. Arrows show the influence from earlier wave packets on later ones. Reproduced from Viggen *et al.*, 2016 [32].

# 4

## Ultrasonic Lab Experiment

The experimental work was conducted at the Formation Physics Laboratory at SINTEF Petroleum Research in Trondheim, Norway, where the Statoil funded "Behind Casing Logging Set-Up" (BeCaLoS, Figure 4.1) developed by SINTEF was made available to the author to conduct the ultrasonic experiments on. In the experimental work the propagation of the leaky Lamb waves in  $x$ - and  $y$ -direction were of interest, and a set of measurements described in Section 4.3 were conducted to investigate the LLWs behavior. In addition to the experimental work, a set of simulations were conducted which are described in Section 4.4. The experimental work done in this thesis and the work done previously by the author during the fall of 2015 was done using the previous work conducted on the BeCaLoS by Kristian Hoel (2014, [11]) as an inspiration.

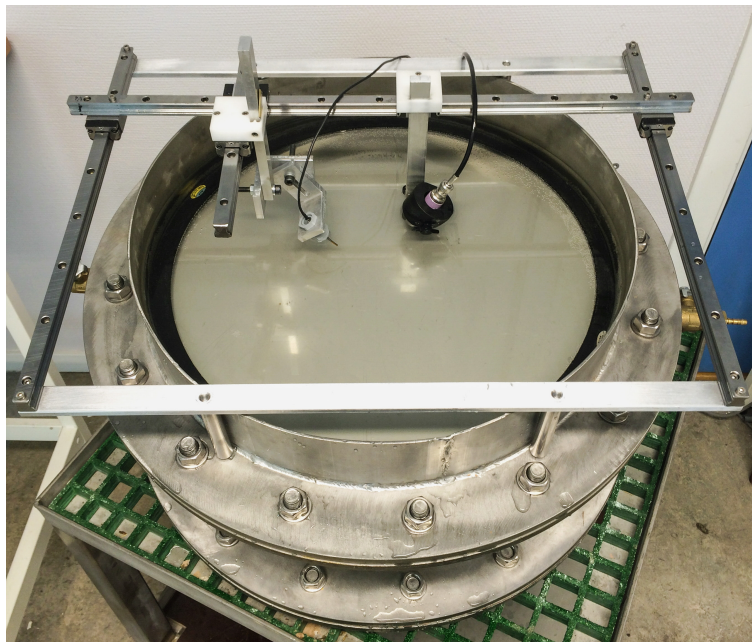


Figure 4.1: The Statoil funded Behind Casing Logging Set-up.

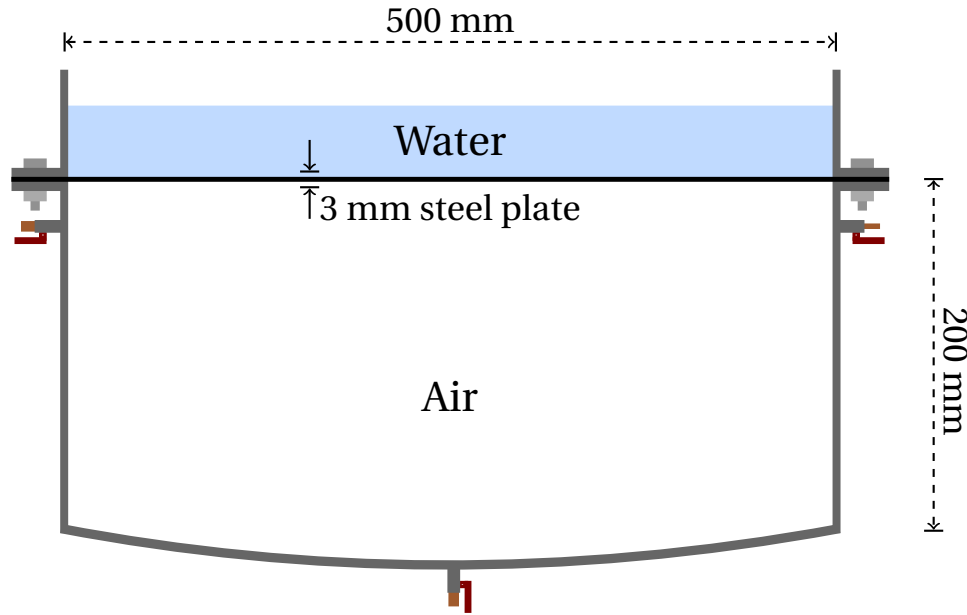


Figure 4.2: Sketch of the BeCaLoS with air as annulus material.

## 4.1 Experimental setup

### 4.1.1 The Behind Casing Logging Set-Up

To replicate an oil well with the possibility to do measurements with different annulus material and different number and thickness of the casings, SINTEF developed the BeCaLoS with funding from Statoil. The BeCaLoS consists of a steel cylinder with a diameter of 500 mm and a length of 200 mm mounted on top of a bottom plate, making it possible to fill the cylinder with different material. At the center of the bottom plate, a valve is placed to make the draining of the BeCaLoS straightforward. Two additional valves are placed on the sides of the cylinder, close to the top, adding options in regard to how to fill the cylinder and to adjust the pressure inside the cylinder. On top of the cylinder it is possible to mount different plates which are to serve as the innermost casing in the oil well case. In the experiments conducted by Hoel [11], a 12 mm thick steel plate was used, while in all the experiments described in this thesis, a 3 mm thick steel plate was used as the innermost casing. To hold the steel plate to the cylinder and to work as a water tank, an open cylinder, also with diameter of 500 mm, was bolted to the first cylinder with a rubber seal placed between the top cylinder and the steel plate to keep the water from leaking. To change the number and type of annulus material as well as the number of casings in the setup, different



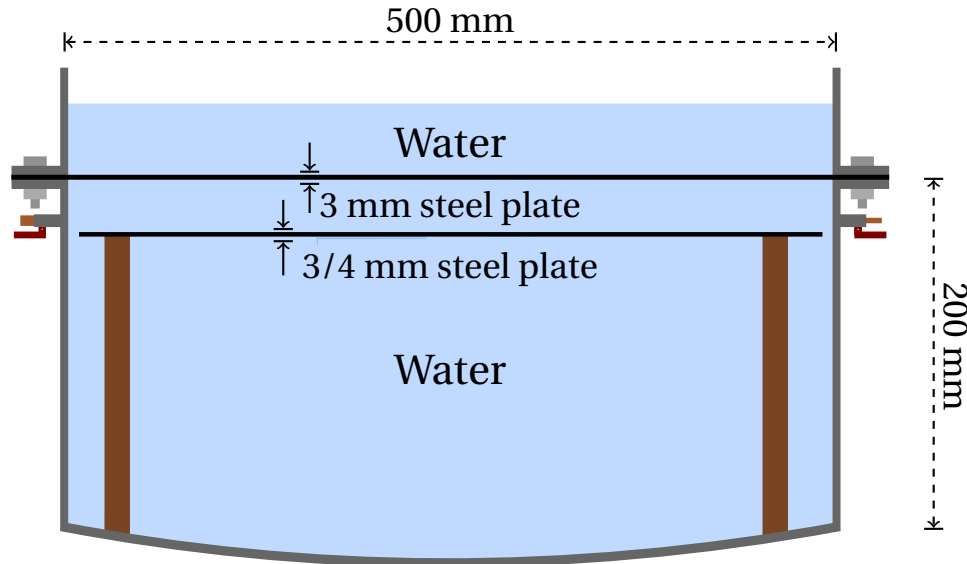


Figure 4.3: Sketch of the BeCaLoS with a second plate mounted inside the BeCaLoS and with water as annulus material. The second plate can also be tilted.

type of material and plates can be placed in the interior of the larger cylinder. In this thesis three configurations of the BeCaLoS were used, two configurations with a 3 mm or 4 mm plate mounted inside the BeCaLoS at a given distance, parallel to the first plate, and one with a 3 mm thick plate mounted at an angle inside the BeCaLoS (Figure 4.3). In all of the three configurations water were used as annulus material.

#### 4.1.2 Transducer and hydrophone holder array

On top of the BeCaLoS, a transducer and hydrophone holder array was placed to make the placing of the transducer and hydrophone relative to each other and the upper plate straightforward. The holder array consists of a frame of four straight rails mounted in a rectangle to form the base. Different rails mounted on ball bearing slider-holders and vertical rails with transducer and hydrophone holders mounted on them, make the placing of the sensors in  $x$ -,  $y$ , and  $z$ -positions simple. The transducer and hydrophone holders also have the possibility to adjust the angle of the respective equipment in the  $xz$ -plane. A sketch of the transducer and hydrophone holder array is shown in Figure 4.4 together with the defined coordinate system used in this thesis. In the rest of this thesis the center of the transducer face is placed at  $x$  and  $y = 0$ , making the  $x$ - and  $y$ -positions of the hydrophone relative to the placing of the transducer.

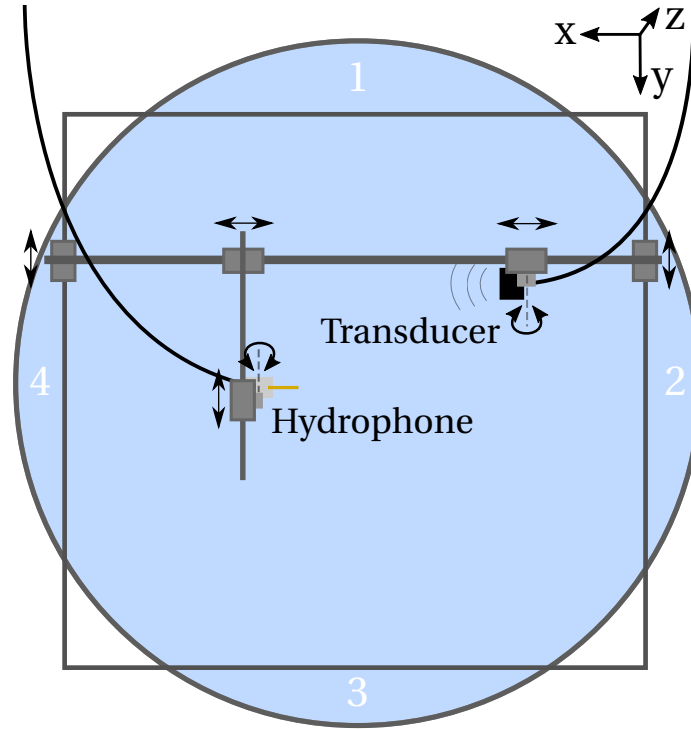


Figure 4.4: Sketch of the transducer and hydrophone holder array. The numbers 1-4 indicates the points where the distance between the two plates were measured during the experimental work.

## 4.2 Experimental equipment

In the ultrasonic experiments conducted an ultrasonic pulser/receiver of the type Olympus Panametrics - NDT 5900PR ([24], Figure 4.5) was used to send an electric pulse to a piezoelectric transducer. The piezoelectric transducer used was a Panametrics C302 Immersion Transducer, made by Olympus IMS ([23], Figure 4.6a), with a nominal element size of 25.4 mm in diameter. The pulse emitted from the transducer is a broadband ultrasonic pulse with a center frequency of 1 MHz. To detect the pressure wave in the casing fluid, a needle hydrophone with a circular element with a diameter of  $500 \mu\text{m}$  of the type HNR-0500 by Onda Corp. ([25], Figure 4.6b) was mounted in the transducer and hydrophone holder array on top of the BeCaLoS. The electric signal from the hydrophone was amplified by the pulser/receiver before it was sent to a digital sampling oscilloscope. The oscilloscope used was a DSO-X 4024A Oscilloscope from Agilent Technologies (Figure 4.5), which through a LabView extension made it possible to log the received signal onto a computer. Matlab 2015b was used to analyze and present the data. To

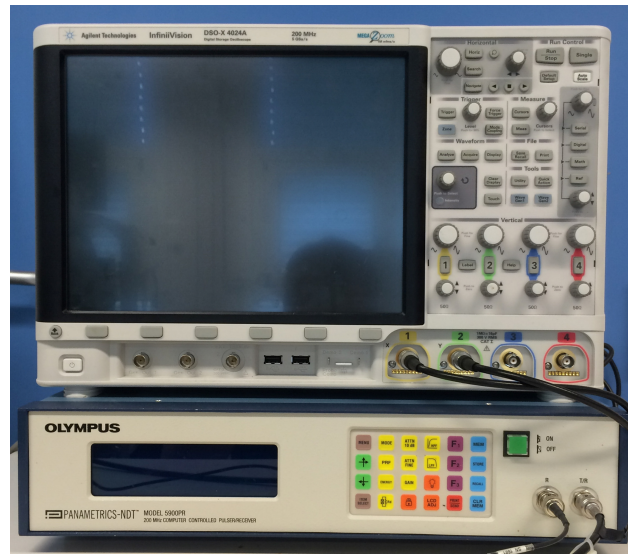


Figure 4.5: The Agilent DSO-X 4024A - oscilloscope (top) and the Olympus Panametrics-NDT 5900PR - pulser/receiver (bottom).

measure the angles of the transducer and the hydrophone as well as the tilt of the whole setup, an application using the internal 3-axis gyroscope in a smartphone was used.



(a) Olympus IMS 1 MHz Immersion Transducer.



(b) Onda Corp. HNR-0500 Hydrophone.

Figure 4.6: The specific transducer and hydrophone used during the ultrasonic experiments at SINTEF Petroleum Research.

## 4.3 Execution

### 4.3.1 Configuration of the setup

During the unpublished work conducted by the author during the fall of 2015 [29], different measurements were done to find the ideal configurations for the BeCaLoS during the measurements. These configurational measurements were conducted on the BaCaLoS with air as annulus material as illustrated in Figure 4.2. The impact of the transducer and hydrophone tilting, as well as the impact of tilting the whole BeCaLoS to make waves reflected at the water-air interface scatter away from the receiver to minimize the disturbance from the water-propagating waves were investigated. Three different water propagating waves are illustrated in Figure 4.7. The optimal transducer tilt ( $\theta_T$ , Figure 4.7) for maximizing the amplitude of the plate wave was found to be around  $30^\circ$  and the hydrophone was adjusted to  $\theta_H = 33^\circ$ . To minimize the influence of the waves being reflected at the water-air interface (as in path (c), Figure 4.7), surface waves were excited at the water-air surface during the time of the measurements. To reduce the disturbances from the water-propagating waves the oscilloscope was configured to take the average of 512 acquired signals.

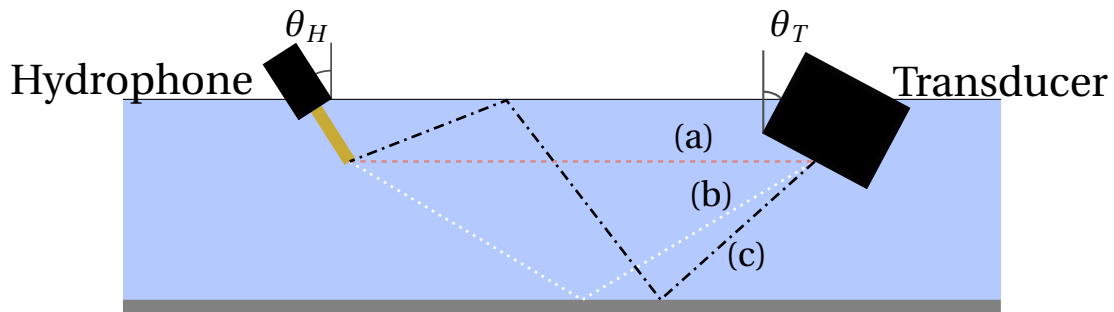


Figure 4.7: A sketch of three of the possible pressure waves propagating through the water from the transmitter to the receiver. Path (a) propagating directly from the transducer to the hydrophone, path (b) being reflected once at the water-steel interface, and path (c) being reflected both at the water-steel and at the water-air interface.

### 4.3.2 Broadband wave propagation in steel plates

To investigate the propagation of leaky Lamb waves in the plates, a set of measurements were done for each of the three BeCaLoS configurations described in Subsection 4.1.1. The measurement set consisted of moving the hydrophone in a grid with the  $x$ -position ranging from 40 to 150 mm with 10 mm intervals and with the  $y$ -position ranging from 0 to 40 mm with 2.5 mm intervals, making a grid of  $12 \times 17$  measuring points. In addition, a set of measurements, moving the hydrophone from  $x = 40$  mm to  $x = 150$  mm with 2.5 mm intervals while keeping  $y = 0$  mm, were conducted. The transducer was held still during all the measurements. To find the distance between the two plates, four measurements were conducted while the upper plate of the BeCaLoS was demounted. The points of the measurements are indicated by the numbers 1-4 in Figure 4.4. For each set of measurements, the tilt of the whole BeCaLoS and the tilting of the transducer and the hydrophone was measured. When measuring with water inside the annulus, the problems occurring with the formation of air bubbles inside the BeCaLoS had to be taken into configuration. As a solution the BeCaLoS was filled with water before it was set to rest for 24 hours before any measurements were conducted. The influence of air bubbles in the setup will be discussed more extensively in Chapter 6.

## 4.4 Simulation setup

To get more information about the broadband wave propagation in the steel plates, a set of simulations were conducted. The finite element method (FEM) solver and simulation software COMSOL Multiphysics 5.2 was used, solving the problems using time-domain simulations. COMSOL was chosen due to the supervisors familiarity with the software and the availability of COMSOL to the author through the Department of Electronics and Telecommunications at NTNU. Time-domain solutions was chosen to be able to follow the pulses in the system for different times. Previously conducted work, e.g. the work by Hora and Červená (2012 [12]), has proven COMSOL to be suitable for time-domain simulations of elastic waves. In COMSOL the acoustics and structural mechanics modules were used while doing the simulations. COMSOL does not require the user to have a deep knowledge about FEM to get useful information

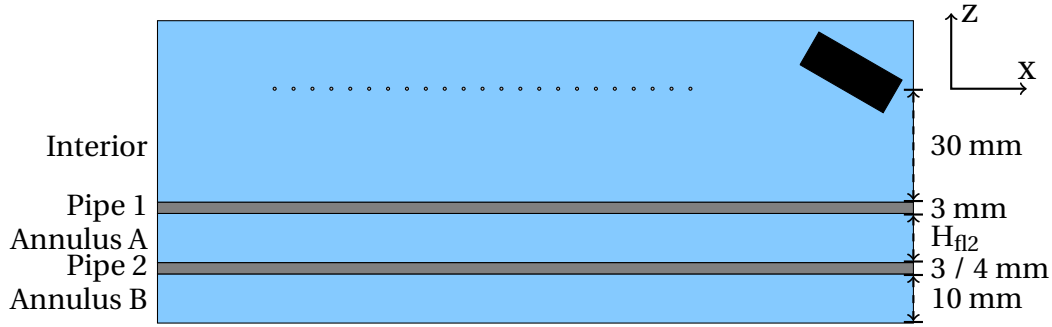


Figure 4.8: Schematic of the 2D simulation setup used in COMSOL Multiphysics.

from the simulations, as it is relatively straightforward to use. The finite element method chapter in the *Computational Methods in Acoustics* compendium written by Kristiansen and Viggen (2011 [16]) was used by the author to understand the principles of FEM and to know the requirements and limitations of simulation software using FEM. A more profound explanation of FEM will not be given in this thesis.

The simulation setup was constructed to replicate the double-casing setup of the first two sets of measurements, with the two plates parallel to each other. In all the simulation runs the thickness of the upper steel plate was 3 mm, with a distance  $H_{fl2}$  of 12 or 13 mm between the plates. The second plate had a thickness of 3 or 4 mm, with distance  $H_{fl2}$  and the thickness of the second plate adjusted according to the respective distances and thicknesses in the experimental measurements. The simulations were conducted in two dimensions at a cross-section lying in the  $xz$ -plane at  $y = 0$ , and the setup is illustrated in Figure 4.8. The implemented transducer was constructed as a rectangular transducer with a flat transducer face, tilted  $30^\circ$  at a height of 30 mm to the center of the transducer face from the first plate. The transducer face had a width of 25.4 mm and the transducer height was 10 mm. The simulated ultrasonic pulse was simulated through the implementation of an inward acceleration boundary condition on the transducer face given by the equation

$$\frac{\partial^2 u_n}{\partial t^2} = A \sin [2\pi f_0 (t - t_p/2)] e^{-\frac{1}{2} \left( \frac{t - t_p/2}{\sigma_t} \right)^2}, \quad (4.1)$$

where  $u_n$  is the displacement normal to the transducer face,  $f_0$  the center frequency of the ultrasonic pulse,  $t_p = 4/f_0$  the pulse length,  $\sigma_t = t_p/8$ , and  $A$  the amplitude chosen as  $A = 1 \text{ m/s}^2$ . The center frequency,  $f_0$ , was set to 1 MHz in the simulations. To reduce the amplitude of the

water propagating wave traveling directly from the transducer to the hydrophone, a set of simulations were also conducted by applying a spatial function to the transducer face acceleration. The displacement at the outer edge were in these simulations set to zero through a sine function as used by Vigen *et al.* (2016 [32]). This aperture function was applied in COMSOL as

$$\frac{\partial^2 u_n}{\partial t^2} = A \sin [2\pi f_0 (t - t_p/2)] e^{-\frac{1}{2} \left( \frac{t-t_p/2}{\sigma_t} \right)^2} \sin (s\pi), \quad (4.2)$$

where  $s$  is a spatial parameter running from 0 to 1 over the length of the transducer face. To compare the simulations with the pressures measured by the hydrophone during the experimental work, the pressure were logged at 23 points placed at a height of 30 mm above the plate, at distances of 40 to 150 mm from the center of the transducer face with 5 mm intervals. The displacement of the upper surface of the two plates in  $z$ -direction as a function of position and time were also logged.

The geometry of the simulation setup was meshed using free triangular elements with maximum element size of  $\lambda_0/6 = (c_w / f_0)/6$ , where  $c_w$  is the sound velocity in the casing fluid, being 1500 m/s for water used in the simulations. A control run was conducted using a maximum element size of  $\lambda_0/10$ , but as the results from this run deviated very little from the simulations using our normal mesh, the maximum element size of  $\lambda_0/6$  were used in the simulations presented in this thesis. The edges of the geometry were set to be low-reflecting boundaries to minimize the energy being reflected back into the system at the edges.





# 5

## Results

In this chapter the results from the ultrasonic experiments along with the simulation results will be presented. Some observations from the measurements will be discussed briefly in this chapter, with a more profound discussion in Chapter 6.

### 5.1 Configuration of the setup

The optimal tilt of the transducer, maximizing the amplitude of the wave front being radiated from the plate wave, was found to be  $30^\circ$ . This angle was used in the experiments conducted in this thesis due to the maximization of the plate wave amplitude and due to the excitation of only the lower order Lamb wave modes. The tilting of the hydrophone was found to have little impact due to the hydrophone's low directivity in the frequency range of interest, and the hydrophone was set to a tilt of  $33^\circ$ . By tilting the whole setup and by exiting surface waves at the water surface, the noise from the waves being reflected at the surface (see path (c), Figure 4.7) was reduced. The work done to find the proper configurations of the setup is described more thoroughly in Talberg, 2015 [29].

### Broadband wave propagation in steel plates

The ultrasonic experiments described in Section 4.3 were conducted to analyze the broadband wave propagation in the steel plates of the setup. The experiment consisted of three set of measurements, each with a second plate mounted inside the BeCaLoS, and the results of the measurements are described in the following three subsections. Some of the setup parameters are

mentioned together with the results, while all the specific configuration details for each set of measurements can be found listed in Appendix A. Following the presentation of the experimental results, the results of the COMSOL simulations can be found in Section 5.3.

## 5.2 Experimental results

### 5.2.1 Second plate: 3 mm thick

The first set of measurements conducted with a 3 mm plate mounted inside the BeCaLoS is presented in this subsection, with the specific configurations of the setup listed in Table A.1.

To inspect the plate wave propagation along the  $x$ -direction, the absolute value of the pulse detected by the hydrophone at 45 measuring points along the  $x$ -axis, ranging from 40 mm to 150 mm with 2.5 mm intervals, were plotted logarithmic as a function of  $x$ -position and time in Figure 5.1. As described in Subsection 3.3.3 and in the work done by Vigggen *et al.* [32], multiple Lamb wave packets are expected to be excited in the plates after some propagation in the  $x$ -direction. This can be seen clearly in Figure 5.1 where the (a)-marker highlights three of these wave packets detected by the hydrophone, with more wave packets following for larger  $x$ -values and later times. These three wave packets are also highlighted by the red (a)-marker in Figure 5.2, where 23 of the pulses detected by the hydrophone along the  $x$ -axis have been plotted with normalized amplitudes as a function of time. The group velocity of the first wave packet was calculated by finding the time delay between the maximum of the envelope for the different measurement points, leading to a group velocity of

$$c_g = 3083.5\text{m/s.}$$

The time difference between the maximums of the successive wave packets in the plate,  $\tau$ , was measured to

$$\tau_1 = 13.077\mu\text{s}, \quad \tau_2 = 12.667\mu\text{s} \quad \text{and} \quad \tau_3 = 12.82\mu\text{s},$$

with  $\tau_1$  being the time between the maximum of the first and second wave packet,  $\tau_2$  between the maximum of the second and third wave packet, and  $\tau_3$  between the maximum of the third

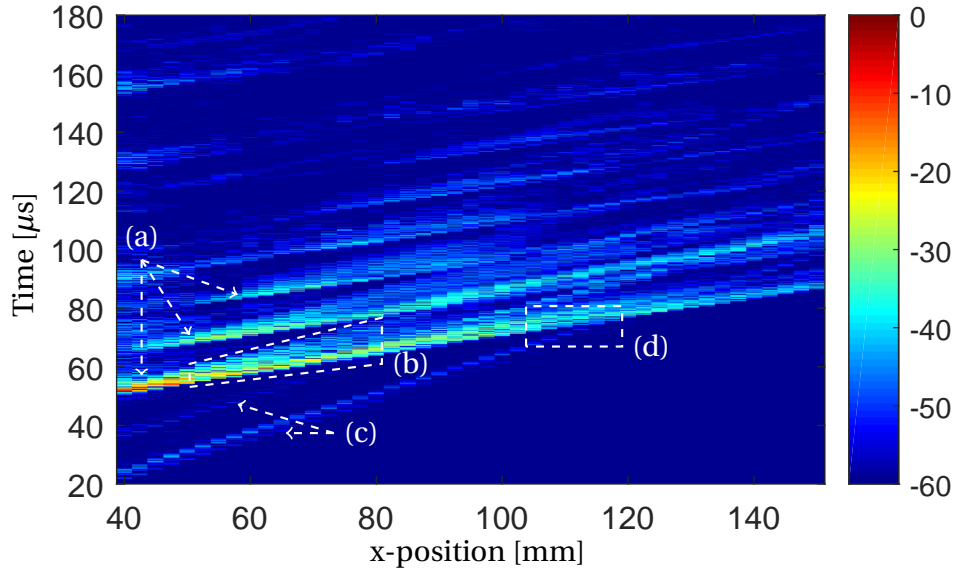


Figure 5.1: The absolute value of the detected pulse plotted logarithmic as a function of  $x$ -position and time.

and fourth wave packet. This time delay is related to the travel time of the water propagating wave, propagating in the fluid layer between the two plates. With a distance between the plates of about 13 mm and a group velocity as calculated above, a time difference of approximately

$$\tau = \left( \frac{2H_{fl2}}{c_w} \right) \cos \theta_w = \left( \frac{2 \cdot 13 \cdot 10^{-3}}{1500} \right) \cos(\arcsin(1500/3083.5)) = 15.14 \mu s$$

would be expected (Hovem, 2012 [14] - equation 5.57). Here,  $\theta_w$  is the angle of which the wave front from the Lamb wave packet is radiated into the surrounding fluid, given by Snell's law (3.18), and  $H_{fl2}$  the distance between the two plates. The measured time difference between the successive pulses are lower than the expected value.

The area marked (b) in Figure 5.1 highlights where it can be observed that the Lamb wave packet widens. This is due to the excitation of multiple Lamb wave modes by the transducer which propagates at different velocities in the plate, as were described in Subsection 3.3.1.

The maximum amplitude of the envelope of the first four wave packets as a function of  $x$ -position are plotted logarithmic in Figure 5.3. The amplitude of the first wave packet is decreasing along the propagation direction, while the other wave packets have their maximums after some propagation in the  $x$ -direction. Doing a linear fit on the amplitude data for the first wave

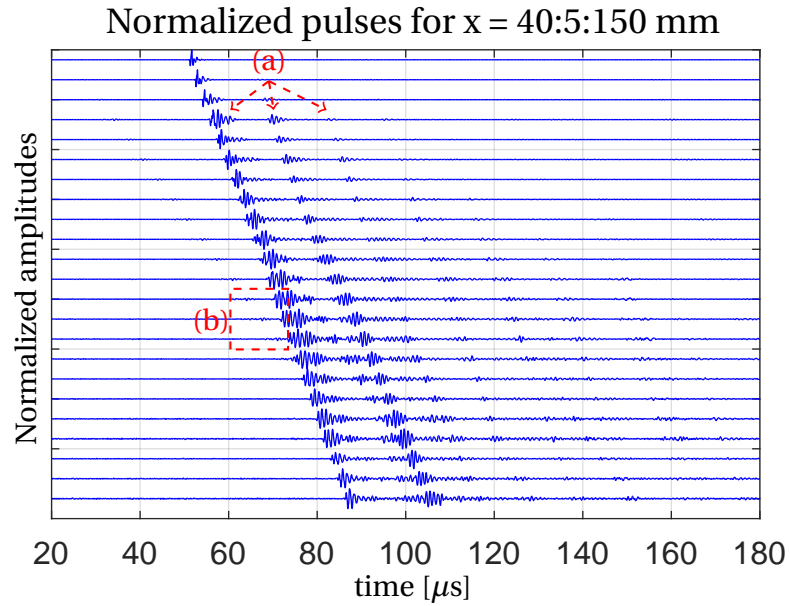


Figure 5.2: Normalized pulses detected by the hydrophone for  $x$ -positions ranging from 40 to 150 mm with 5 mm intervals. The upper line is for  $x = 40$  mm, the second for  $x = 45$  mm etc.

packet gives an attenuation value of 0.251 dB/mm.

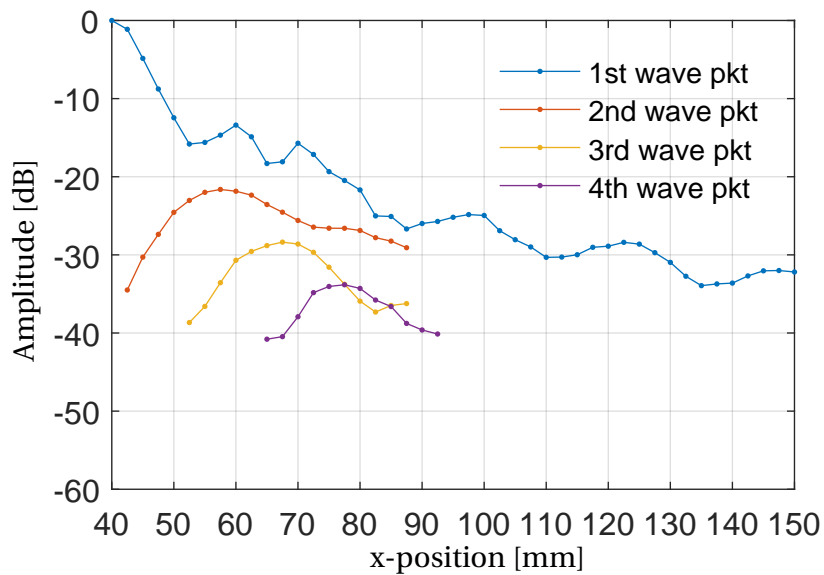


Figure 5.3: The maximum amplitude of the wave packets as a function of  $x$ -position.

### Plate wave spreading

To investigate how the Lamb wave propagates in the plate, the maximum amplitude of the wave packet's envelopes was found for all the measuring points of the hydrophone, described in Section 4.3.

A logarithmic plot displaying the maximum amplitudes of the first Lamb wave packet as a function of  $x$ - and  $y$ -position can be seen in Figure 5.4, where the amplitudes have been normalized against the value at  $x = 40$  mm and  $y = 0$  mm. It can be seen that the amplitudes have their maximum value close to the transducer and that the amplitudes decay fast in  $x$ -direction, as found in Figure 5.3. To investigate the spreading of the wave in  $y$ -direction, the maximum amplitudes for all  $y > 0$  mm were normalized against the corresponding maximum amplitude at  $y = 0$  mm and plotted in Figure 5.5, with a line marking the -6 dB level. This was done to compensate for the attenuation in  $x$ -direction for highlighting the plate wave spreading in  $y$ -direction.

It can be seen in Figure 5.5 that the plate wave propagates mainly in the  $x$ -direction, with little spreading in  $y$ -direction. The area marked (a) in Figure 5.5 is where the time of arrival of the wave propagating directly from the transducer to the hydrophone (following path (a) in Figure 4.7) will coincide with the time of arrival of pulse radiated from the first wave packet. This direct water-propagating wave is marked by (c) in Figure 5.1 and one of the points where the direct wave overlaps with the pulse from the first wave packet can be seen marked by (d) in Figure 5.1 and (b) in Figure 5.2. Close to the  $x$ -axis, this disturbance in the measurements are relatively small compared with the amplitude of the wave front being radiated from the wave packets, but as the amplitudes decay along  $x$ -direction and when measuring for large  $y$ -positions, this disturbance can play a more significant role when analyzing the data.

Analyzing the behavior of the second wave packet by plotting the same two types of plots, where the maximum amplitude of the envelope of the second wave packet detected by the hydrophone as a function of  $x$ - and  $y$ -position, can be seen in Figure 5.6 and Figure 5.7. From Figure 5.6 it can be seen that the amplitude of the second wave packet has its maximum after the first wave packet has propagated some distance in the plate, which was shown for the values along the  $x$ -axis in Figure 5.3. The values for the  $x$ -positions smaller  $x = 50$  mm in Figure 5.7

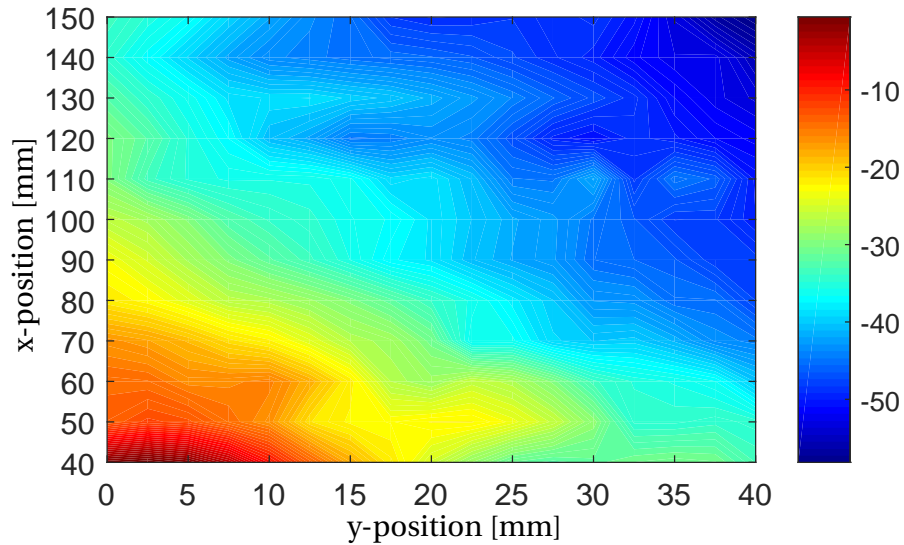


Figure 5.4: The amplitude of the first wave packet plotted logarithmic as a function of  $x$ - and  $y$ -position.

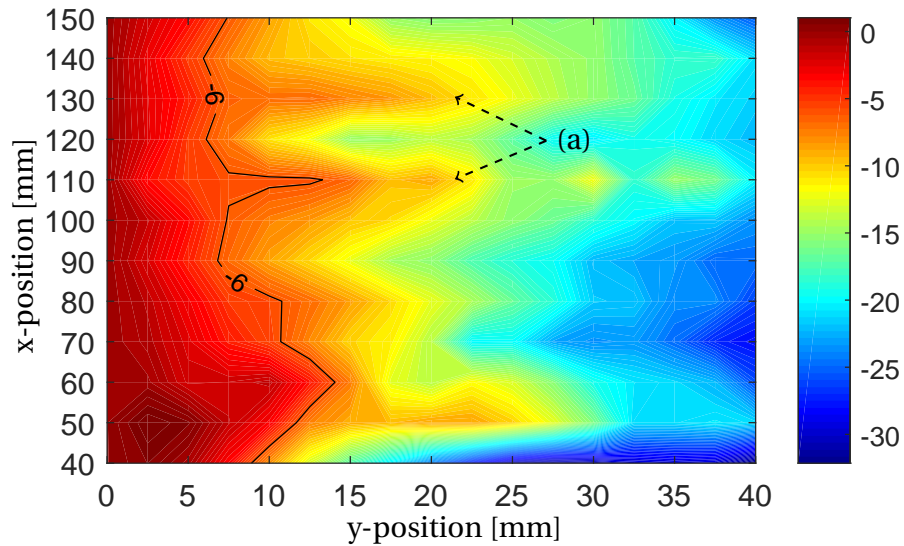


Figure 5.5: The amplitude of the first wave packet normalized against the corresponding value at  $y = 0$  mm. Plotted logarithmic as a function of  $x$ - and  $y$ -position.

are normalized against a maximum amplitude at the  $x$ -axis where the second wave packet is hard to detect, leading to some artifacts in the figure. As discussed for the first wave packet, the water propagating wave disturb the measurements of the amplitudes of the second wave packet at larger  $x$ - and  $y$ -positions, highlighted by (a) in Figure 5.7. By not considering the disturbance highlighted by (a) and the artifacts due to the normalization at small  $x$ -values, it can be seen that

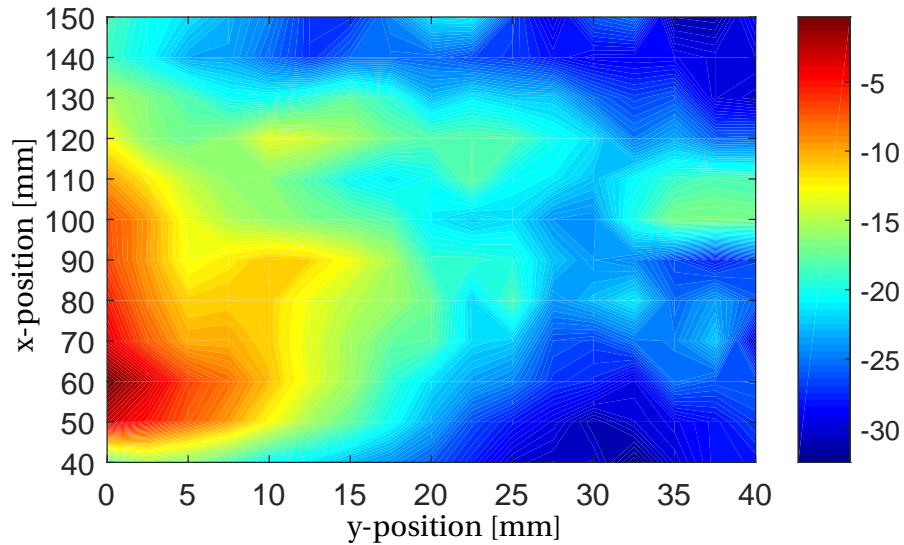


Figure 5.6: The amplitude of the second wave packet plotted logarithmic as a function of  $x$ - and  $y$ -position.

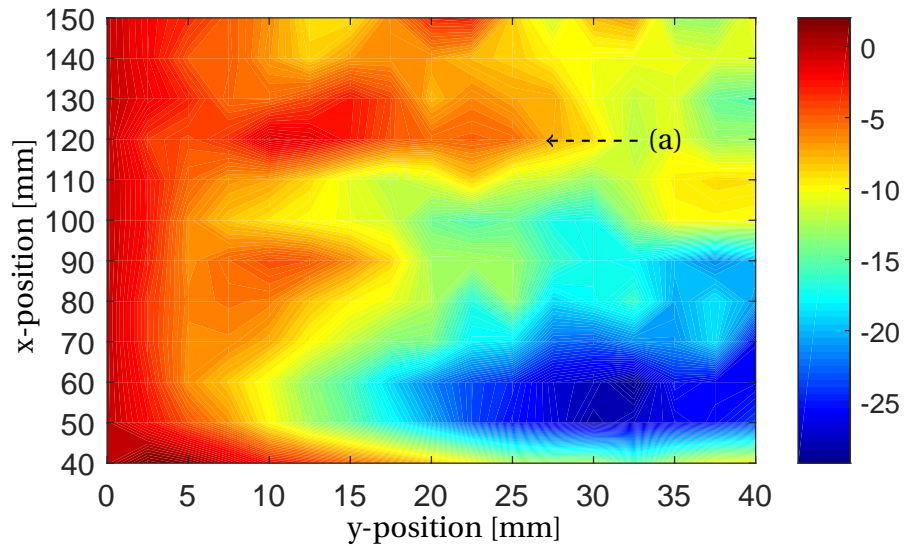


Figure 5.7: The amplitude of the second wave packet normalized against the corresponding value at  $y = 0$  mm. Plotted logarithmic as a function of  $x$ - and  $y$ -position.

most of the energy of the second wave packet propagates in the  $x$ -direction, with little spreading in  $y$ -direction. The third wave packet was also inspected, and the two plots are displayed in Figure 5.8 and Figure 5.9. For  $x$  smaller than 60 mm the amplitude of the third wave packet is very small, or even absent, hence Figure 5.9 show some artifacts for this area when normalizing against the value at  $y = 0$  mm.

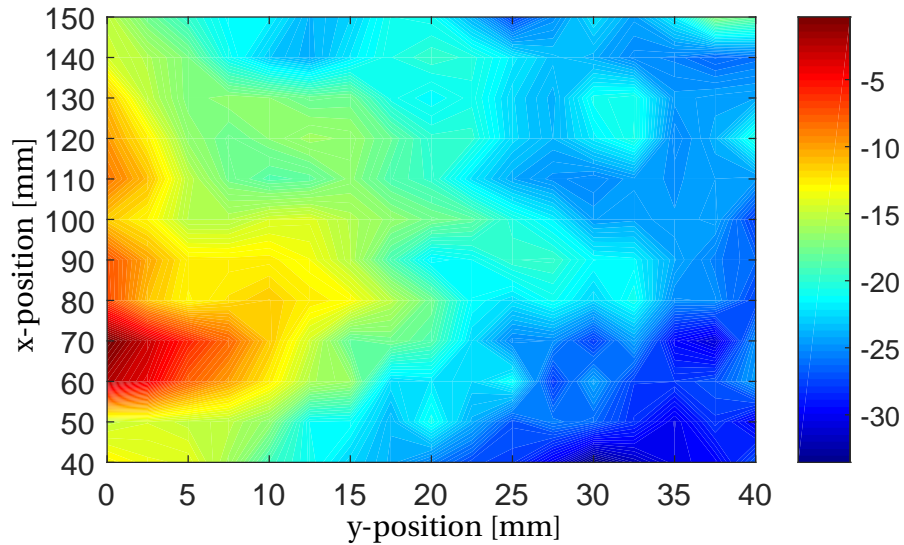


Figure 5.8: The amplitude of the third wave packet plotted logarithmic as a function of  $x$ - and  $y$ -position.

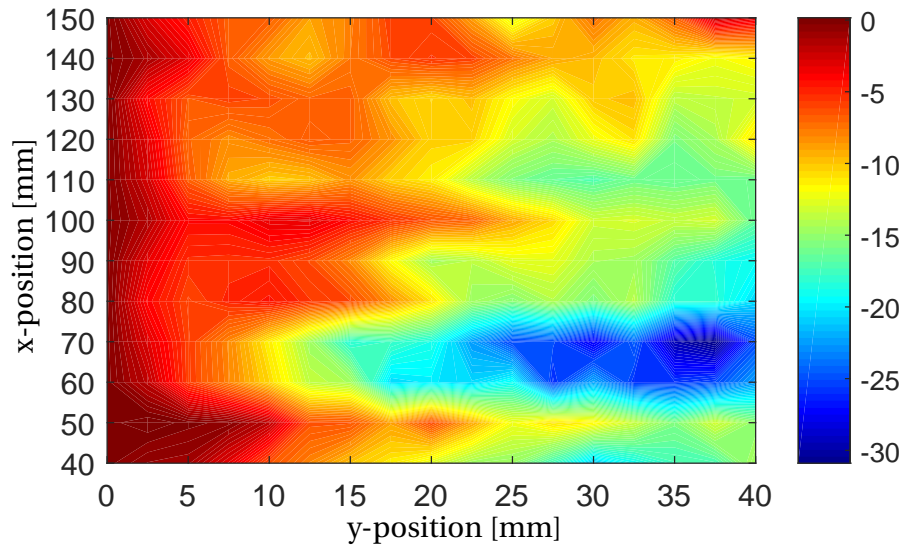


Figure 5.9: The amplitude of the third wave packet normalized against the corresponding value at  $y = 0$  mm. Plotted logarithmic as a function of  $x$ - and  $y$ -position.

Except for the areas where the disturbances from the water-propagating waves interfere with the wave being radiated of the wave packets and the area with artifacts due to the normalization, it can be seen in Figure 5.5, Figure 5.7, and Figure 5.9 that the plate wave propagates mainly in  $x$ -direction, with very little spreading in  $y$ -direction.



### 5.2.2 Second plate: 4 mm thick

The second set of measurements were conducted on the setup with a 4 mm thick plate mounted inside the BeCaLoS, with the specific configuration details listed in Table A.2. The measurements conducted and the calculations presented in this section are in general the same as described in Subsection 5.2.1, hence it will be described a bit more briefly.

To inspect the plate wave propagation along the  $x$ -direction, the absolute value of the measured pulses at  $y = 0$  mm were plotted logarithmic as a function of  $x$ -position and time in Figure 5.10. The excitation of multiple wave packet are harder to detect in this set of measurement, with only two wave packets marked (a) appearing clearly in the figure. The pulses detected for 23 of the measuring points along the  $x$ -axis are displayed in Figure 5.11 with normalized amplitudes as a function of time, and the two wave packets are highlighted by the (a). To find the group velocity the same calculations as in Subsection 5.2.1 were conducted, giving a group velocity of

$$c_g = 2950.1\text{m/s}$$

for the first wave packet. The time difference between the maximums of the first and second wave packet in the plate,  $\tau$ , was calculated to be

$$\tau_1 = 13.203\mu\text{s}.$$

With the group velocity measured and a height between the two plates of about 12 mm, a time difference of approximately

$$\tau = \left( \frac{2H_{fl2}}{c_w} \right) \cos\theta_w = \left( \frac{2 \cdot 12 \cdot 10^{-3}}{1500} \right) \cos(\arcsin(1500/2950.1)) = 13.78\mu\text{s}$$

would be expected.

The area marked (b) in Figure 5.10 highlights where the first wave packet widens as it propagates in the plate. This is due to the excitation of multiple Lamb wave modes which propagates at different velocities in the plate, as described in Subsection 3.3.1.

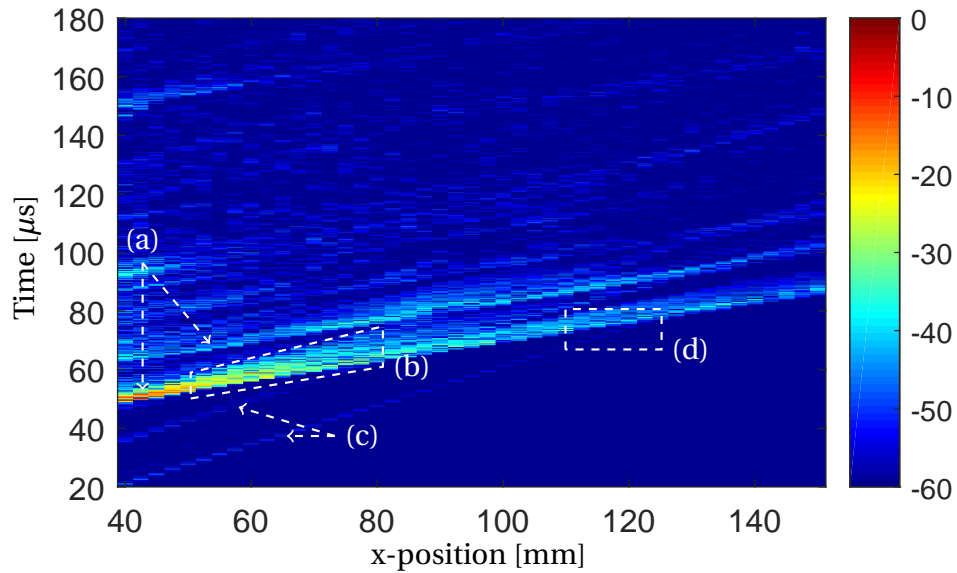


Figure 5.10: The absolute value of the detected pulse plotted logarithmic as a function of  $x$ -position and time.

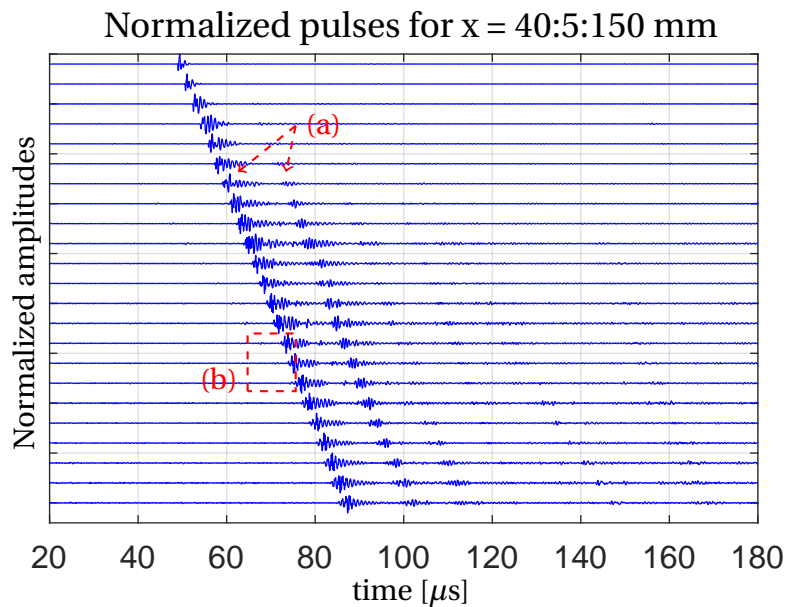


Figure 5.11: Normalized pulses detected by the hydrophone for  $x$ -positions ranging from 40 to 150 mm with 5 mm intervals. The upper line is for  $x = 40$  mm, the second for  $x = 45$  mm etc.

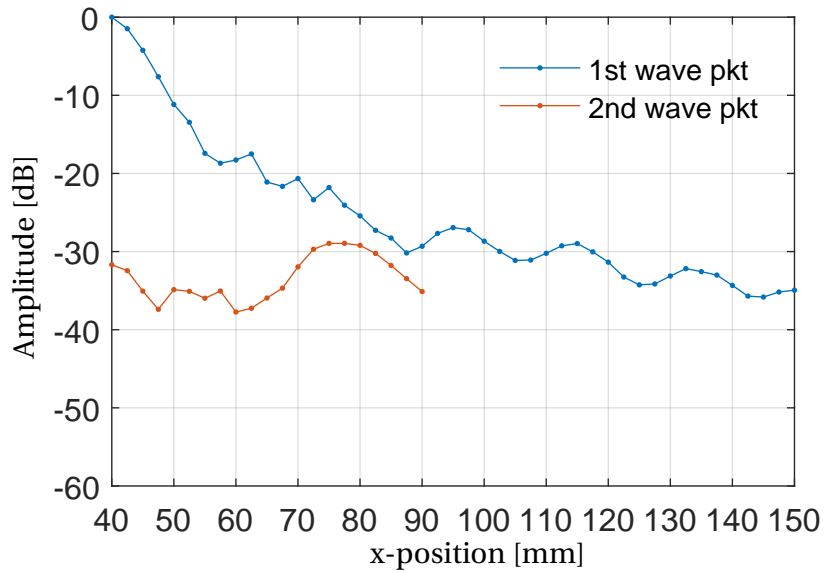


Figure 5.12: The maximum amplitude of the wave packets as a function of  $x$ -position.

The maximum amplitude of the envelopes of the two wave packets are plotted logarithmic as a function of  $x$ -position in Figure 5.12. As observed in the first set of measurements the amplitude of the first wave packet is mainly decreasing along the propagation direction. For the second wave packet the amplitude of the envelope first increases up to  $x = 75$  mm where it has its maximum, before it starts to decrease. By doing a linear fit on the amplitude data for the first wave packet, an attenuation value of 0.256 dB/mm was found.

### Plate wave spreading

To investigate the Lamb wave propagation in the plate, the maximum amplitude of the wave packet's envelope was found for all the measuring points of the hydrophone. For the first wave packet, a logarithmic plot of the maximum amplitudes as a function of  $x$ - and  $y$ -positions is shown in Figure 5.13. In this figure it can be observed that the first wave packet decays relatively fast in the propagation direction, which was displayed for the values along the  $x$ -axis in Figure 5.12. To highlight the spreading of the plate wave in  $y$ -direction, the maximum amplitudes measured for all  $y > 0$  mm were normalized against the corresponding maximum amplitudes at  $y = 0$  mm, compensating for the attenuation in  $x$ -direction. This normalized maximum amplitude plot is plotted logarithmic in Figure 5.14 with a line marking the -6 dB level.

The area marked (a) in Figure 5.14 highlights where the wave propagation directly from the transducer to the hydrophone in the water will interfere with the pulse radiated from the first wave packet. The water-propagating waves propagating directly from the transducer to the hydrophone are marked (c) in Figure 5.10, and one of the areas where it interferes with the pulse from the first wave packet is marked (d) in Figure 5.10 and (b) in Figure 5.11.

To analyze the behavior of the second wave packet, the same two types of plots, showing the amplitude of the second wave packet detected by the hydrophone as a function of  $x$ - and  $y$ -position in Figure 5.15 and the amplitude values normalized against the value at  $y = 0$  mm in Figure 5.16 were plotted. As can be seen in both of the figures, a large value for the second wave packet's maximum amplitude is found at  $x = 60$  mm and  $y = 10$  mm. The origin of this maximum in the measurements is unclear, as no water-propagating wave following path (a) or (b) in Figure 4.7 would interfere with the wave from the second wave packet at this position.

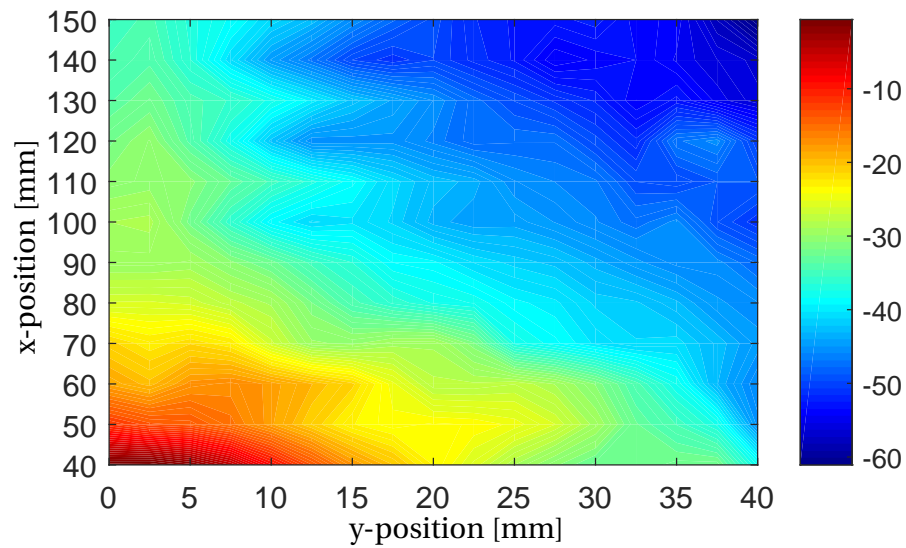


Figure 5.13: The amplitude of the first wave packet plotted logarithmic as a function of  $x$ - and  $y$ -position.

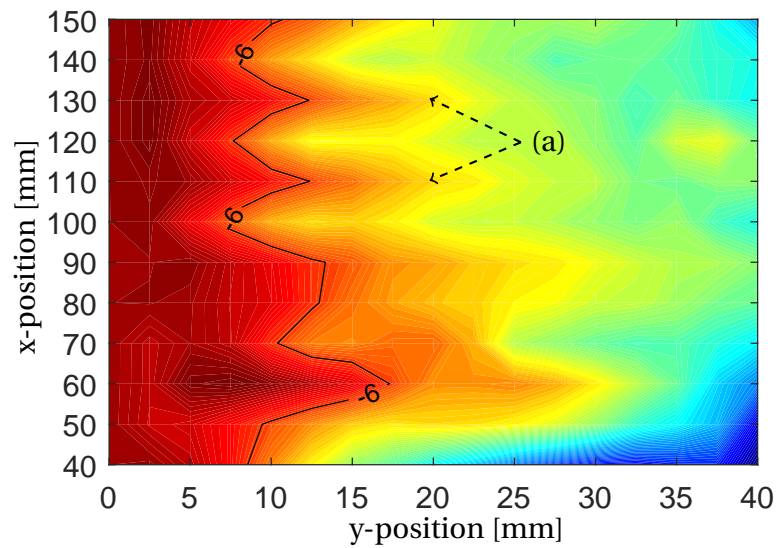


Figure 5.14: The amplitude of the first wave packet normalized against the corresponding value at  $y = 0$  mm. Plotted logarithmic as a function of  $x$ - and  $y$ -position.

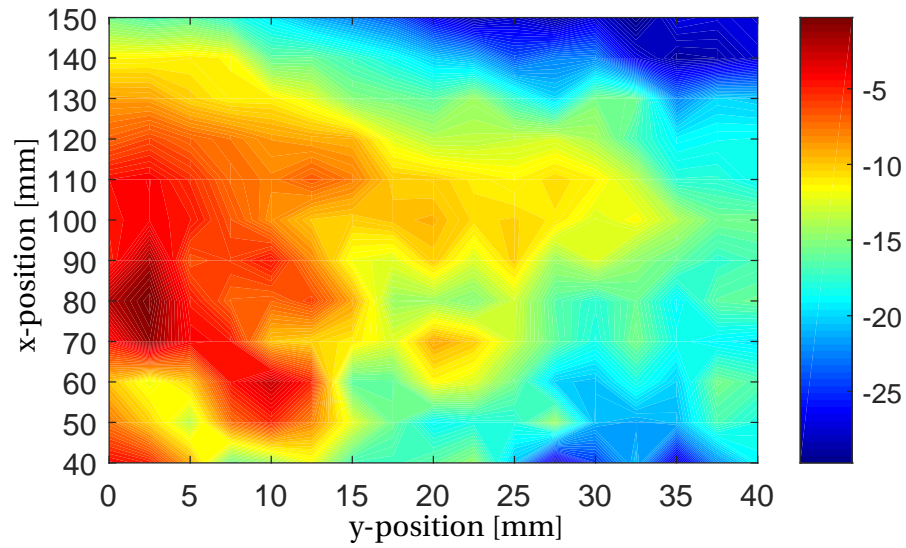


Figure 5.15: The amplitude of the second wave packet plotted logarithmic as a function of  $x$ - and  $y$ -position.

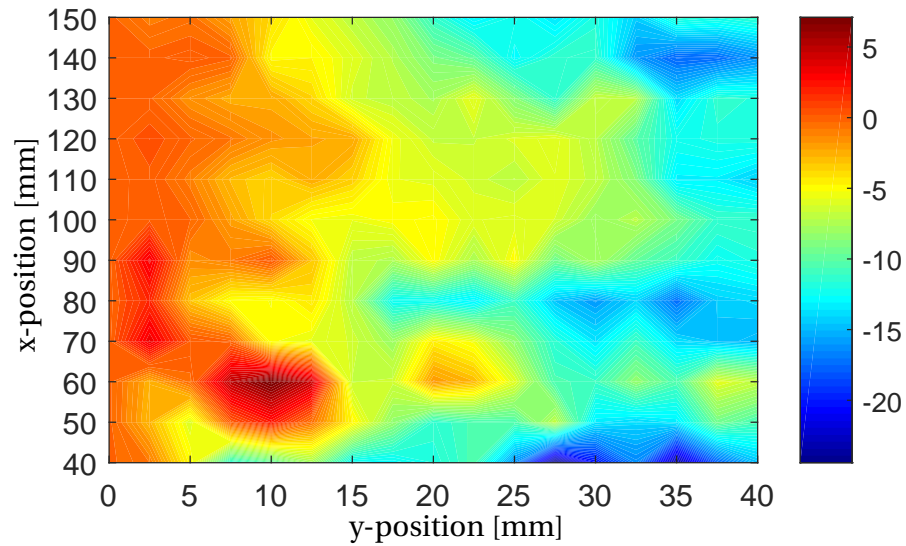


Figure 5.16: The amplitude of the second wave packet normalized against the corresponding value at  $y = 0$  mm. Plotted logarithmic as a function of  $x$ - and  $y$ -position.

### 5.2.3 Second plate: 3 mm thick - tilted

The last experiment was conducted with a 3 mm thick plate mounted with a tilt inside the BeCa-LoS, with the specific configuration of the setup listed in Table A.3. For the distances between the plates as listed in Table A.3, the plate have a tilt of

$$\Theta_{plate} = \arctan\left(\frac{35.32\text{mm} - 8.53\text{mm}}{500\text{mm}}\right) = 3.07^\circ$$

relative to the upper plate. This was confirmed by measuring the tilt using a smartphone application for angle measurements. With the transducer placed 192 mm from edge marked "1" in Figure 4.4, the height between the two plates directly underneath the transducer was

$$8.53\text{mm} + 192\text{mm} \cdot \left(\frac{35.32\text{mm} - 8.53\text{mm}}{500\text{mm}}\right) = 18.82\text{mm}.$$

As in the two previously presented sets of results, the absolute value of the detected pulses for the 45 measuring points lying on the  $x$ -axis are plotted in a logarithmic plot as a function of  $x$ -position and time in Figure 5.17. The marker (a) highlights three wave packets in the figure, with a possible fourth and fifth wave packet being barely observable. In Figure 5.18, 23 of the pulses detected along the  $x$ -axis are plotted with normalized amplitudes as a function of time, where the marker (a) highlights the same three wave packets as the marker (a) in Figure 5.17. By measuring the time delay between the maximums of the first wave packet's envelope as a function of  $x$ -position, the group velocity of the first wave packet was calculated to

$$c_g = 3099.6\text{m/s}.$$

Measuring the time difference between the maximums of the successive wave packets in the plate,  $\tau$ , the values

$$\tau_1 = 20.119\mu\text{s} \quad \text{and} \quad \tau_2 = 19.332\mu\text{s}$$

can be calculated. Here,  $\tau_1$  is the time difference between the first and second wave packet and  $\tau_2$  between the second and third wave packet. With the height between the plates calculated to

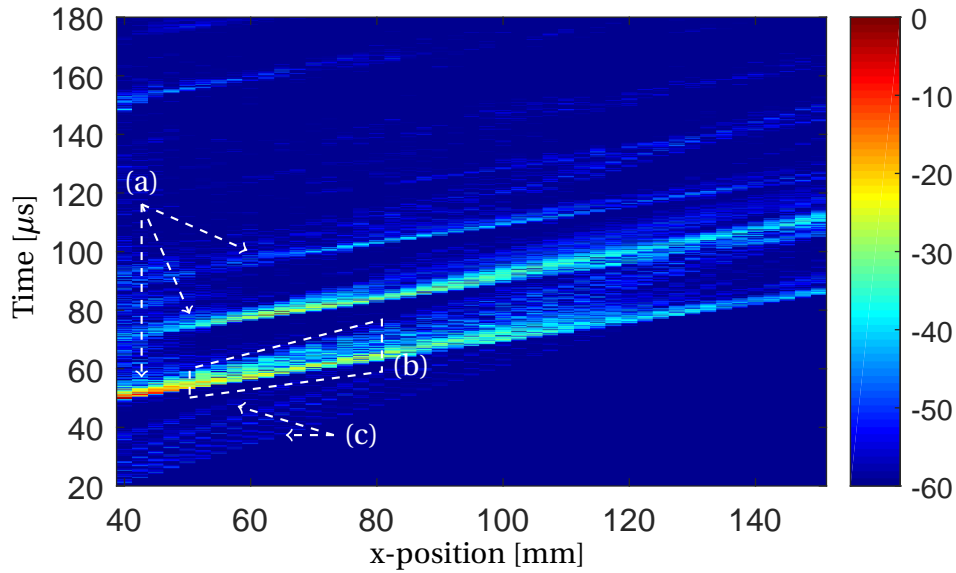


Figure 5.17: The absolute value of the detected pulse plotted logarithmic as a function of  $x$ -position and time.

be 18.82 mm and with the group velocity found, a time difference of approximately

$$\tau = \left( \frac{2H_{fl2}}{c_w} \right) \cos \theta_w = \left( \frac{2 \cdot 18.82 \cdot 10^{-3}}{1500} \right) \cos(\arcsin(1500/3099.6)) = 21.96 \mu s$$

would be expected.

As in the previous subsections, the area marked (b) in Figure 5.17 highlights an area where the Lamb wave packet widens, which is due to the excitation of multiple Lamb wave modes by the transducer. As described in Subsection 3.3.1 the Lamb wave modes propagate at different velocities in the plate, hence the widening of the wave packet.

The maximum amplitude of the envelope of the first three wave packets was then found and plotted logarithmic as a function of  $x$ -position in Figure 5.19. The amplitude of the first wave packet is seen decreasing along the propagation direction, while the other wave packets have their maximums after the wave packets have been propagating a short distance in the  $x$ -direction, and it can even be observed that the maximum amplitude of the second wave packet exceeds the amplitude of the first wave packet at some measuring points. By doing a linear fit on the amplitude data for the first wave packet an attenuation value of 0.265 dB/mm was found.



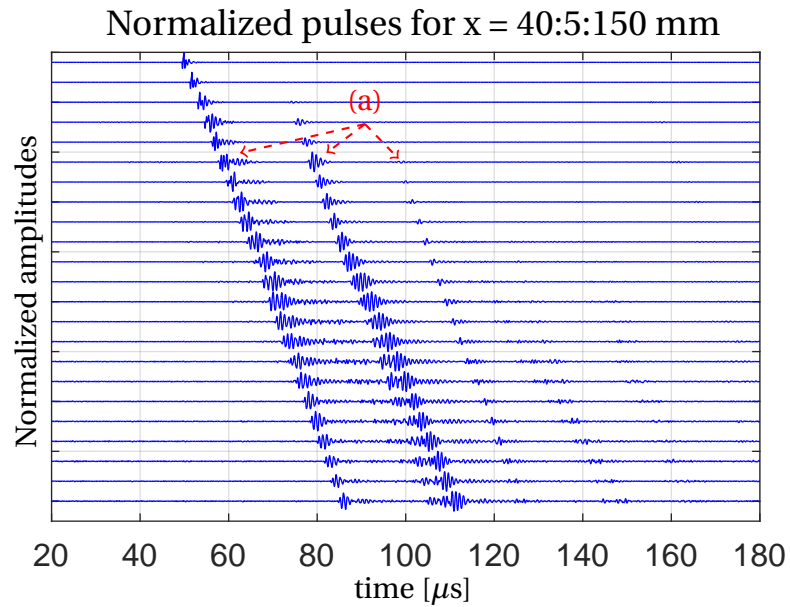


Figure 5.18: Normalized pulses detected by the hydrophone for  $x$ -positions ranging from 40 to 150 mm with 5 mm intervals. The upper line is for  $x = 40$  mm, the second for  $x = 45$  mm etc.

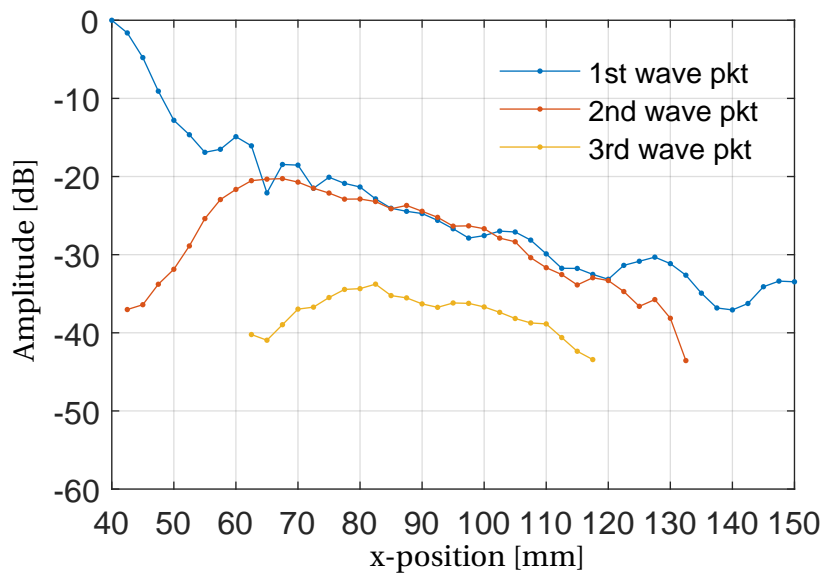


Figure 5.19: The maximum amplitude of the wave packets as a function of  $x$ -position.

### Plate wave spreading

As three distinguishable wave packets can be observed in Figure 5.17, it was of interest to inspect these wave packet's behavior in regard to the spreading in  $y$ -direction. To investigate how the Lamb wave packets propagates in the plate, the maximum amplitude of the wave packet's envelope was found for all the measuring points of the hydrophone. A logarithmic plot displaying the maximum amplitudes of the first Lamb wave packet as a function of  $x$ - and  $y$ -position can be seen in Figure 5.20, where the amplitudes have been normalized against the maximum amplitude at  $x = 40$  mm and  $y = 0$  mm. It can be seen that the amplitudes have their maximum value close to the transducer and that the amplitudes decay fast in  $x$ -direction, as found in Figure 5.19. To investigate the spreading of the wave in  $y$ -direction, the maximum amplitudes for all  $y > 0$  mm were normalized against the corresponding maximum amplitude at  $y = 0$  mm. This was done to compensate for the attenuation in  $x$ -direction and to highlight the plate wave spreading in  $y$ -direction. Figure 5.21 shows this plot together with a line marking the -6 dB level.

To analyze the behavior of the second wave packet, the maximum amplitudes of the second wave packet's envelopes were plotted logarithmic as a function of  $x$ - and  $y$ -position in Figure 5.22. By compensating for the attenuation in  $x$ -direction by normalizing all the maximum values for  $y > 0$  mm against the corresponding values at  $y = 0$  mm, the spreading of the plate wave in  $y$ -direction can be highlighted. This plot is shown in Figure 5.23, where it can be observed that more energy seems to radiate in the positive  $y$ -direction than in the corresponding figures in the two preceding sets of measurements. As the second plate has a tilt of  $3.07^\circ$  relative to the  $xy$ -plane, this is as expected, as the radiated energy from the first wave packet will excite a Lamb wave in the second plate, propagating at an angle relative to the  $x$ -axis.

By conducting the same exercise on the third wave packet, the two plots displayed in Figure 5.24 and Figure 5.25 were plotted. In these two figures the tilting of the second plate in the setup can be clearly observed as the maximum amplitude of the third wave packet is measured at a distance off the  $x$ -axis, at  $y = 10$  mm.

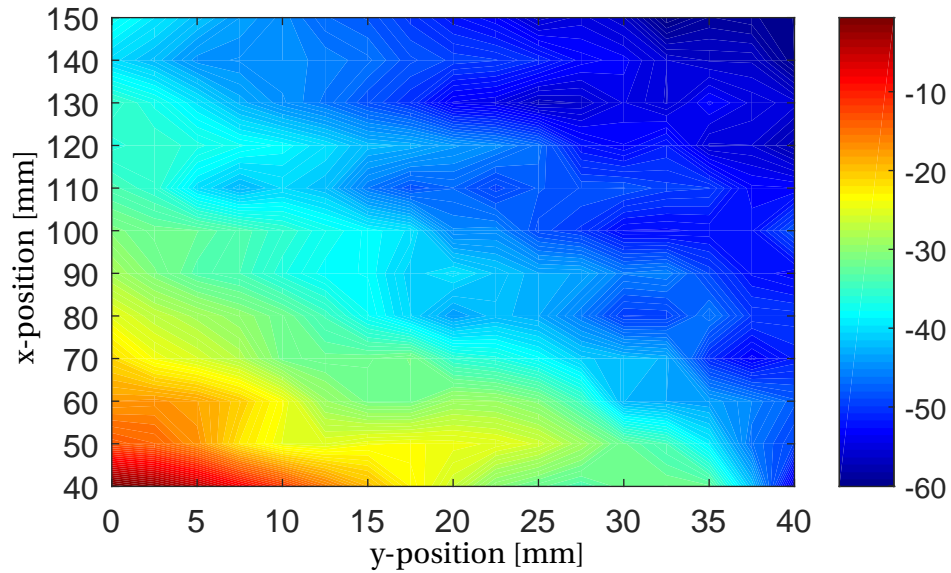


Figure 5.20: The amplitude of the first wave packet plotted logarithmic as a function of  $x$ - and  $y$ -position.

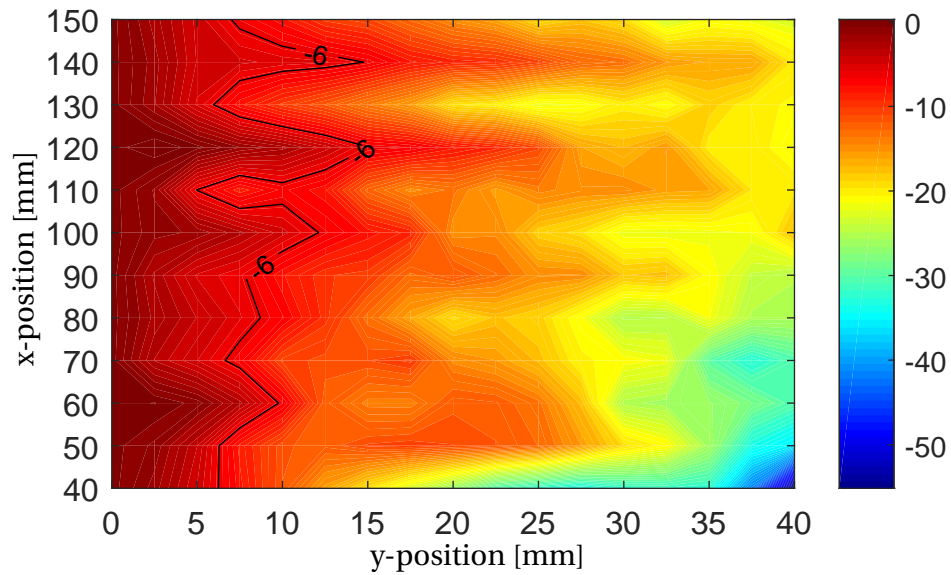


Figure 5.21: The amplitude of the first wave packet normalized against the corresponding value at  $y = 0$  mm. Plotted logarithmic as a function of  $x$ - and  $y$ -position.

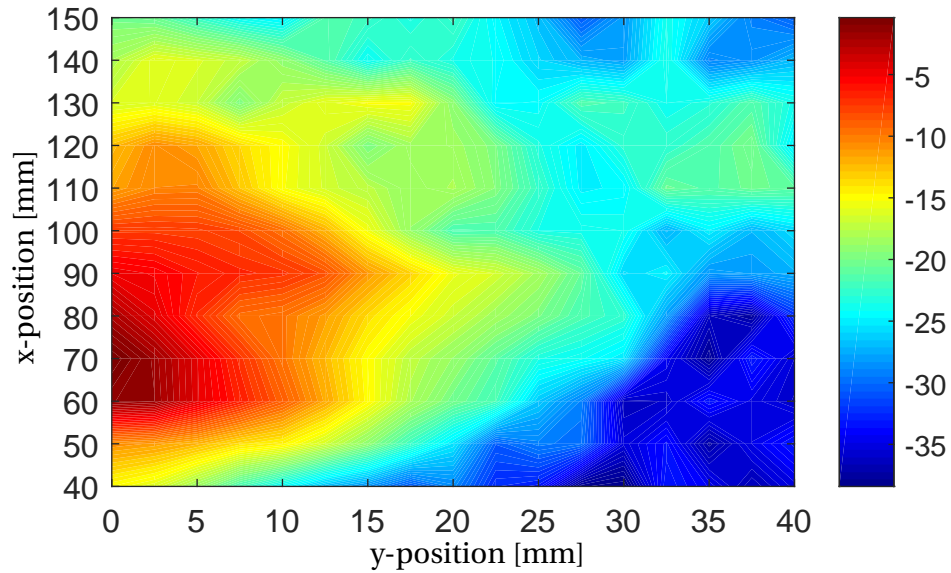


Figure 5.22: The amplitude of the second wave packet plotted logarithmic as a function of  $x$ - and  $y$ -position.

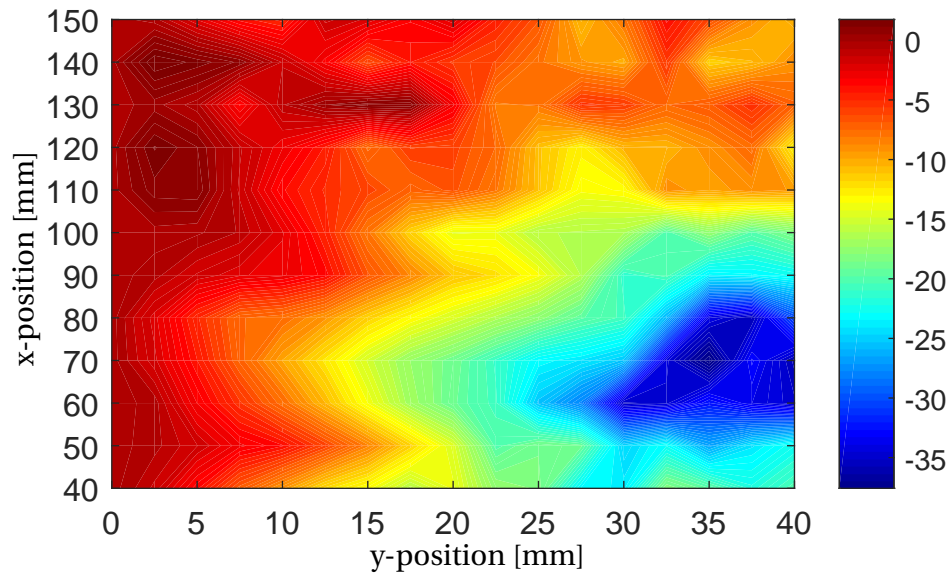


Figure 5.23: The amplitude of the second wave packet normalized against the corresponding value at  $y = 0$  mm. Plotted logarithmic as a function of  $x$ - and  $y$ -position.

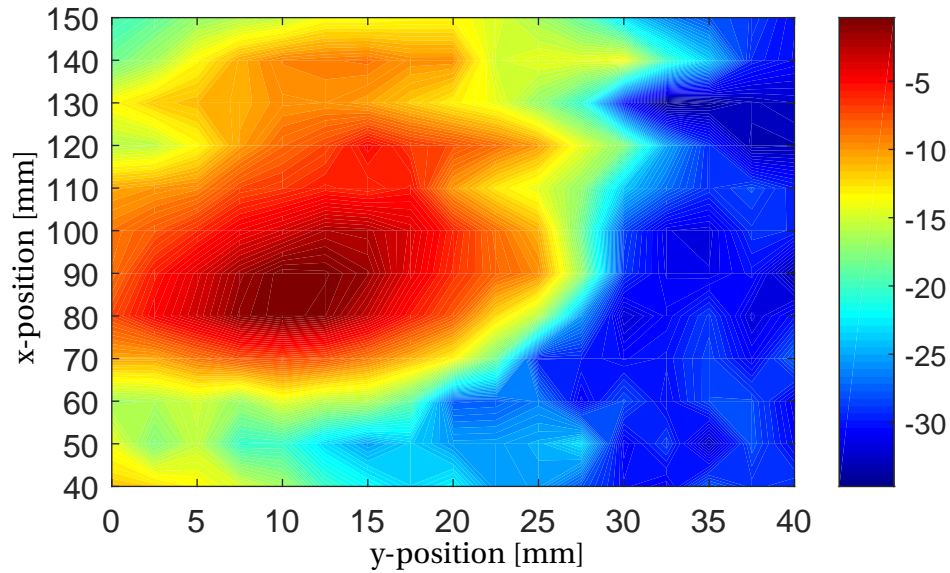


Figure 5.24: The amplitude of the third wave packet plotted logarithmic as a function of  $x$ - and  $y$ -position.

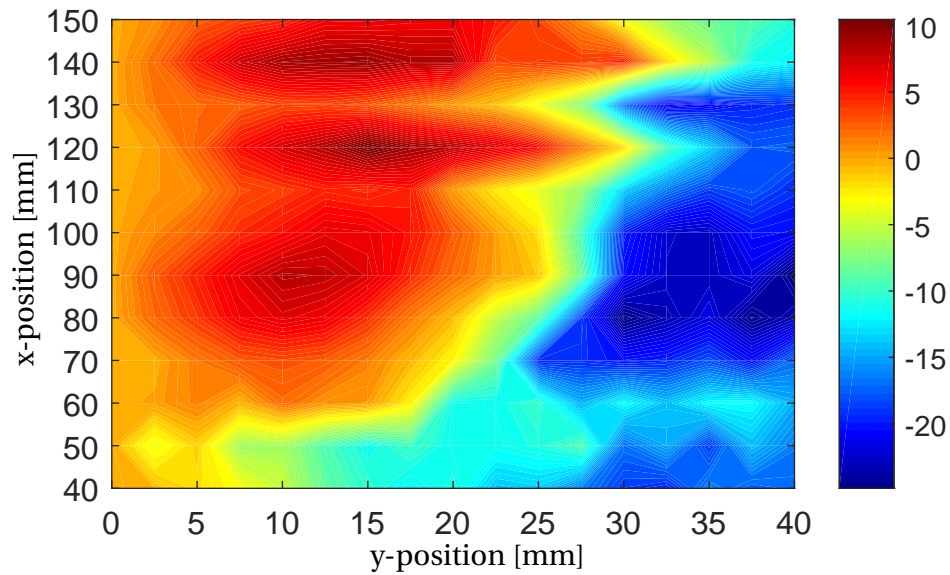


Figure 5.25: The amplitude of the third wave packet normalized against the corresponding value at  $y = 0$  mm. Plotted logarithmic as a function of  $x$ - and  $y$ -position.

## 5.3 COMSOL simulations

To give a deeper understanding of the plate wave propagation in the steel plates a set of simulations were planned. The two main sets of simulations consisting of simulating in a 2D environment with a 3 mm or 4 mm thick plate aligned 13 mm or 12 mm underneath the upper plate, as described in Section 4.4. First a test run where a flat transducer aperture function was used will be briefly presented in the next subsection, before the two main sets of simulations using a sine aperture function for the transducer will be presented.

### 5.3.1 Second plate: 3 mm thick - Flat aperture function

The first simulations were run using a flat aperture function for the transducer as described in equation (4.1). For the 23 measuring points illustrated in Figure 4.8 the pressure in the fluid was logged, and these pulses with normalized amplitudes are plotted as a function of time in Figure 5.26. It can be observed in the area marked (a) that the amplitude of the water-propagating waves are higher than in the experimental data, hence an aperture function adding a spatial limitation to the acceleration of the transducer face were added in the following simulations, with the specific acceleration described in equation (4.2).

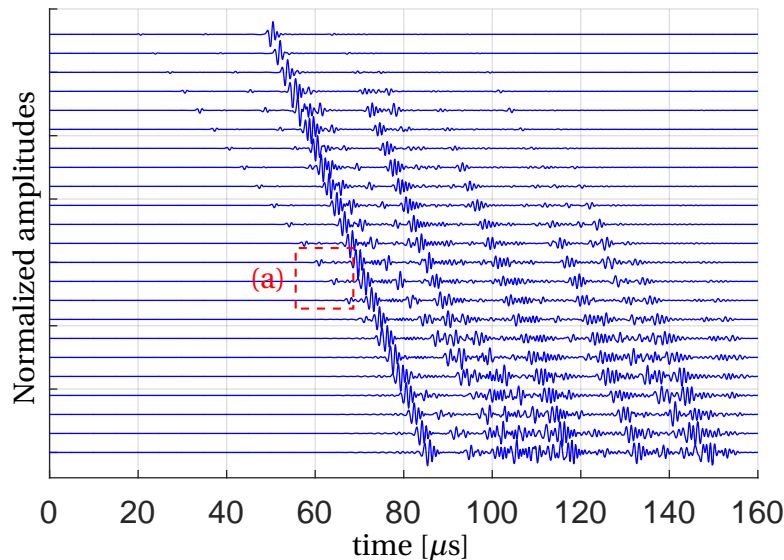


Figure 5.26: Normalized simulated pulses for distances to the transducer ranging from 40 to 150 mm with 5 mm intervals. The upper line is for a distance of 40 mm, the second for 45 mm etc.

### 5.3.2 Second plate: 3 mm thick - Sine aperture function

In the first main simulation the second plate was of thickness 3 mm and the height between the two plates, named  $H_{fl2}$  in Figure 4.8 was 13 mm. The simulation ran for the times,  $t = 0$  to  $160 \mu s$ . In Figure 5.27 four snapshots of the pressure in the three fluid layers and the vertical displacement in the two plates from the COMSOL model can be seen.

By studying the snapshots from the COMSOL model, it can be observed how the first wave packet in the upper plate excites a wave packet in the lower plate. This leads to a train of wave packets leaking energy into the fluid, building up the following wave packets. The area marked (a) highlights an area where it can be observed that the first wave packet consists of two Lamb wave modes, one anti-symmetrical and one symmetrical, propagating at different velocities in the plate. The area marked (b) shows one of the limitations with this model, as the plane wave radiation boundary condition in COMSOL reflects some of the energy for incoming waves at a steep angle.

To compare the simulations with the measurements, the pressure as a function of time was logged at 23 points, at a height of 30 mm above the upper plate and at distances ranging from 40 to 150 mm with 5 mm intervals from the center of the transducer face along the  $x$ -axis. The logged pressure pulses was then filtered using a high-pass zero-phase digital filter to reduce the influence of the water propagating waves of low frequency. The absolute value of the pressure as a function of distance from the transducer and time is plotted logarithmic in Figure 5.28. Marked (a) in this figure the wave being reflected at the upper boundary of the model, which was marked by (b) in Figure 5.27, can be observed as a second top following the pulse radiated from the second wave packet. The pressure logged in the simulations were also plotted with normalized amplitudes as a function of time in Figure 5.29. By doing the same calculations as in the measured data, a group velocity of

$$c_g = 3124.0 \text{ m/s}$$

was calculated for the first wave packet in the simulations. The time difference between the

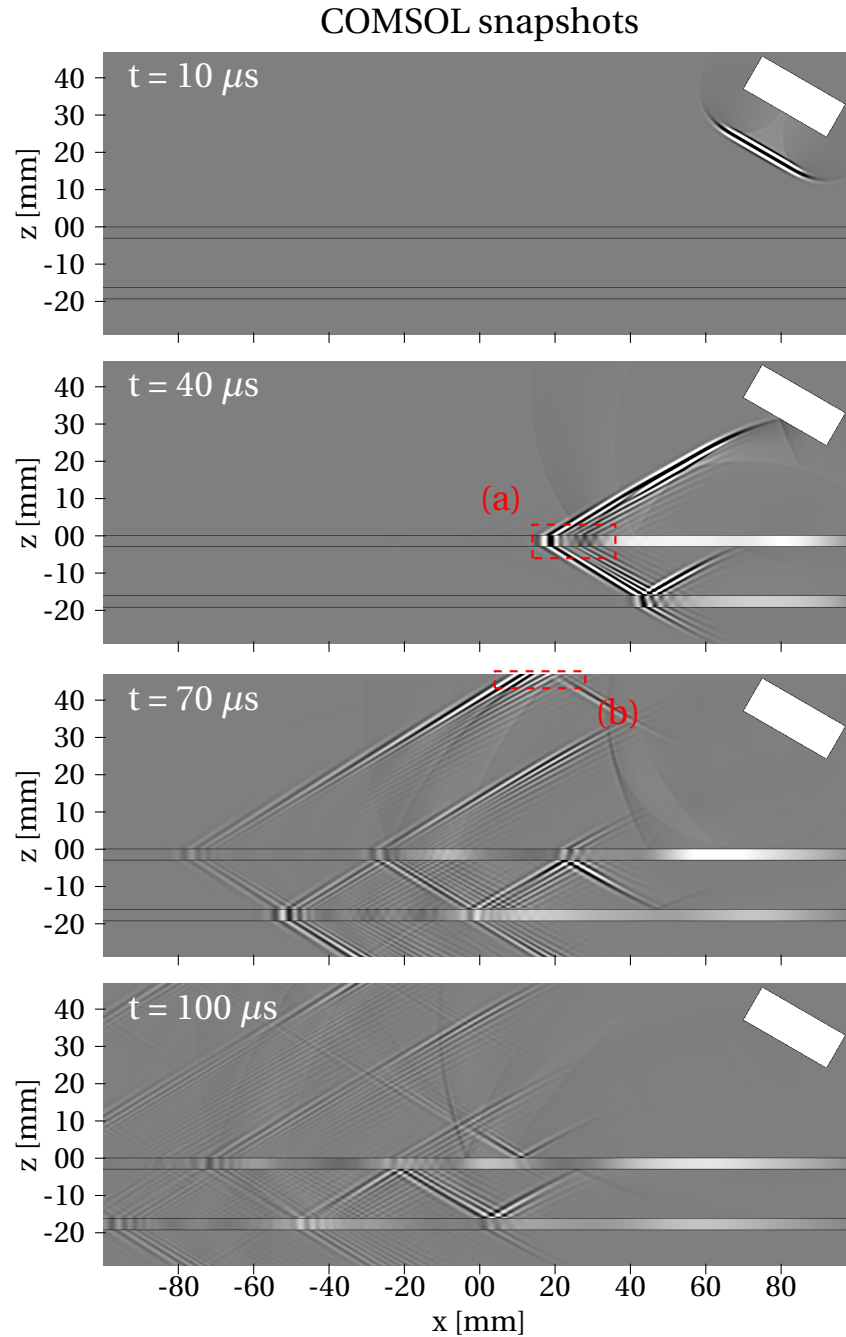


Figure 5.27: Snapshots of pressure  $p$  in the interior and the two annulus and displacement  $u_z$  in plate 1 and 2 at four different times. The setup is with two steel plates of 3 mm thickness and the excited pulse at the transducer face is spatially bounded by a sine function.

maximums of the successive wave packets in the plate,  $\tau$ , was calculated to be

$$\tau_1 = 15.69\mu\text{s}, \quad \tau_2 = 15.989\mu\text{s} \quad \text{and} \quad \tau_3 = 15.46\mu\text{s}.$$



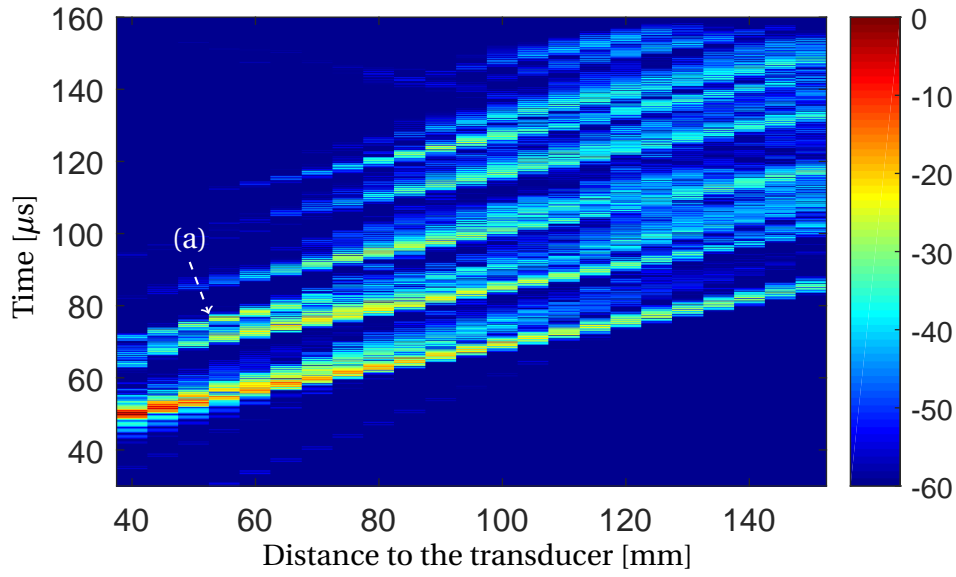


Figure 5.28: The absolute value of the simulated pulse plotted logarithmic as a function of distance from the center of the transducer face along the  $x$ -axis and time.

By comparing this to the expected time difference of

$$\tau = \left( \frac{2H_{fl2}}{c_w} \right) \cos \theta_w = \left( \frac{2 \cdot 13 \cdot 10^{-3}}{1500} \right) \cos(\arcsin(1500/3124)) = 15.21 \mu s,$$

it can be seen that the values from the simulations are generally a bit higher than the expected value.

The maximum amplitudes of the envelopes of the first four wave packets are plotted logarithmic in Figure 5.30. As in the measurements, the amplitude of the first wave packet decreases as the wave propagates in the plate, while the second, third, and fourth wave packet have their maximum amplitude after some propagation in the plate. By doing a linear fit to the amplitude plot for the first wave packet, an attenuation value of 0.218 dB/mm can be found.

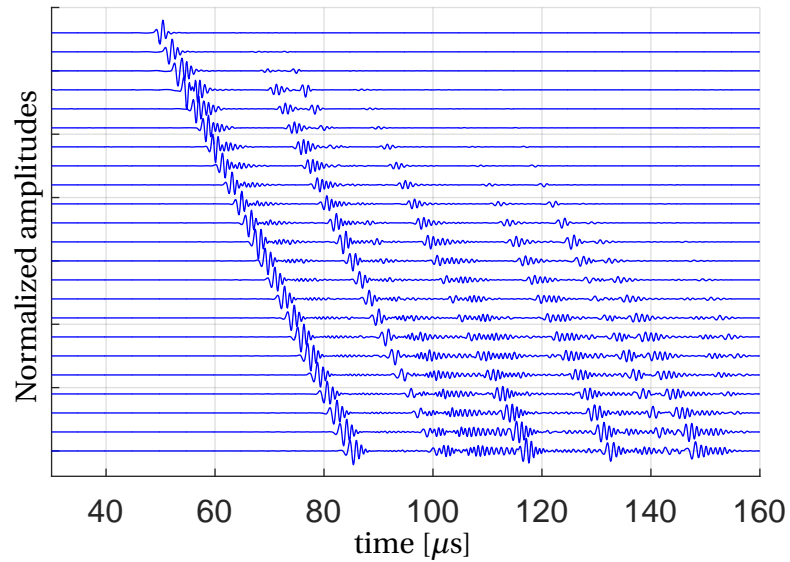


Figure 5.29: Normalized simulated pulses for distances to the transducer ranging from 40 to 150 mm with 5 mm intervals. The upper line is for a distance of 40 mm, the second for 45 mm etc.

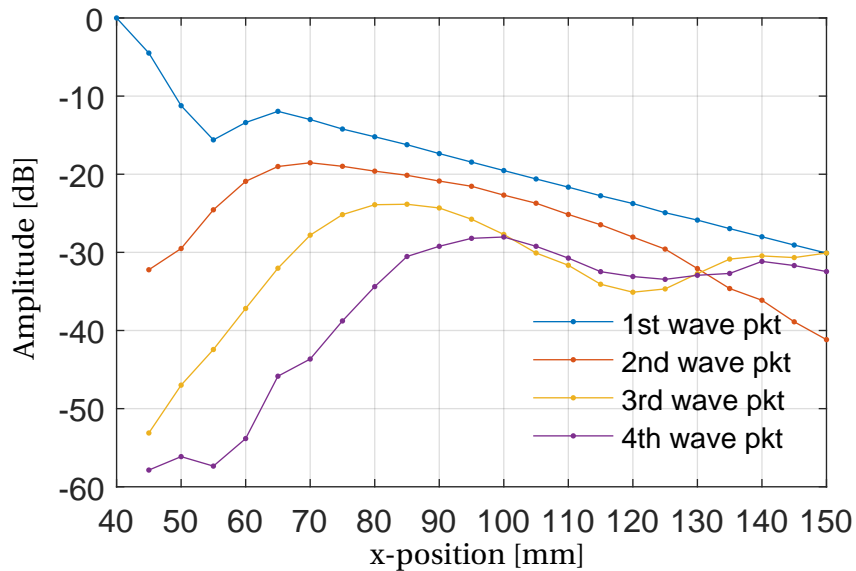


Figure 5.30: The maximum amplitude of the wave packets as a function of distance to the transducer.

### 5.3.3 Second plate: 4 mm thick - Sine aperture function

The second simulation consisted of a setup with a 4 mm thick plate mounted 12 mm underneath the first plate, and as the first simulation, it ran for times,  $t = 0$  to  $160\mu\text{s}$ . Four snapshots of the pressure in the three fluid layers and the vertical displacement in the two plates from the COMSOL model can be seen in Figure 5.31.

By studying the snapshots from the COMSOL model as were done in Subsection 5.3.2, it can be observed that the first wave packet in the upper plate excites a wave packet in the lower plate. This again excites a new wave packet in the upper plate, leading to a train of wave packets in the two plates being excited. The area marked (a) in Figure 5.31 highlights an area where it can be observed that the first wave packet consists of one symmetric and one anti-symmetric Lamb wave mode, propagating at different velocities in the plate. As in the model with the 3 mm thick plate, the area marked (b) shows that some of the energy of the wave is reflected back at the boundary of the model.

To compare this simulation with the experimental work, the absolute value of the pressure logged at 23 points with a distance ranging from 40 mm to 150 mm from the center of the transducer face, at a height of 30 mm above the plate were plotted logarithmic as a function of distance to the transducer and time in Figure 5.32. The pulses has gone through a high-pass, zero-phase filter to reduce the influence from the low frequency water-propagating waves. Marked (a), the wave being reflected at the upper boundary of the simulation model can be observed in the figure. The pressure logged in the simulations are also shown in Figure 5.33 where the pulses are plotted with normalized amplitudes as a function of time.

The calculation of the group speed in the second simulation setup lead to the same group velocity as in the first simulation,  $c_g = 3124$  m/s, while the time differences between the maximums of the successive wave packets in the plate,  $\tau$ , was calculated to

$$\tau_1 = 14.852\mu\text{s}, \quad \tau_2 = 14.924\mu\text{s} \quad \text{and} \quad \tau_3 = 14.933\mu\text{s}.$$

By comparing this to the expected time difference

$$\tau = \left( \frac{2H_{\text{fl2}}}{c_w} \right) \cos \theta_w = \left( \frac{2 \cdot 12 \cdot 10^{-3}}{1500} \right) \cos(\arcsin(1500/3124)) = 14.04\mu\text{s},$$

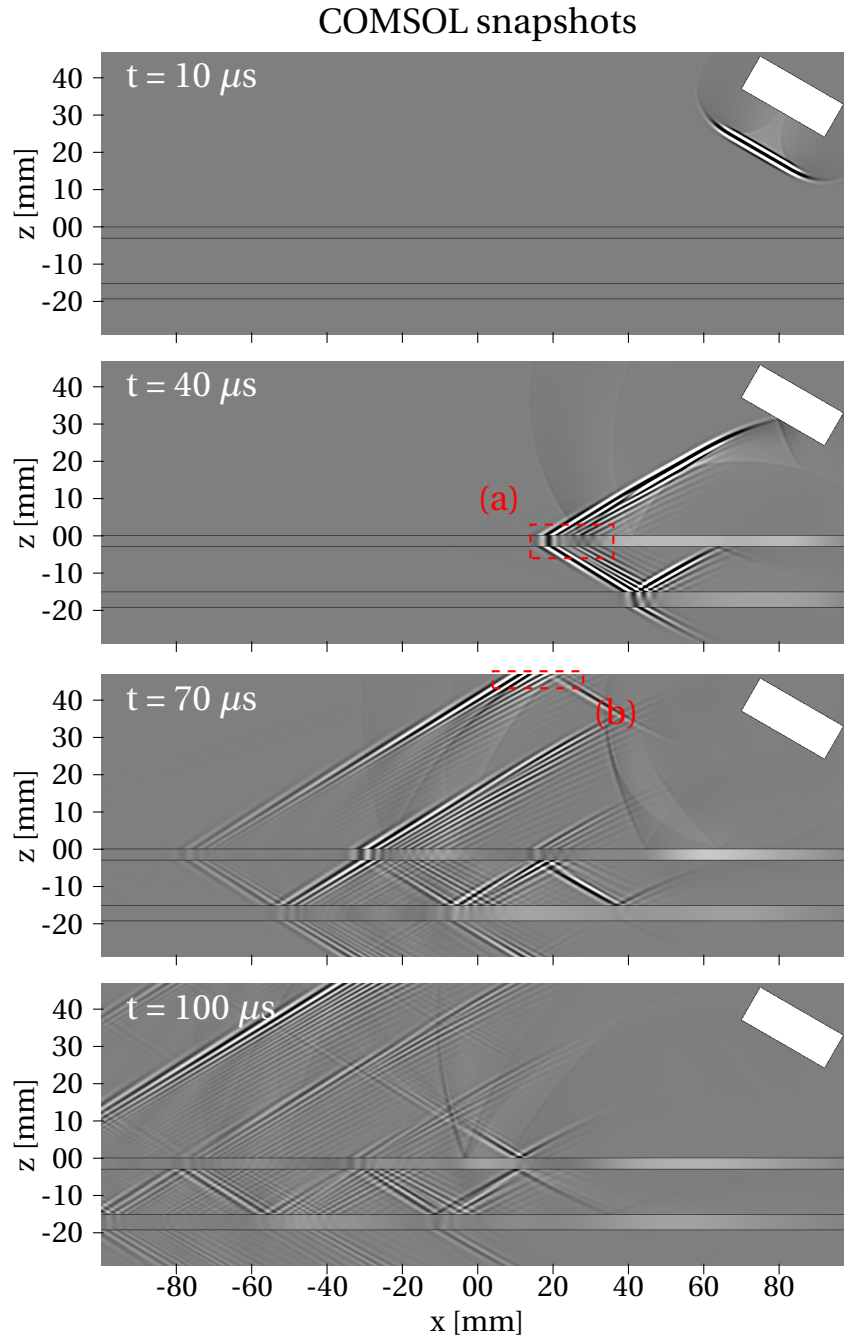


Figure 5.31: Snapshots of pressure  $p$  in the interior and the two annulus and displacement  $u_z$  in plate 1 and 2 at four different times. The setup is with one plate of 3 mm thickness and one of 4 mm thickness. The excited pulse at the transducer face is spatially bounded by a sine function.

it can be observed that they are generally a bit higher than the expected value, as was found for the simulations in Subsection 5.3.2.

The maximum amplitude of the envelopes of the first four wave packets are plotted logarithm-

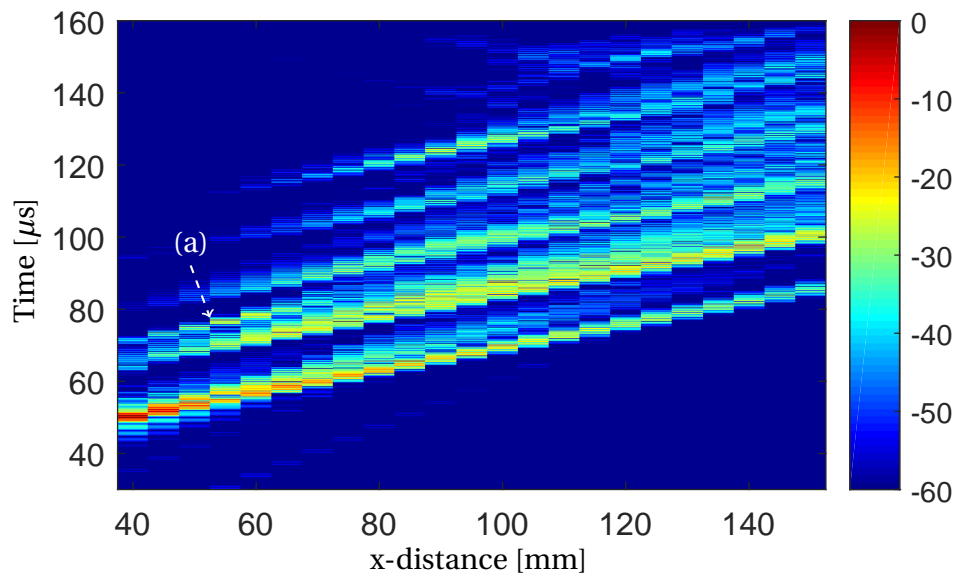


Figure 5.32: The absolute value of the simulated pulse plotted logarithmic as a function of distance from the center of the transducer face along the  $x$ -axis and time.

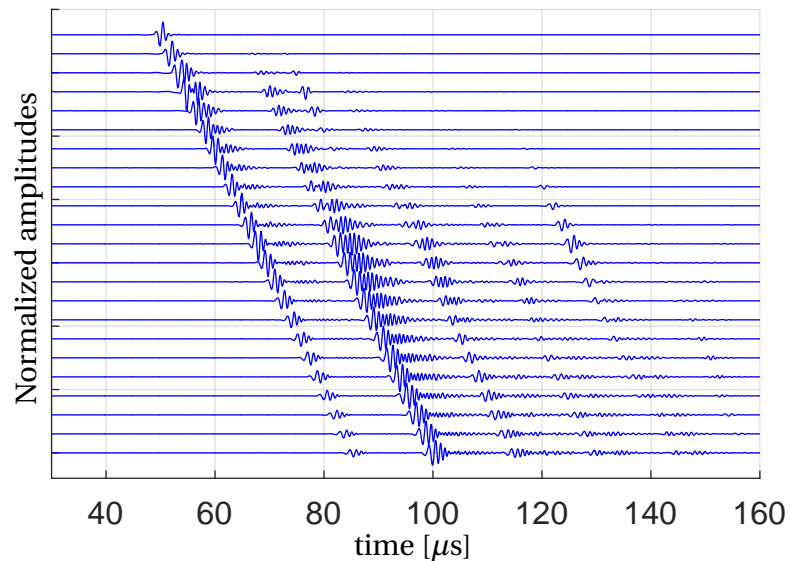


Figure 5.33: Normalized simulated pulses for distances to the transducer ranging from 40 to 150 mm with 5 mm intervals. The upper line is for a distance of 40 mm, the second for 45 mm etc.

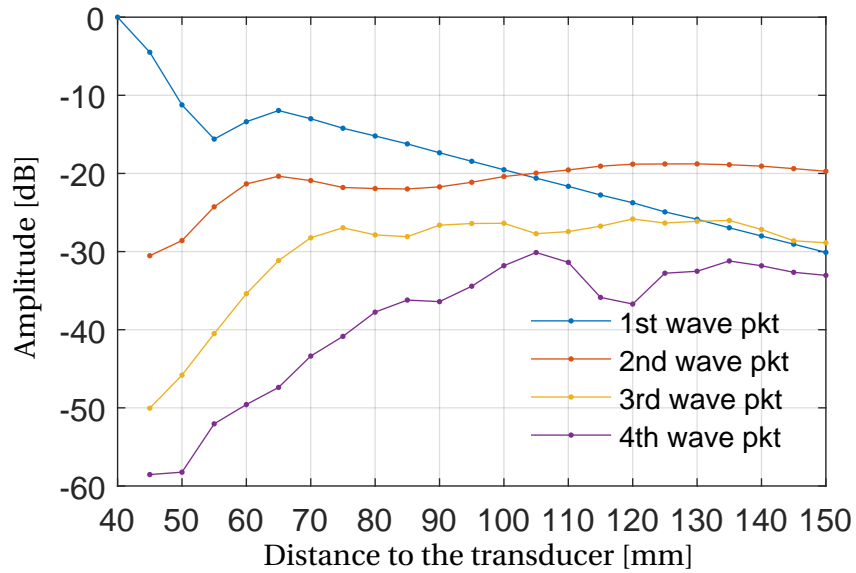


Figure 5.34: The maximum amplitude of the wave packets as a function of distance to the transducer.

mic in Figure 5.34, where the amplitude of the first wave packet shows the exact same behavior as for the first set of simulations, and by doing a linear fit the same attenuation value of 0.218 dB/mm is found. In this simulation it can be observed that the amplitudes of the second, third and fourth wave packet in the upper plate increase to a higher level than in the previous simulation.

# 6

## Discussion

The work on trying to match the experimental measurements with the 2D simulations in COM-SOL were to a certain extent successful. During the analysis of the experimental measured data, the impact of noise and uncertainties in the measurements proved to play a bigger part than expected. The results of the experiments and the simulation work will be discussed more thoroughly in this chapter.

In both the measurements and the simulations conducted, the excitation of both a flexural and an extensional Lamb wave mode can be observed. As it can be seen that the amplitude of the energy radiated from the flexural mode into the fluid is much higher than the energy from the extensional mode, it is believed that it is the flexural mode that gives origin to the wave packets which were analyzed in Chapter 5. For the measuring points located closest to the transducer, it can be observed that the water-propagating wave being reflected at steel plate interfere with the wave front radiated from the first wave packet in the plate. This is due to the time of arrival of the two waves being almost identical, and that the water-propagating wave being reflected at the plate has a relatively high amplitude for the measuring points close to the transducer, where the decrease due to the directivity of the transducer is smaller than for larger distances.

By analyzing the amplitudes of the first wave packet as a function of distance from the transducer for the three sets of measurements and for the simulations, plotted in Figure 6.1, it can be observed that the amplitude plot for the simulations has a small local minimum at a  $x$ -distance of 55 mm from the center of the transducer face. After  $x = 55$  mm it increases in amplitude to the value logged for  $x = 65$  mm, before it starts to decrease steadily. The same type of behavior can be observed in the experimental measured data, and this effect may originate from the in-

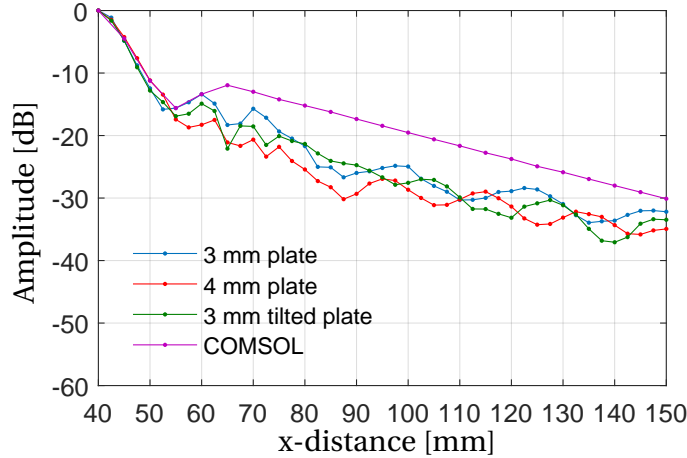


Figure 6.1: The maximum amplitude of the first wave packets as a function of  $x$ -distance from the center of the transducer face.

interference with the water-propagating waves. By doing a linear fit on the amplitudes measured for  $x$ -distances from 65 mm and further away from the transducer, the attenuation values of

$$\alpha_{3\text{mm}} = 0.185\text{dB/mm}, \quad \alpha_{4\text{mm}} = 0.160\text{dB/mm},$$

$$\alpha_{3\text{mm tilt}} = 0.201\text{dB/mm} \text{ and } \alpha_{\text{COMSOL}} = 0.214\text{dB/mm}$$

can be found. The attenuation value from both the measurements with the 3 mm plate inside the BeCaLoS and the value from the COMSOL simulations seems to fit well with the expected value of approximately 0.2 dB/mm for the lowest order anti-symmetrical Lamb wave mode in a steel plate in water, found in the work conducted by Wilcox *et al.* [36].

The three group velocities for the first wave packet found in the measurements were  $c_g = 3083.5$  m/s, 2950.1 m/s, and 3099.6 m/s for the setup with the 3 mm plate, the 4 mm plate, and the 3 mm tilted plate inside the BeCaLoS respectively. From the simulations a group velocity of  $c_g = 3124$  m/s was found. Comparing these values with the work done by Zeroug *et al.* [37], a group velocity of about 3140 m/s for the flexural Lamb wave mode in a 3 mm thick steel plate and with a frequency of 1 MHz would be expected. This value for the group velocity is read of manually from a figure, hence it is not very accurate, but it seems to fit well with the simulated and measured velocities for the two setups with the 3 mm plate inside the BeCaLoS. This confirms that it is the lowest order anti-symmetrical Lamb mode that mainly are observed in the



experiments and the simulations.

As the both the upper plate and the fluid in the setup are the same in all the measurements, the same behavior of the first wave packet would be expected. In Figure 5.5, Figure 5.14 and Figure 5.21 it can be seen that the propagation of the first wave packet in the three plots are mainly in the  $x$ -direction, with little spreading in  $y$ -direction. The interference from the wave propagating directly from the transducer to the hydrophone can be observed at the same measuring points in the setup with the 3 mm and the 4 mm thick plate mounted without a tilt inside the BeCaLoS. For the setup with the 3 mm tilted plate, the interference appear at  $x = 120$  mm and  $x = 140$  mm, and with stronger amplitudes relative to the amplitudes measured at  $y = 0$  mm. In Talberg, 2016 [30], the plate wave spreading in a setup with air as annulus material were analyzed, and as the SNR were higher for this set of measurements, the wave propagation mainly in  $x$ -direction could be more clearly observed in the experimental results than it the sets of measurements presented in this thesis.

From the phase and group velocity plot in Zeroug *et al.* [37] it can be seen that by changing the steel plate thickness from 3 mm to 4 mm, the phase and group velocity of the flexural mode does not change drastically. The excitation of multiple Lamb wave packets should therefore be clearly present in the experiments with a 4 mm thick plate mounted inside the BeCaLoS, as it is in the simulation with the second plate of 4 mm thickness. In Figure 5.10 only two wave packets can be observed. The reason for this may be disturbances due to bubbles at the plate surface. When leaving the BeCaLoS still for 24 hours after filling it with water, lots of small bubbles were detected at the upper steel plate. These were removed manually by scraping the plate before the measurements were conducted, but due to the interior of the BeCaLoS being inaccessible after mounting the upper plate, a method to ensure the absence of these potential bubbles inside the setup should be considered in future work. If a thin bubble layer was present at the lower side of the upper plate or at the top surface of the second plate during the measurements, the radiation of energy from the wave packets in the plate into the fluid could be influenced, and the presence of bubbles in the setup may be the reason for only detecting two Lamb wave packets and also a lower attenuation value in the experimental data for the setup with the 4 mm thick plate mounted inside the BeCaLoS.

A strange find from the measured data is the time differences between the successive wave

packets, as the measured time differences are smaller than the time the wave use to propagate between the two plates in the fluid layer. From the simulations, the time difference measured were a bit longer than the expected value, which seems more logical. The uncertainty when measuring the distance between the plate should be considered, but it is very unlikely that this can be the sole source of such a significant deviation.

By analyzing the behavior of the second and third wave packet in the experiment conducted with the 3 mm plate mounted with a tilt inside the BeCaLoS, it can clearly be seen in Figure 5.24 and Figure 5.25 that this method of measuring can detect eventual casing eccentricity. By performing a set of measurements with a finer grid of measuring point and analyzing the data further, the exact tilt of the second plate can possibly be detected.

As the waves propagating in water propagates at a velocity much lower than the velocity of the plate waves, the distance between the transmitter and receiver in the pitch-catch method should be placed further apart from each other to prevent the water-propagating waves interfering with the waves from the plate waves. In Viggen *et al.* [32] a transmitter-receiver distance of 25 cm and 35 cm were used, while in this thesis the distances used were from 4 cm to 15 cm in  $x$ -direction. While measuring for larger  $x$ -values would make it easier to separate the waves of interest from the water-propagating waves, it would also decrease the signal-to-noise ratio, making the signal harder to detect. The SNR was the reason the measurements were conducted at the distances used in this thesis.

# 7

## Conclusions and Future Work

### Conclusions

The work presented in this thesis consisted of the creation of a simulation model and the execution of a set of ultrasonic experiments, both intended to give a deeper understanding of broadband wave propagation in plates. A 2 dimensional FEM model was created in COMSOL Multiphysics to model the situation of an ultrasonic pitch-catch measurement in a double-casing geometry, with one transmitter emitting a broadband ultrasonic pulse and an array of points for measuring the pressure at different distances to the transducer. Through the simulations it could be observed that a train of Lamb wave packets were excited on both of the steel plates in the model, and a set of experimental measurements were conducted to give experimental verification of this observation. In Section 5.2 three sets of experiments were presented, with the excitation of the train of Lamb wave packets being clearly observed in two of the measurement sets. By studying the simulations it can be observed that the transducer excites a symmetrical and an anti-symmetrical Lamb wave mode in the plate, with the anti-symmetrical mode radiating most energy into the fluid and propagating at the highest velocity. The group velocities found in the experiments confirm that it is the lowest order anti-symmetrical mode which is the origin of the wave front being radiated from the plate wave which is detected by the hydrophone.

By tilting the lower plate in the BeCaLoS, the situation of casing eccentricity could be replicated to some extent. When detecting the second and third wave packet propagating in the upper plate, it can be observed that the tilting of the lower plate leads to excitation of wave packets having their maximum amplitude at a distance off the original axis of propagation.

The influence of the interference of the signals by the water-propagating waves proved to

be more significant than expected when planning the experiments, and as mentioned in the recommendations for future work, the use of a different receiver should be considered. The hydrophone was chosen due to its low directivity which was an advantage when placing the hydrophone relative to the transducer, not having to adjust the tilt for every measuring point, but it proves to be a disadvantage in regards to the disturbance from the water-propagating waves. By increasing the transmitter-receiver distance, the time of arrival for the water-propagating waves can be made significantly different than for the waves being radiated from the wave packets in the plate. As the wave packet is quite strongly attenuated in the plate, different transmitters and receivers should be considered to increase the signal-to-noise ratio if measuring at larger distances.

## **Recommendations for future work**

There is a lot of work that can be done with the BeCaLoS in regards to the evaluation of broadband wave propagation in steel plates. To continue to develop a good simulation model would also aid future work, as the simulations help predicting the behavior of the experiments. Doing simulations in 3 dimensions would be preferable, e.g. to investigate the impact of casing eccentricity on the plate waves, but the computational power needed for these simulations is huge. By filling the volume underneath the second plate with different material and by using different fluids in the setup, interesting well-like configurations can be replicated.

In regards to the setup, investing in a robot doing the placing of the hydrophone and transducer automatically should be considered. The measuring process where the hydrophone is placed at different positions relative to the transducer is time demanding and also introduces a possibility of a measuring error due to the manual position measurements. The placing of the second steel plate inside the BeCaLoS was done using wooden support legs, and investing in a more solid and easier adjustable holder should also be considered if further work shall be conducted on the setup with two plates. The use of a different receiver should also be considered, as the low directivity of the hydrophone makes it more receptive of the water-propagating waves, and to overcome the problems with the signal-to-noise ratio becoming too small for larger distances from the transmitter.

# Bibliography

- [1] Alleyne, D. N. and Cawley, P. (1992). The interaction of lamb waves with defects. *Ultrasonics, Ferroelectrics, and Frequency Control, IEEE Transactions on*, 39(3):381–397.
- [2] Allouche, M., Guillot, D., Hayman, A. J., Butsch, R. J., and Morris, C. W. (2005a). *Well cementing*, chapter 15. Schlumberger.
- [3] Allouche, M., Guillot, D., Hayman, A. J., Butsch, R. J., and Morris, C. W. (2005b). *Well cementing*, chapter 5. Schlumberger.
- [4] Bellabarba, M., Bulte-Loyer, H., Froelich, B., Le Roy-Delage, S., van Kuijk, R., Zeroug, S., Guillot, D., Moroni, N., Pastor, S., and Zanchi, A. (2008). Ensuring zonal isolation beyond the life of the well. *Oilfield Review*, 20(1):18–31.
- [5] Calvert, D. (2005). *Well cementing*, chapter preface. Schlumberger.
- [6] Cavanagh, P. H., Johnson, C. R., Roy-Delage, L., DeBruijn, G. G., Cooper, I., Guillot, D. J., Bulte, H., Dargaud, B., et al. (2007). Self-healing cement-novel technology to achieve leak-free wells. In *SPE/IADC Drilling Conference*. Society of Petroleum Engineers.
- [7] Frigaard, I., Pelipenko, S., et al. (2003). Effective and ineffective strategies for mud removal and cement slurry design. In *SPE Latin American and Caribbean Petroleum Engineering Conference*. Society of Petroleum Engineers.
- [8] Froelich, B., Dumont, A., Pittman, D., Seeman, B., et al. (1982). Cement evaluation tool: A new approach to cement evaluation. *Journal of Petroleum Technology*, 34(08):1–835.
- [9] Harb, M. and Yuan, F.-G. (2016). Non-contact ultrasonic technique for lamb wave characterization in composite plates. *Ultrasonics*, 64:162–169.

- 
- [10] Hayden, R., Russell, C., Vereide, A., Babasick, P., Shaposhnikov, P., May, D., et al. (2011). Case studies in evaluation of cement with wireline logs in a deep water environment. In *SPWLA 52nd Annual Logging Symposium*. Society of Petrophysicists and Well-Log Analysts.
- [11] Hoel, K. (2014). Ultrasonic evaluation of well integrity.
- [12] Hora, P. and Červená, O. (2012). Determination of lamb wave dispersion curves by means of fourier transform.
- [13] Hovem, J. M. (2012a). *Marine Acoustics: The Physics of Sound in Underwater Environments*, chapter 15 - Elastic waves in solids. Peninsula publishing.
- [14] Hovem, J. M. (2012b). *Marine Acoustics: The Physics of Sound in Underwater Environments*, chapter 5 - Reflection and transmission in multilayered media. Peninsula publishing.
- [15] Khalifeh, M., Hodne, H., Saasen, A., Vralstad, T., et al. (2013). Techniques and materials for north sea plug and abandonment operations. In *Offshore Technology Conference*. Offshore Technology Conference.
- [16] Kristiansen, U. R. and Viggen, E. (2010). *Computational methods in acoustics*, volume 69, chapter 3 - The finite element method. Department of electronics and telecommunications, NTNU.
- [17] Lamb, H. (1917). On waves in an elastic plate. *Proceedings of the Royal Society of London. Series A, Containing papers of a mathematical and physical character*, pages 114–128.
- [18] Liversidge, D., Taoutaou, S., Agarwal, S., et al. (2006). Permanent plug and abandonment solution for the north sea. In *SPE Asia Pacific Oil & Gas Conference and Exhibition*. Society of Petroleum Engineers.
- [19] Løvstad, A. (2012). Detection of localised corrosion in pipes using guided waves.
- [20] Morris, C. W., Sabbagh, L., Wydrinski, R., Hupp, J. L., van Kuijk, R., Froelich, B., et al. (2007). Application of enhanced ultrasonic measurements for cement and casing evaluation. In *SPE/IADC Drilling Conference*. Society of Petroleum Engineers.

- 
- [21] Norwegian Petroleum Directorate. Norwegian Petroleum Directorate - fact pages. <http://factpages.npd.no/factpages/default.aspx?culture=en&nav1=wellbore&nav2=Statistics|EntryYear>. Accessed: 13.03.2016.
- [22] Norwegian Petroleum Directorate. Norwegian petroleum history. <http://www.norskpetroleum.no/en/framework/norways-petroleum-history/>. Accessed: 05.05.2016.
- [23] Olympus-IMS. Olympus Panametrics C302 - Transducer. <http://www.olympus-ims.com/en/ultrasonic-transducers/immersion/>. Accessed: 20.11.2015.
- [24] Olympus-IMS. Olympus Panametrics-NDT 5900PR - Pulse/Receiver. <http://www.olympus-ims.com/en/5800pr/>. Accessed: 20.11.2015.
- [25] Onda Corp. Onda HNR data sheet. Revised: October 15, 2015.
- [26] Roy-Delage, L., Baumgarte, C., Thiercelin, M., Vidick, B., et al. (2000). New cement systems for durable zonal isolation. In *IADC/SPE Drilling Conference*. Society of Petroleum Engineers.
- [27] Schlumberger (2011). Isolation scanner - Advanced evaluation of wellbore integrity - product brochure.
- [28] Statoil Innovate. Statoil Innovate -challenges - plug & abandonment. <http://innovate.statoil.com/challenges/Pages/PlugAndAbandonment.aspx>. Accessed: 06.06.2016.
- [29] Talberg, A. (2015). Experimental evaluation of broadband wave propagation in plates. *Unpublished*.
- [30] Talberg, A. S. and Johansen, T. F. (2016). Acoustic measurements above a plate carrying lamb waves. *arXiv preprint arXiv:1604.02254*.
- [31] van Kuijk, R., Zeroug, S., Froelich, B., Allouche, M., Bose, S., Miller, D., Le Calvez, J.-L., Schoepf, V., Pagnin, A., et al. (2005). A novel ultrasonic cased-hole imager for enhanced cement evaluation. In *International Petroleum Technology Conference*. International Petroleum Technology Conference.

- 
- [32] Viggen, E. M., Johansen, T. E, and Merciu, I.-A. (2016). Simulation and modeling of ultrasonic pitch-catch through-tubing logging. *Geophysics*, 81(4):D383–D393.
- [33] Vigran, T. E. *Building acoustics*, chapter 3 - Waves in fluid and solid media.
- [34] Viktorov, I. A. (1967a). *Rayleigh and Lamb waves: physical theory and applications*, chapter II. Plenum Press.
- [35] Viktorov, I. A. (1967b). *Rayleigh and Lamb waves: physical theory and applications*, chapter I. Plenum Press.
- [36] Wilcox, P, Lowe, M., and Cawley, P. (2001). Mode and transducer selection for long range lamb wave inspection. *Journal of intelligent material systems and structures*, 12(8):553–565.
- [37] Zeroug, S. and Froelich, B. (2003). Ultrasonic leaky-lamb wave imaging through a highly contrasting layer. In *2003 IEEE Symposium on Ultrasonics*, volume 1, pages 794–798. IEEE.



# A

## Tables

The specific configurations for each set of measurements is listed in the tables in this appendix.

Table A.1: The configuration of the experimental setup with a 3 mm thick plate mounted inside the BeCaLoS.

Variable	Value
Transmitter - Receiver distance ( $x$ -pos.)	40 - 150 mm
Side-/ $y$ -position	0 - 40 mm
Second plate thickness	3 mm
Distance between the plates	(12.87, 13.40, 13.86, 12.66) mm <sup>1</sup>
Transducer Tilt	30°
Transducer Height	30 mm
Hydrophone Tilt	33°
Hydrophone Height	30 mm
BeCaLoS Tilt	5.8°
Pulse/Receiver Settings	
Energy	32 $\mu$ J
Gain	40.0 dB
Attenuators	0.0 dB

<sup>1</sup>Measured at the four points marked 1, 2, 3, and 4 in Figure 4.1

Table A.2: The configuration of the experimental setup with a 4 mm thick plate mounted inside the BeCaLoS.

Variable	Value
Transmitter - Receiver distance ( $x$ -pos.)	40 - 150 mm
Side- / $y$ -position	0 - 40 mm
Second plate thickness	4 mm
Distance between the plates	(12.15, 13.18, 10.97, 11.92) mm <sup>1</sup>
Transducer Tilt	30°
Transducer Height	30 mm
Hydrophone Tilt	33°
Hydrophone Height	30 mm
BeCaLoS Tilt	4.6°
Pulse/Receiver Settings	
Energy	32 $\mu$ J
Gain	40.0 dB
Attenuators	0.0 dB

Table A.3: The configuration of the experimental setup with a 3 mm thick plate mounted with a tilt inside the BeCaLoS.

Variable	Value
Transmitter - Receiver distance ( $x$ -pos.)	40 - 150 mm
Side- / $y$ -position	0 - 40 mm
Second plate thickness	3 mm
Distance between the plates	(8.53, 22.06, 35.32, 21.62) mm <sup>1</sup>
Transducer $y$ -position	192 mm <sup>2</sup>
Transducer Tilt	30°
Transducer Height	30 mm
Hydrophone Tilt	33°
Hydrophone Height	30 mm
BeCaLoS Tilt	4.6°
Pulse/Receiver Settings	
Energy	32 $\mu$ J
Gain	40.0 dB
Attenuators	0.0 dB

<sup>1</sup>Measured at the four points marked 1, 2, 3, and 4 in Figure 4.1

<sup>2</sup>Measured in  $y$ -direction from edge marked "1" in Figure 4.1

# B

## **SSPA 2016 Article**

During the period from January 31st to February 3rd 2016, the author participated at the 39th Scandinavian Symposium on Physical Acoustics in Geilo, Norway. The author held one of 31 talks and contributed to the symposium proceedings with the paper added in this appendix.

This page is intentionally left blank.

# Acoustic measurements above a plate carrying Lamb waves

Andreas Sørbrøden Talberg<sup>1</sup>, Tonni Franke Johansen<sup>1,2</sup>

<sup>1</sup> Norwegian University of Science and Technology, NTNU

<sup>2</sup> SINTEF ICT

Contact email: andreasstalberg@gmail.com

## Abstract

This article presents a set of acoustic measurements conducted on the Statoil funded Behind Casing Logging Set-Up, designed by SINTEF Petroleum Research to resemble an oil well casing. A set of simple simulations using COMSOL Multiphysics were also conducted and the results compared with the measurements. The experiments consists of measuring the pressure wave radiated of a set of Lamb waves propagating in a 3 mm thick steel plate, using the so called pitch-catch method. The Lamb waves were excited by a broadband piezoelectric immersion transducer with center frequency of 1 MHz. Through measurements and analysis the group velocity of the fastest mode in the plate was found to be 3138.5 m/s. Measuring the wave radiated into the water in a grid consisting of 8x33 measuring points, the spreading of the plate wave normal to the direction of propagation was investigated. Comparing the point where the amplitude had decreased 50 % relative to the amplitude measured at the axis pointing straight forward from the transducer shows that the wave spread out 3.2 mm after propagating 140 mm in the plate.

## 1 Introduction

According to the Norwegian Petroleum Directorate there have been drilled more than 1500 exploration wells and more than 4200 development wells on the Norwegian Continental Shelf since the discovery of oil in 1966 [1]. Due to the severity of uncontrolled hydrocarbon migration from oil or gas bearing reservoirs to the surroundings, both during production as well as when the well has been plugged for abandonment, it is crucial to cement the well properly. After a cement job has been completed, a proper inspection has to be conducted to evaluate the cement sheath. The operation of placing a permanent plug in a well that has reached the end of its lifetime on offshore exploration wells in Norway, can contribute with 25% of the total drilling costs [2]. Due to the extra cost for the responsible company and the environmental consequences of an improperly executed cement job, the field of cement job evaluation is of great interest.

### Well Cementing

When placing a cement sheath, different criteria have to be fulfilled. The main objective of primary cementing, the stage where cement is placed in the annulus between the casing and the borehole wall, is to create zonal isolation. This is achieved by creating a hydraulic seal between both the cement and borehole wall, as well as between the casing and the

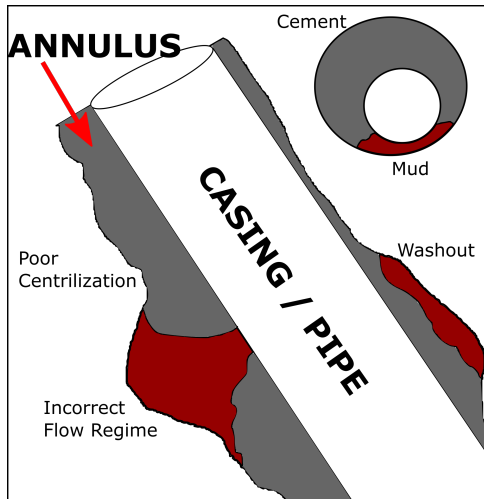


Figure 1: Examples of cement slurry displacement problems in the annulus.

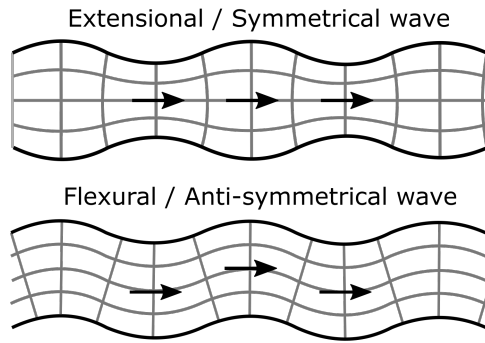


Figure 2: Illustration of the particle displacement in Lamb wave modes. The arrows indicate the direction of the wave propagation.

cement. There should also be no fluid channels inside the cement [3]. Figure 1 shows different problems that may occur when a cement sheath is placed improperly in a wellbore. Causes of a poorly conducted cement job can be divided into two categories: flow problems of mechanical origin like poor centralization and washouts, and degradation of the cement during the curing stage where the cement may be polluted by fluid or gas [4]. The production capacity of a well may never reach its full potential without complete isolation in the wellbore. To control if the cement sheath has been placed properly, a cement job evaluation has to be conducted.

### Cement Job Evaluation: The Pitch-Catch Technique

Since the 1960s when Zemanek and Caldwell first applied the ultrasonic pulse-echo technique to well logging with their tool named the Borehole Televiewer (1969), the ultrasonic tools have been an important tool in the field of cement job evaluation. The ultrasonic tools usually operate in the frequency range of 200 to 700 kHz, much higher than the acoustic tools. The frequencies are chosen to coincide with the resonance frequency of the casing [5]. The so called pitch-catch (P-C) method used e.g. by Schlumberger in their Isolation Scanner (2005) [6, 7] is the technique used in this paper.

The concept of the pitch-catch method involves the Lamb wave and the conditions for the following derivations are that the plate, in which the Lamb waves are excited, is an infinitely unbounded plate lying in the  $xy$ -plane. For sufficiently high frequencies, 80 kHz or more, the pulse from the ultrasonic transducer interacts with a small area of the casing, making the approximation of treating the part of the casing as a part of an infinitely unbounded plate appropriate [8]. A plate supports two infinite sets of Lamb wave modes whose velocities in the plate depend on the relationship between plate thickness,  $d$ , and the frequency,  $f$ . The number of possible modes and the velocity of the different modes are decided by the quantity frequency-thickness,  $f \cdot d$ . As  $f \cdot d \rightarrow 0$  only the lowest anti-symmetrical mode,  $a_0$ , and the lowest order symmetrical mode,  $s_0$ , can appear in the plate. These lowest order modes are called the flexural and the extensional mode respectively and are shown in figure 2. As  $f \cdot d$  increases higher order symmetric and anti-symmetric Lamb wave modes may be excited in the plate.

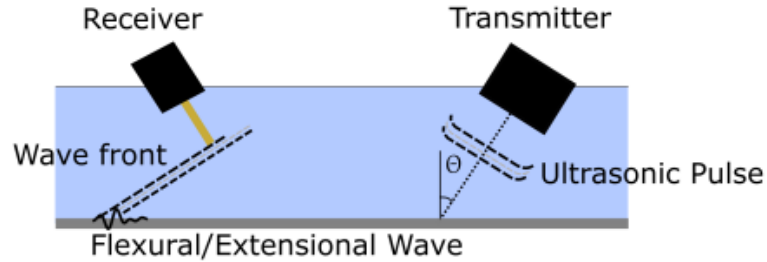


Figure 3: Illustration of the pitch-catch principle. A transmitter emits an ultrasonic pulse which excites Lamb waves in the plate. The Lamb waves propagate in the plate, radiating/leaking energy into the fluid which is detected by the receiver.

In the P-C method, a piezoelectric immersion transducer emits an ultrasonic pulse into the casing fluid. As the pulse hits the solid plate, various Lamb wave modes are excited, dependent on plate thickness, the pulse frequency and the incident angle of the pulse. The Lamb waves then propagate along the plate, radiating or leaking (hence often called Leaky Lamb Waves, LLW) energy into the casing fluid. Due to the velocity of the plate wave being faster than the sound velocity in the casing fluid, the propagating Lamb wave works as an ultrasonic sound source, generating a wave front in the fluid. The wave front in the fluid is then detected by a receiver. A simple sketch of the P-C method is shown in figure 3.

## 2 Set-Up and Experimental Method

### Experimental Set-Up

The ultrasonic experiments were conducted at the Laboratory of Formation Physics at SINTEF Petroleum Research in Trondheim. SINTEF's Statoil funded "Behind Casing Logging Set-Up" (BeCaLoS, fig. 4) was made available to the author to conduct the ultrasonic experiments on. The BeCaLoS was designed to replicate an oil well casing with the possibility to change casing fluid, the thickness and number of plates, and the annulus material. It is formed as a cylinder with a diameter of 500 mm and a length of 200 mm. In this specific experiment a 3 mm thick steel plate was placed on top of the cylinder. To hold the steel plate to the cylinder and to work as a fluid tank, an open cylinder also with a diameter of 500 mm, was bolted to the first cylinder with a rubber ring placed between the plate and the upper cylinder to keep the tank from leaking. On top of the BeCaLoS a transmitter/receiver holder array was placed to make the positioning of the transmitter and the receiver relatively simple. Positions in  $x$ -,  $y$ - and  $z$ -direction as well as the transmitter/receiver tilt in the  $xz$ -plane were adjustable parameters in the experiment. Figure 4 shows a picture of the BeCaLoS together with two sketches. In the experiment an ultrasonic pulser-receiver of the type Olympus Panametrics-NDT 5900PR was used to send an electric pulse to a piezoelectric transducer. The transducer used was a Panametrics C302 Immersion Transducer which has a circular aperture with diameter 1 in. (25.4 mm) and emits an ultrasonic broadband pulse with center frequency 1 MHz. The transducer was mounted in the transducer/hydrophone holder array of the BeCaLoS together with a HNR-0500 needle hydrophone from Onda Corp. The hydrophone has a circular aperture

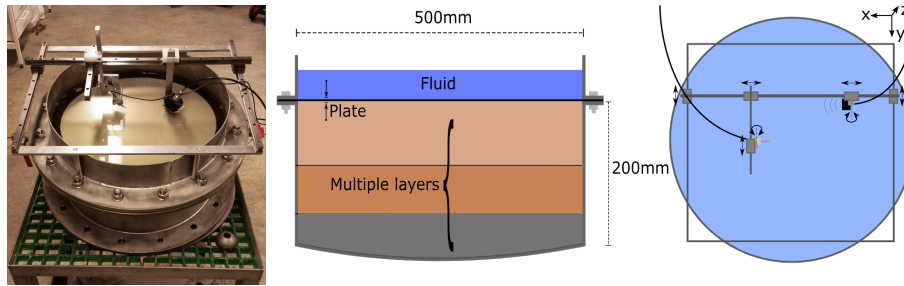


Figure 4: *Left*: SINTEF's Statoil funded Behind Casing Logging Set-Up. *Middle*: Sketch showing the different possibilities regarding number of plates, casing fluid, and annulus material. *Right*: Sketch showing the BeCaLoS viewed from above together with the transducer/hydrophone holder array.

with diameter  $500 \mu\text{m}$ . The electric signal from the hydrophone was sent via the pulser-receiver which amplified the signal, to a digital sampling oscilloscope of the type DSO-X 4024A Oscilloscope from Agilent Technologies. The annulus material was air and the casing fluid was water during the following set of measurement.

### Experimental Method

A considerable part of the work went to configure the set-up, conducting a set of preliminary measurements to find the optimal tilt of both the transducer and the hydrophone, and to eliminate sources of error. The experimental work conducted on the BeCaLoS was inspired by the work done by K. Hoel [9]. The main measurements which will be presented in the following section consisted of adjusting the  $x$ - and  $y$ -position (defined in fig. 4) of the hydrophone with the transducer held still. The  $x$ -positions ranged from 60 - 200 mm with 20 mm intervals between each measurement point, while the  $y$ -positions ranged from 0 to 80 mm with 2.5 mm intervals. For each of these measurement points, the pulse detected by the hydrophone was logged using a LabView program. The rest of the configurations during the measurements can be found in Appendix A.

### COMSOL Simulations

COMSOL Multiphysics was used to make a model of the conducted experiment. As shown in figure 5 and 6 the wave from the transducer was modeled as a circular pulse with the same diameter as the transducer (25.4 mm) and with an incident angle of  $30^\circ$ , bounded spatially by a raised cosine function. The incoming was applied as a boundary load to the plate with two periods of a 1 MHz pulse, bounded by a Gaussian window. The modulated plate was a 30 mm wide, 150 mm long and 3 mm thick steel plate in vacuum. The amplitude of the plate displacement as a function of time and space was analyzed, giving information about the waves propagating in the plate.

## 3 Results

The main measurements resulted in a data set consisting of 264 (8x33) pressure pulses detected as a function of time. Eight examples of the data gathered are shown in figure 7 for the measurements along the  $x$ -axis, together with points indicating the maximum value of the envelope for each measurement (the  $x$ -axis is defined as the propagation direction



**Simplified model in COMSOL**

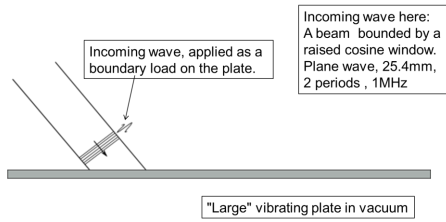


Figure 5: A sketch of the incoming wave modeled as a boundary load on the upper surface of the 3D model.

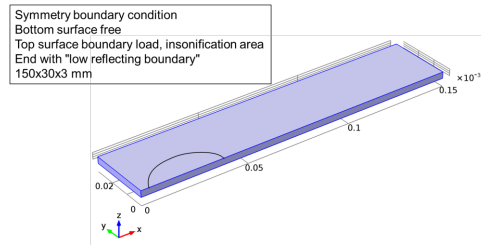


Figure 6: Image from COMSOL Multiphysics showing a 3D plate in vacuum. The ellipse on the plate indicates where the boundary load representing the incoming wave were applied.

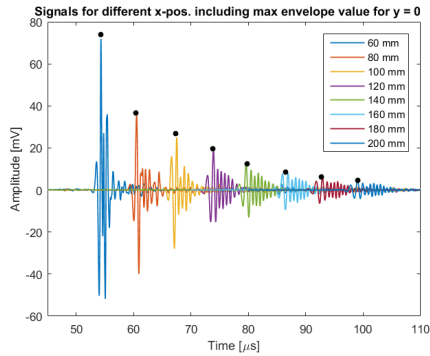


Figure 7: Eight pulses measured by the hydrophone at different  $x$ -positions. The black dots indicates the maximum of the envelope.

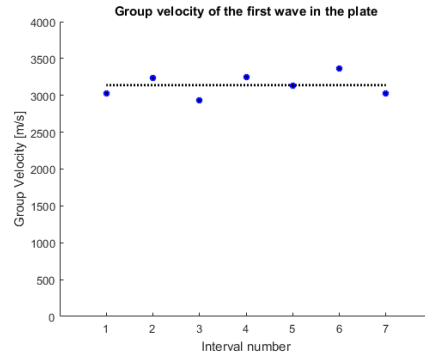


Figure 8: Group velocity of the first Lamb wave as a function of interval number. The black line indicates the average of 3138.5 m/s.

of the LLW, illustrated in figure 4). In figure 8 the group velocity of the wave in the plate, found by measuring the first pulse detected by the hydrophone at each measuring point, is plotted together with a mean value. The average group velocity of the first wave was measured to 3138.5 m/s. Comparing this experiment with the work done by Zeroug and Froelich [10] on a steel plate in water, a group velocity of 3100-3200 m/s was expected for the flexural mode.

The peak amplitude for each measuring point are shown in a logarithmic, normalized plot in figure 9. As the figure indicates, the attenuation of the LLWs are high due to the radiation of energy into the fluid that is in contact with the plate. In figure 10 the absolute values of the peak amplitudes for  $y = 0$  is plotted together with an exponential fit. From the fit an attenuation factor of 0.1927 dB/mm was found. Investigating further how the beam spreads out in the  $y$ -direction, the peak amplitude for each measuring point was normalized against the peak value at the given  $x$ -position and  $y = 0$ . The normalized peak values are shown in a logarithmic plot in figure 11, giving information about the beam profile in the plate. Four cross sections of the beam profile plot with amplitude as a function of  $y$  are shown in figure 12. The peak voltage values at  $y \geq 50$  mm are mainly noise, which becomes more significant at larger  $x$ -values due to the normalization against the exponentially decreasing peak amplitude value at the axis. As both the cross section plot and the black lines in the beam profile plot shows, the LLWs does not spread out much in the  $y$ -direction. After propagating 140 mm in the  $x$ -direction the -6 dB line, where the amplitude have decreased approximately 50% relative to the corresponding peak value at

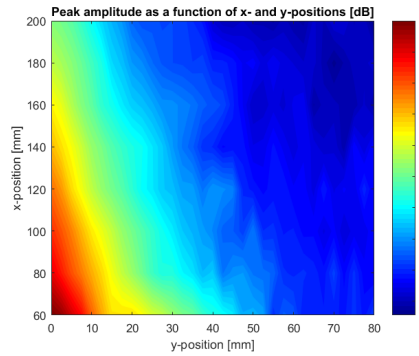


Figure 9: Logarithmic plot of the absolute value of the peak amplitude as a function of the hydrophone's  $x$ - and  $y$ -position.

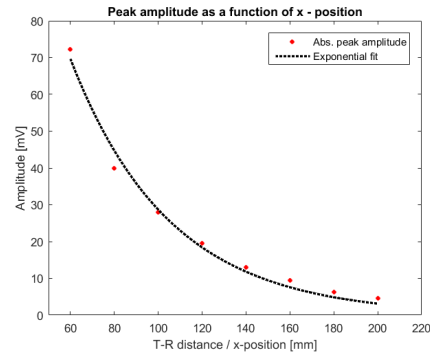


Figure 10: Peak amplitude of the pulse measured along the  $x$ -axis with an exponential fit with an decaying factor of  $-0.1927$  dB/mm.

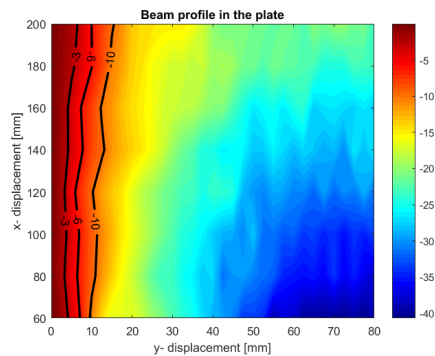


Figure 11: Logarithmic plot of the peak amplitudes normalized against the peak values at  $y = 0$ . The  $-3$ ,  $-6$  and  $-10$  dB lines are drawn in the figure.

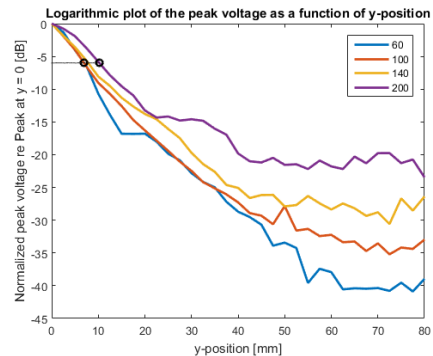


Figure 12: Cross sections of the beam profile figure for four  $x$ -values. The black dotted line and the two circles indicates the  $-6$  dB points.

$y = 0$  has only moved 3.2 mm in the  $y$ -direction. This is also indicated by the two black circles in figure 12.

As the Lamb waves propagate in the plate, the different modes propagate with different velocities. In figure 7 eight pulses detected by the hydrophone are plotted, where the pulse becomes wider as it propagates in the plate. In figure 13 the normalized signals for all the 33  $y$ -values at  $x = 100$  mm are plotted. The red and the blue dotted lines show two detected pulses radiated of the LLWs traveling at different velocities, indicating that it is two different modes. In figure 14 the time delay of the first detected pulse relative to the pulse detected at  $y = 0$  is plotted as a function of  $y$  for the eight different  $x$ -positions. The same is shown in figure 15 for the second detected pulse. Figure 16 shows the time delay of the first detected pulse, zoomed in on  $y \leq 25$  mm, which shows that the time delay at  $y \leq 10$  mm is equal at all of the eight  $x$ -positions. The radius of the transducer was 12.7 mm and hence a flat curve indicating no time delay could be expected for  $y$ -values smaller than 12.7 mm. The small time delay for  $y \leq 10$  mm may originate from the transducer not emitting a plane ultrasonic pulse, but a spatially bounded, slightly curved pulse. In figure 17 and 18 the time of arrival of the first and second detected pulse respectively are shown as a function of the  $x$ - and  $y$ -position of the hydrophone. The figures show clearly how the second pulse travels slower than the first pulse, indicated by the black lines drawn

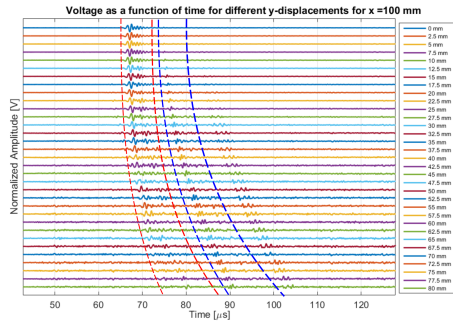


Figure 13: The 33 normalized pulses detected at  $x = 100$  mm. The red and blue dotted lines highlights the first and second detected pulse.

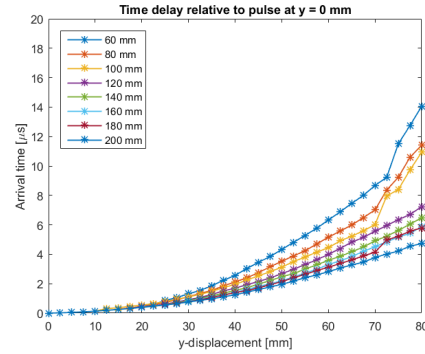


Figure 14: Time delay of the first detected pulse relative to the pulse measured at  $y = 0$  as a function of  $y$ .

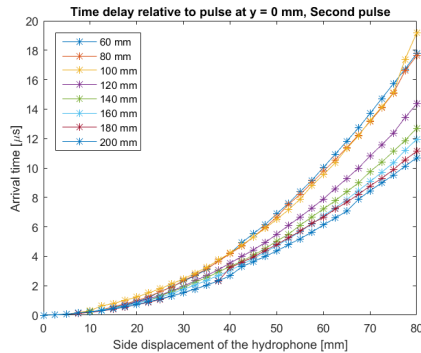


Figure 15: Time delay of the second detected pulse relative to the pulse measured at  $y = 0$  as a function of  $y$ .

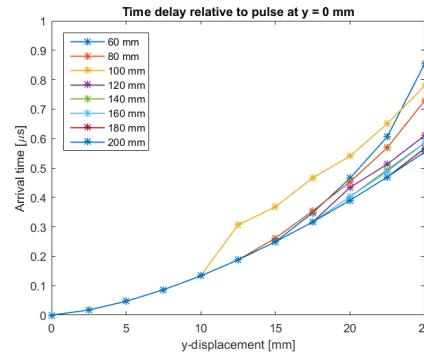


Figure 16: Time delay of the first detected pulse relative to the pulse measured at  $y = 0$  as a function of  $y$ , zoomed in on smaller  $y$ -values from fig. 14.

for every  $20 \mu s$ .

### COMSOL Simulations

Some results of the COMSOL Multiphysics model of a 3D plate in vacuum are shown in figure 19 and 20. In figure 19 it is clearly shown that the Lamb waves have split into two wave packages traveling at different velocities. The first is an anti-symmetrical mode, while the second is a symmetrical mode. This coincides with the measurements done, where the Lamb waves split into multiple wave packages which travels at different velocities. The fact that the first wave package traveling in the plate seems to be the flexural mode in the simulations and that the expected velocities of the flexural wave in a plate contact with water from Zeroug and Froelich's experiment were 3100-3200 m/s [10], fits with the experiment conducted. Figure 20 shows a snapshot in time of the normalized displacement of the top surface for ten different  $y$ -positions. The maximum of the second wave package has traveled a shorter  $x$ -distance for larger  $y$ -values, relative to the corresponding maximum at  $y = 0$  mm, than the maximum of the first wave package. This coincides well with the plots in figure 14 and 15, indicating the time delay between the maximums of the first and second pulse detected, showing a steeper curve for the second detected pulse.

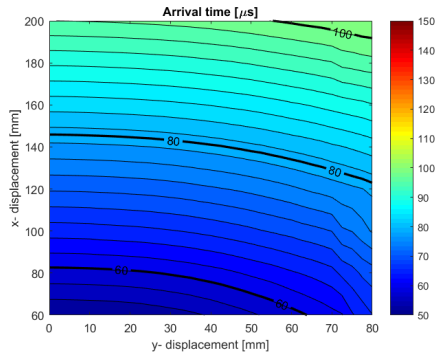


Figure 17: Time of arrival for the first pulse detected by the hydrophone as a function of  $x$ - and  $y$ -positions.

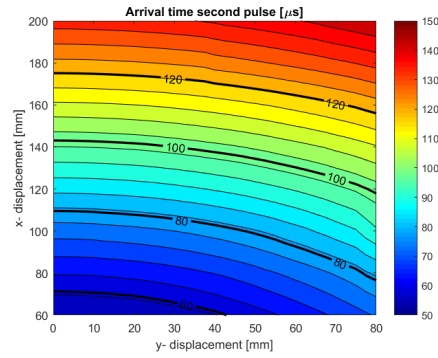


Figure 18: Time of arrival for the second pulse detected by the hydrophone as a function of  $x$ - and  $y$ -positions.

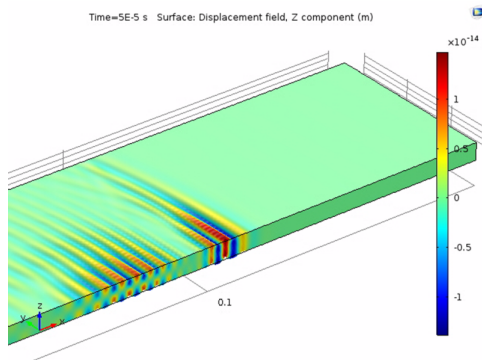


Figure 19: Snapshot of the plate displacement at  $t = 50 \mu\text{s}$ . First wave package is anti-symmetrical while the second wave package is symmetrical.

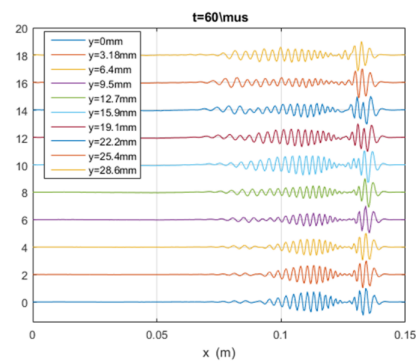


Figure 20: Snapshot of the normalized displacement of the upper surface of the plate for ten different  $y$ -positions, captured at  $t = 60 \mu\text{s}$ .

NB! Legend and plots are in opposite order - the lowest plot belongs to the upper legend entry.

## 4 Conclusion

After a preliminary set of adjustments and measurements the experiments conducted on the BeCaLoS gave good information about the Lamb waves in the plate. The measured group velocity of the Lamb wave are in agreement with the simulations and similar experiments conducted. Inspecting how the plate wave widens in  $y$ -direction due to the impact of the vertically polarized shear waves, it is shown that the Lamb wave spreading is very small and that the plate wave behaves almost as a soundbeam.

## Nomenclature

BeCaLoS	Behind Casing Logging Set-Up
LLW	Leaky Lamb Wave
P-C	Pitch-Catch

## References

- [1] Norwegian Petroleum Directorate, “Norwegian Petroleum Directorate - fact pages.” <http://factpages.npd.no/factpages/default.aspx?culture=en&nav1=wellbore&nav2=Statistics|EntryYear>. Accessed: 13.03.2016.
- [2] M. Khalifeh, H. Hodne, A. Saasen, T. Vralstad, *et al.*, “Techniques and materials for north sea plug and abandonment operations,” in *Offshore Technology Conference*, Offshore Technology Conference, 2013.
- [3] D. Calvert, *Well cementing*, ch. preface. Schlumberger, 2005.
- [4] M. Allouche, D. Guillot, A. J. Hayman, R. J. Butsch, and C. W. Morris, *Well cementing*, ch. 5. Schlumberger, 2005.
- [5] M. Allouche, D. Guillot, A. J. Hayman, R. J. Butsch, and C. W. Morris, *Well cementing*, ch. 15. Schlumberger, 2005.
- [6] Schlumberger, “Isolation scanner - Advanced evaluation of wellbore integrity - product brochure,” 2011.
- [7] M. Bellabarba, H. Bulte-Loyer, B. Froelich, S. Le Roy-Delage, R. van Kuijk, S. Zeroug, D. Guillot, N. Moroni, S. Pastor, and A. Zanchi, “Ensuring zonal isolation beyond the life of the well,” *Oilfield Review*, vol. 20, no. 1, pp. 18–31, 2008.
- [8] R. van Kuijk, S. Zeroug, B. Froelich, M. Allouche, S. Bose, D. Miller, J.-L. Le Calvez, V. Schoepf, A. Pagnin, *et al.*, “A novel ultrasonic cased-hole imager for enhanced cement evaluation,” in *International Petroleum Technology Conference*, International Petroleum Technology Conference, 2005.
- [9] K. Hoel, “Ultrasonic evaluation of well integrity,” 2014.
- [10] S. Zeroug and B. Froelich, “Ultrasonic leaky-lamb wave imaging through a highly contrasting layer,” in *Ultrasonics, 2003 IEEE Symposium on*, vol. 1, pp. 794–798, IEEE, 2003.

## A Appendix

Table 1: The configuration of the BeCaLoS during the main measurements.

Variable	Value
Transmitter - Receiver distance ( $x$ -pos.)	60 - 200 mm
Side-/y-displacement	0 - 80 mm
Transducer Tilt	30°
Transducer Height	30 mm
Hydrophone Tilt	33°
Hydrophone Height	30 mm
BeCaLoS Tilt	8.3°
Pulse/Receiver Settings	
Energy	32 $\mu$ J
Gain	40.0 dB
Attenuators	0.0 dB